博士論文(要約)

Quantum mechanical electron transport driven by surface acoustic waves

(表面弾性波に駆動された電子の量子的伝導)

伊藤　諒

Contents

Chapter 1

Motivation

This document describes my PhD thesis about the development of methods for utilizing traveling electrons driven by surface acoustic waves (SAW) for quantum computations. Before describing my work, two preceding background studies for SAW-driven electrons are presented. One work is related to experiments in the field of quantum-electron optics, such as types that use electron interferometers instead of those of photons. SAW-driven electron transport allows the qubit-encoding of quantum electron optics (e.g., time-bin encoding). The other work is related to the scalability problem of qubits, as defined in static quantum-dot systems. By using SAWs, single electrons can be transported between distant static quantum dots. This protocol is considered a promising method of overcoming the scalability problem. While presenting these studies, I address the motivation behind this thesis. Finally, I provide an outline of this document.

1.1 Quantum-electron optics

Optical systems are promising platforms for quantum information technology. In the field of quantum communications, an optical system is considered to be unbeatable, because the loss of photonic quantum information during transportation is minimized. Recent studies have demonstrated quantum teleportation of 100- to 1,000-km distances [1] with quantum key distributions [2]. It has also been shown that optical systems have great potential for quantum computation, similar to static qubit systems (e.g., transmon qubits comprising superconducting circuits and spin qubits encoded in electron or hole spins) in which quantum error correction codes are available. Photons traveling through the same optical channel can be encoded as different qubits if there is a time delay between them. This allows us to implement deterministic universal quantum manipulation of many qubits using only a few fundamental physical gates by employing a loop structure as information memory, as originally proposed for time-bin qubits [3, 4]. The creation of a cluster-entangled state has been demonstrated by using a delay line to couple multiple time-bin qubits [5]. Thus, it is possible to implement error correction codes for each time-bin qubit, owing to the redundancy in the continuum state of the harmonic oscillator.

Similar to photon qubits, flying electrons in a solid device can also be used as flying qubits. The flying electron qubit should have the same advantages as a flying photon qubit in terms of

scalability, in that it does not require the integration of numerous physical qubits. Instead, the universal quantum operation of many qubits is possible by using only a few fundamental physical gates. The path of such flying electrons should be defined using a 1D channel (e.g., edge channel of the quantum Hall regime or a gate-defined 1D wire defined by electrostatic potential). In contrast to a photon system, the flying-electron system is programmable by means of gate voltage, and it has a strong electron–electron interaction. The size of the device, apart from the cooling system, is much smaller than the optical system, because the velocity of the electron is much smaller than that of photons. Therefore, the use of flying electrons for quantum computations becomes a choice of future quantum information-technology applications.

As a part of quantum-electron optics experiments, interference experiments of flying electrons have mainly been conducted for direct-current (DC) transport using DC bias. The objective of these works was to extract quantum information, such as the phase of the wave function, that was otherwise hidden during standard conductance measurements. A Mach–Zhender interferometer provides one full-qubit manipulation. This was demonstrated for flying electrons through the quantum Hall edge state [6] and the 1D gate-defined channel [7]. The output current is determined by the phase difference of an electron acquired in the two paths of a Mach–Zhender interferometer. Because the phase shift contains information about the scattering present in each path, it is used to gain the full transmission coefficient using a scatterer. For example, it was used to measure the scattering phase of a quantum dot [8]. From the interference amplitude, one can also obtain information about decoherence caused by electron–electron interactions [9–12]. Two-electron interference was also investigated by combining two Mach–Zhender interferometers and measuring the cross correlations [13, 14].

In these interferometer experiments, electrons are injected from electron reservoirs via low-energy excitations. The wave packet is not explicitly generated and is treated as plane wave that extends over all interferometers. This means that we cannot access each electron resolved by time and space. The main advantage of the flying qubit is therefore missing. To overcome this situation, G.Féve et al. developed a single electron source [15]. In their experiment, electrons or holes trapped in a quantum dot were emitted on-demand one-by-one to the quantum Hall edge channel via a rapid sweep of the gate voltage. This created a finite size packet in the form of a charge density wave and enabled the time-resolved experiment. This was the first realization of a single flying qubit generated from an electronic system, but it was imperfect. The problem of this scheme was the simultaneous excitation of electrons and holes, because the excitation is not a pure single electron or hole [16]. Recently, a short Lorentzian-shaped voltage pulse ($V(t) \propto \frac{1}{W^2+t^2}$: W is width) on Ohmic contact, which satisfied the condition for excitation of an integer number of electrons, $\int_{-\infty}^{\infty} V(t) = \frac{nh}{e}$, was found to excite only electrons or holes, as predicted theoretically by J. Keeling et al. [17] and demonstrated experimentally by J. Dubois et al. [18]. Here, n is integer, e is the elementary charge, and h is the Planck constant. Moreover, when n is one, a pure single electron having an energy distribution higher than the Fermi energy is generated. This particle is a leviton, and it has attracted a great deal of research attention [19, 20] because it provides a promising single electron for quantum-electron optics. It is thus considered possible to construct a flying qubit system using levitons. The size of the wave packet reaches several 10s of μm in current radio-frequency technology. One of the difficulties with constructing a leviton-based flying qubit system is cooling the electrons to below several 10 mK, such that the energy distribution of a leviton is not smeared

by the Fermi distribution. The size and temperature could be made smaller or larger by using THz technologies. There are several proposals [21, 22] for quantum manipulation of a leviton state. However, none have yet been realized experimentally.

The electron transport driven by SAW on a piezoelectric material may be an easier and simpler method of realizing the flying qubit. A SAW creates a moving quantum dot when it propagates on a depleted 1D channel. The number of electrons trapped in each moving quantum dot can be set as an integer by the charging energy of the dot. When only one electron is trapped, it is used as a single electron source. Therefore, SAW-driven electrons are also promising for the construction of a flying qubit system. The typical size of the wave packet can be made to be less than 100 nm with the distance between neighboring wave packets around 1 μm. The quantum state of this single electron is robust against increases of temperature up to several Kelvin. These are advantages over the leviton. Another challenge is that the direction of flow is restricted to a direction determined by the inter-digital transducer (IDT) fabricated to generate the SAW. It is thus necessary to combine several SAW sources (i.e., IDTs) to fully control the direction of the electron flow. Compared with the SAW-driven electron system and the photon qubit system, the system size of the SAW-driven electron system can be made much smaller, owing to the far smaller propagating velocity of electrons and the smaller size of the wave packet. Additionally, strong two-particle interactions can be used for the two-qubit operation. However, the SAW-driven electron system has not yet been well-investigated in this light.

One of the most important quantum manipulations is that of coherent beam-splitting, which is used in most of optical setups. Therefore, as one of the targets of this thesis work, I demonstrate the coherent beam-splitting of SAW-driven electrons. This demonstration corresponds with the single flying-qubit manipulation and the first quantum manipulation of a qubit array. The detail of this demonstration is described in Chapter 3. This demonstration of the beam splitter opens a new way of realizing a Mach–Zehnder interferometer of a SAW-driven electron by combining two beam splitters. There is also a theory that proposes a device for demonstrating the violation of Bell ' s inequality by creating an entanglement between two electrons belonging to two neighboring Mach–Zehnder setups [23]. Thus, the realization of the beam splitter should finally lead to the universal operation of multiple qubits.

Research of the flying electron qubit started very recently. One of the purposes of my work is to address its potential. Yet, further works in this field remain necessary.

1.2 Single electron transfer via SAW and electron-spin entanglement

Electrons trapped in static quantum dots are generally considered promising for quantum information technology. Qubit information is usually encoded to the electron spin. Thus, coherence time has reached more than 10 μs in a quantum dot formed in isotopically purified silicon [24,25]. Two-qubit operation has also been realized, and prototype devices containing relatively large number of qubits have been fabricated [26, 27]. To define a logical qubit, which is fully protected from errors, one needs to manipulate numerous physical qubits at high fidelity to perform quantum error detection and correction [28]. Therefore, this type of spin device faces a scalability problem.

To overcome this problem, some researchers have proposed using long-range electron–electron interactions mediated by floating metallic gates [29–31] or superconducting resonators [32–35]. On the other hand, several researchers have considered directly transporting single electrons. One method of single-electron transport is to shuttle an electron between adjacent quantum dots [36,37]. However, this scheme requires many quantum dots to transport an electron over a long distance, and the transport length is currently limited to several μm. Another method is to use a SAW. It was demonstrated that a single electron can be transferred over a long distance of at least 250 μm [38,39]. The efficiency of this electron transport has recently exceeded 99%. It is also possible to select the arbitrary moving dot (i.e., SAW potential minimum) to catch and transfer the electron [40]. Spin scattering during transportation over several μm has been shown to be negligible [41], and manipulation of spin during the transportation has also been demonstrated [42]. Therefore, the electron-spin transport via SAW is useful.

In this thesis work, I also propose to generate and detect non-local entanglement of electron spins using the SAW-driven electrons. These are generated by combining a spin qubit system with a photon system [43]. However, the method of using SAWs has advantages for certain applications, because the projection of photon information to electron information is far from efficient. In an electron system, the ground state of two electrons confined in a static or a moving quantum dot is the spin singlet state, known as a maximally entangled state. Therefore, spatial splitting of an electron pair generates a non-local entanglement state.

In Chapter 6, I present my original scheme to create and detect non-local entanglement. As a part of this scheme, I demonstrate the spatial splitting of two electrons confined in a moving quantum dot into different spatially separated moving quantum dots. A complete set used to create non-local entanglement can be directly applied to distribute entanglements between separated spin-qubit sub-groups. These sub-groups can then be quantum-mechanically connected and mediated by the entangled pair. This should address the scalability issue of the electron-spin qubit system.

1.3 Outline

Here, I provide an outline of this thesis. In Chapter 2, general background related to my work is described. The platform of my experiments is the 2D electron system under the application of strong SAWs. In the first section, a 2D electron system realized in a high electron mobility transistor formed at the interface comprising GaAs/AlGaAs is explained. Then, SAW modes of GaAs devices are described in the second section. The third section is devoted to explaining the technical details used in SAW-driven electron experiments.

Beam splitting for SAW-driven single electrons is described in Chapter 3. I prepare two tunnel-coupled quantum wires in which a SAW-driven electron is transported. A simplified two-level model of beam splitting is described at first, followed by a more precise theoretical description. I simulate coherent electron motion using numerically calculated electrical potential. Finally, the experimental result is presented and compared with the numerical simulation result. The experiment result is found consistent with the simulation. I use the simulation to identify the origin of experimentally observed behavior of the measured current. I also find that the dephasing of the electron-wave function is negligible and that fidelity of the state initialization is very low. This low initialization

fidelity is the motivation of the experiment presented in Chapter 4.

In Chapter 4, the internal orbital state of the SAW-driven electron is measured. This is realized by the measurement of potential dependent electron tunneling to a reservoir. I analyze the experimentally observed current by employing a theoretically derived fitting function, finding that it works well. From the fitting, the internal quantum state of an electron in a SAW potential minimum is evaluated. Additionally, I discuss the case wherein the initial state is not a classically mixed state, but is instead a superposition of orbital states. I also find this to be inconsistent with the experimental result.

In Chapter 5, I show high-visibility tunneling oscillation observed when the barrier potential is directly controlled by the center barrier gate. The origin of this high-visibility current oscillation has not yet been well-understood, but it behaves as if the coherent tunneling of electrons, which escape the confinement of the SAW-driven moving quantum dots, happens. If this is truly coherent electron tunneling, it is the highest interference visibility observed in quantum-electron opticals.

In Chapter 6, electron-pair splitting is described. The electron pair is initially loaded into the potential minimum of a SAW and is then split into different channels at the fork structure of the 1D channel. This experiment is closely related to the realization of non-local entanglement, because the two-electron ground state in a standard quantum dot is the spin singlet. I also present a device design to demonstrate the creation and detection of a non-local entangled pair.

Chapter 2

Background

In Section 2.1, the physics of low-dimensional electron systems are described. Understanding the characteristics of GaAs devices are particularly important for understanding my work. Elaborate devices are realized using GaAs-based semiconductors, which offer ideal platforms for the quantum electron-optics experiment. Section 2.2 refers to SAWs generated on the surface of GaAs. The method of generating a SAW and its properties are discussed. Electron transport driven by the SAW is also described. Technical aspects of the experiments for SAW-driven electrons and related studies are discussed in Section 2.3. The driving of electrons by SAWs and the influences of the SAW on the experimental system are also discussed.

2.1 Devices made of GaAs and low-dimensional physics

Electrons in a material are always exposed to the material's roughness. Materials are full of defects and impurities, and symmetry is unintentionally broken. Numerous attempts have been made during the history of semiconductors to realize clean electron systems. One remarkable achievement was the invention of high electron-mobility transistors in the 1980s. In such transistors, the mean free path can exceed 10 μm. This value far exceeds the typical size of modern semiconductor devices. Research on ballistic electrons is thus made possible.

2.1.1 GaAs high-electron-mobility transistor as a 2D electron system

If the dimension of a system changes, the equations used to describe the system must be corrected from those used for 3D systems. This leads to new physical phenomena. It is thus possible to prepare low-dimensional 2D, 1D, and 0D systems of electrons or holes in solids. Varieties of materials have been developed to investigate low-dimensional physics. For 2D systems, membrane-like materials have recently been used (e.g., graphene and monolayer transition metal dichalcogenides). Epitaxially grown semiconductor devices can also host 2D electrons by sandwiching a thin conductive layer inside insulating layers. In these materials, electron motion is quantized in the growth direction. When only the lowest energy mode is allowed, electron motion is restricted to 2D. Similarly, nanowire materials have been used for studies of 1D physics, and self-assembled quantum dots have

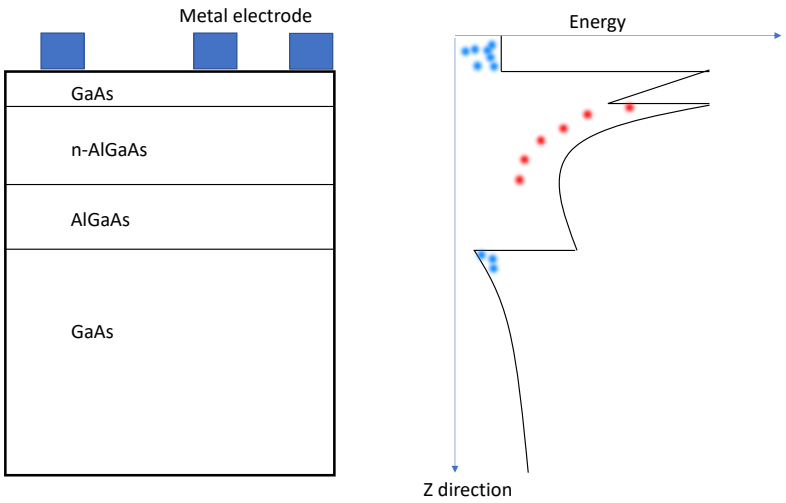

Figure 2.1: Layer structure of GaAs/AlGaAs devices (left) and conduction-band energy bottom perpendicular to surface (right). Blue (red) circle indicates electron accumulated at hetero junction and metal electrode (dopant ionized at n-AlGaAs layer).

been used for 0D physics.

The dimensionality of electron (hole) systems can also be changed by confining the electrons (holes) using the electrostatic potential induced by gate electrodes. By applying tuning voltages to gate electrodes, it becomes possible to restrict electron motion to lower dimensions and to investigate the physics of low-dimensional systems. For example, gate electrodes deposited onto a 2D system can create such confinement potentials either from the top, bottom, or side. Among the variety of 2D systems, the high electron mobility transistor (HEMT) formed at an interface of GaAs and AlGaAs is particularly suitable for the study of electron transport, owing to its long mean-free path. Devices of the highest quality are realized using this type of transistor.

The HEMT has a history greater than 30 years, and high mobility has been achieved after some technical contrivance. A typical structure of the GaAs/AlGaAs HEMT is shown in Figure.2.1. It utilizes a deep potential dip at the junction of the different semiconductors. This potential dip emerges from the combination of the jump of the conduction-band bottom at the hetero-junction and the electrical field caused by ionized dopants. First, AlGaAs has a larger band gap than does GaAs, leading to the jump of the band at the interface. This band-gap mismatch depends on the fraction of Al. In my experiments, I employed $Al_{0.3}Ga_{0.7}As$, which has a band gap of about 1.9 eV, whereas the band gap of GaAs is about 1.5 eV. The jump of the conduction and valence band bottoms are 0.2 eV [44, 45]. Note that both the bottom of the conduction band and the top of the valence band are at the Γ point, and the electron state in the conduction band is at the s-orbital, meaning that no valley freedom is allowed for the electrons. This makes this system easy to understand.

An electric field is created using ionized Si dopants in an n-AlGaAs layer in our device. The energy level of an electron trapped in a Si dopant is known as the DX center. It is placed at 0.12

eV below the conduction-band bottom for $Al_{0.3}Ga_{0.7}As$ [46]. This deep-dopant level is mediated by the deformation of the lattice structure. Electrons trapped in the DX center can easily escape from this level, because their energies are higher than the GaAs conduction at the band bottom. Therefore, they are ionized. As a result, an electrical field is created along the growth direction (z-direction). A deep potential dip is formed at the AlGaAs/GaAs interface, as shown in Figure.2.1. If the potential dip is deeper than the Fermi energy, electrons accumulate at the interface with a strong confinement potential. Typical energy splitting is at the order of 10–100 meV. In contrast, the Fermi energy is tuned to be several-to-10 meV above the lowest mode in the z-direction, thus keeping all electrons in the lowest mode of the confinement direction. The electrons trapped at the hetero-junction are considered to be 2D electron system (2DES).

The role of the undoped AlGaAs layer placed between the GaAs substrate and the n-doped AlGaAs in Figure.2.1 is to separate the 2DEG from the Si dopants and to reduce electron scattering. The distribution of dopants and their unintentional occupation are uncontrollable. This induces randomness to the electrostatic potential and reduces mobility. However, if the distance between the 2DES and its dopants is large, the influence of the potential randomness is suppressed. The surface the GaAs layer is then deposited to protect the AlGaAs layer from oxidization. There is a jump of the potential energy at the junction between the metal and the semiconductor, known as the Schottky junction. At the junction of different materials, the energy band is modified, and polarization takes place, leading to the energy barrier shown in Figure.2.1. This energy barrier is about 0.7 eV for the Ti/GaAs interface [47, 48]. This value is not changed much by the application of a gate voltage. Ti is often used as a glue between the GaAs and another metal (e.g., Au).

2.1.2 1D and 0D structures

When gate electrodes are deposited on the surface of a substrate, the electrostatic potential of 2DES is controlled by means of voltages applied to gate electrodes. Note that both GaAs and AlGaAs are not conductive at low temperatures. Thus, current leakage from the surface gate to the 2DES is small, typically 10^{-20}A [49] for a mesoscopic structures. On the other hand, electrical contact to a 2DES is made by alloying a metal with a semiconductor. A metal electrode contacted to the 2DES is called an Ohmic contact.

Figure.2.2 shows a typical gate design for a short 1D channel. This structure is called a quantum-point contact (QPC). When we apply negative voltages to the gate electrodes, the region beneath the gate is depleted. Electrons then flow through a narrow constriction between the gates. Eigen energies along the confinement (transverse) direction are discretized. It appears as a quantization of the conductance in units of $\frac{2e^2}{h}$ [50] (see Figure.2.2(b)). When the gate voltage is tuned such that the conductance is at the first plateau ($\frac{2e^2}{h}$), only one transmitting mode exists as the realization of the 1D channel. When the conductance is on the second plateau, two transmitting channels exist. The robustness of the plateaus depends on the smoothness of the potential. In our HEMT, because the 2DES is about 100 nm below the surface, and the Fermi wavelength is 40–60 nm, the potential profile defined by such a gate structure is always smooth. Electrons can thus adiabatically transport through the QPC, and the transmission probability of a channel can reach 100%.

It is also possible to construct a structure in which an electron is confined from all directions.

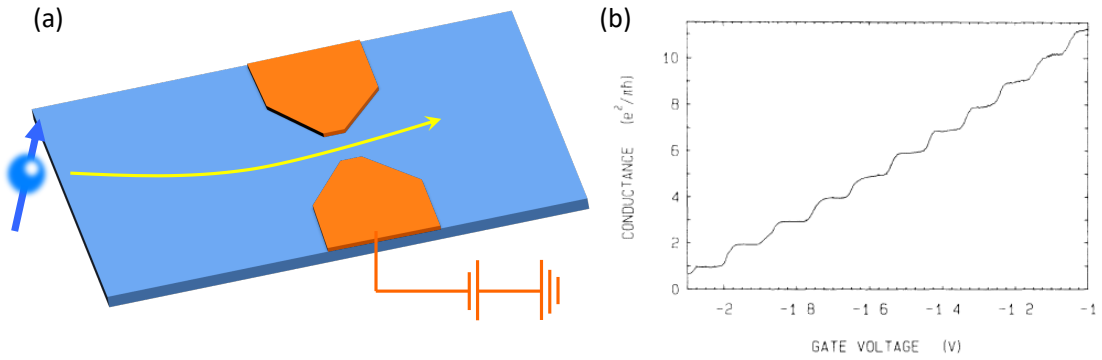

Figure 2.2: (a) Quantum-point contact and electron transported through an opening of the electrical potential. (b) Quantization of conductance cited from [50]

Such a structure is known as a quantum dot. Electron energy is discretized by the single particle energy spacing and charging energy. In a GaAs-based lateral quantum dot, the charging energy is larger than the single particle energy spacing. The electrochemical potential in a quantum dot depends on the number of electrons trapped. Conversely, the number of electrons is tuned electrostatically using gates. This quantum dot is used in my research as a source of integer-number electrons. However, a SAW can induce a moving electrostatic potential, as describe in the next section.

2.2 Generation of a SAW-driven current

A SAW is a mechanical wave that travels on the surface of a material. This mechanical wave mode does not always interact with electrical modes. In the case of piezoelectric materials, however, electrical modes strongly couple with mechanical modes. A sophisticated method of generating a SAW was developed by R.M. White and F.W. Voltmer in the 1960 ' s. They adopted the IDT (see Figure.2.3(a)), which is made of two metal electrodes having comb-like fingers placed facing each other. By applying alternating-current (AC) voltages to the IDT, one can generate a SAW on demand. After the adoption of IDTs, the technique for generating SAWs became more sophisticated, owing to the commercial advantages of implanting SAW systems into electrical circuits. Although the velocity of a SAW is much smaller than that of electrons, SAW devices have been successful in minimizing device sizes and increasing the multi-functionality of circuits. SAW devices are used as filters, oscillators, transformers, and sensors. Nowadays, they are also used for touch-panel systems.

In the context of physics, mechanical systems have recently attracted a great deal of attention. As a counterpart to the photon, a quantized particle of a mechanical wave is known as a phonon. This has become the target of various researches. A key component of such a mechanical system is the IDT, because it allows easy generation of a SAW. In addition to the IDT, the SAW resonator consisting

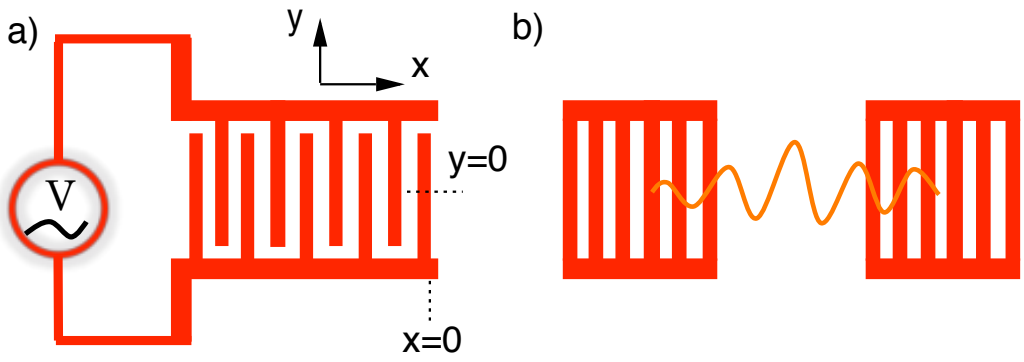

Figure 2.3: (a)An IDT. (b) A SAW resonator.

of two SAW mirrors has been used to confine a phonon to a desired space (see Figure.2.3(b)). Some researchers have employed them for a cavity quantum electrodynamics (QED) experiments that embedded quantum dots [51] or a superconductor transmon qubits [52]. Researchers have also succeeded in generating a number (Fock) state of a phonon in a SAW resonator [53].

In addition to the standing SAW in a resonator, traveling SAWs have also been utilized. In 1996, it was experimentally demonstrated that a high-power SAW could be used to transport single electrons through a gate-defined 1D electron system (i.e., QPC) [54]. Because a single electron is trapped in each SAW potential minimum, experimenting on single flying electrons becomes possible. An important achievement in this field was the single-electron transport between distance quantum dots using a SAW [38, 39]. This single-electron transfer scheme can potentially address the scalability issue of semiconductor quantum-dot-based spin-qubit systems. It also offers a novel platform for quantum-electron optics experimentation.

2.2.1 SAW generation

Generation of a SAW is schematically described in Figure.2.4. When a mutually reversed voltage is applied to the IDT fingers, opposite charges are accumulated under them. The accumulated charge generates an electrical field between the fingers, as indicated by the orange arrows in Figure.2.4. Note that the same situation can be obtained, even when one of the combs is grounded. The equation used to describe the piezoelectricity is written as

$$D = eS + \epsilon E \tag{2.1}$$

$$T = cS - e^t E. \tag{2.2}$$

Here, D, T, S, and E denote the electric flux, stress, strain, and electric field vectors, respectively, and e, c, and ϵ denote piezoelectric constant, stiffness coefficient, and dielectric constant, respectively. These fields and parameters are described using Voigt notation, a rule applied to replace the two-coordinate system in a suffix of one integer based on symmetry. For example, xx is replaced with

Equation of motion	$\rho\frac{\partial^2 u_i}{\partial t^2} = \frac{\partial T_{ij}}{\partial x_j}$	Maxwell's equations	$\nabla \cdot D = 0$
Strain-Displacement	$S_{ij} = \frac{1}{2}(\frac{\partial u_i}{\partial x_j} + \frac{\partial u_j}{\partial x_i})$		$\nabla \cdot B = 0$
Piezoelectric equations	$D_i = e_{ijk}S_{jk} + \epsilon_{ij}E_j$		$\nabla \times E + \frac{\partial B}{\partial t} = 0$
	$T_{ij} = c_{ijkl}S_{kl} - e_{kij}E_k$		$\nabla \times H - \frac{\partial D}{\partial t} = 0$

Table 2.1: Summary of equations describing each field in piezo-electrical materials.

1, and yz is described with 4. The equation without Voigt notation is shown in Table.2.1). The superscript, t, placed on e indicates a transposed matrix. Usually, it is assumed that no real charge exists in a semiconductor. Therefore, the above fields must satisfy the following equation derived from the Maxwell equation:

$$\nabla \cdot D = \nabla \cdot eS + \nabla \cdot \epsilon E = 0. \tag{2.3}$$

A standard method used to find a solution to this kind of equation expands the field with a plane wave while keeping the condition (2.3) at any place and time. This leads to a linear relationship between the electrical field and the strain. Therefore, an electric field applied through the IDT placed on the substrate can generate a SAW. The relationship between displacement (u) and electrical potential (ϕ) is also linear, because these terms are derivatively related to S and E. Equations of the relation between these fields are summarized in Table.2.1.

In a simplified model, IDT fingers are considered to be lines without width upon which voltages are applied (see Figure Figure.2.4b). In this model, electrical potential $\phi_{\mathrm{SAW}}(x_0, t)$ at distance x_0 from the IDT can be calculated as follows:

$$\phi_{SAW}(x_0, t) = c_{SAW}\sum_{n=0}^{N}(-1)^n V(t - \frac{x_0 + \frac{Ln}{2}}{v_{SAW}}). \tag{2.4}$$

Here, c_{SAW} denotes the coupling coefficient between the IDT and the SAW, determined by solving the above equations. N and L indicate the number and period, respectively, of the IDT fingers. Note that eigenmodes of the electro-mechanical coupled system are modified from those of the zero piezo-electric constant system. Although an almost-electrical mode has a velocity approximate to that of light, an almost-mechanical mode has a velocity close to that of a mechanical wave. The SAW is the almost-mechanical wave, and the almost-optical wave component is ignored. For a sinusoidal SAW, V(t)=$Ve^{-i\omega t}$ and ϕ_{SAW} become

$$\phi_{SAW}(x_0, t) = c_{SAW}Ve^{i\{\frac{\omega}{v_{SAW}}(x_0+\frac{L}{4})-\omega t\}}2i\sin(\frac{\omega L}{4v_{SAW}})\sum_{n=0}^{\frac{N}{2}} e^{i\frac{\omega Ln}{v_{SAW}}}. \tag{2.5}$$

For simplicity, N is assumed to be even. ϕ_{SAW} takes the maximum value for $\omega = \omega_0 = \frac{2\pi V_{SAW}}{L}$.

For more precise calculations, the internal reflection of a SAW (between IDT fingers) and the reflection to the IDT input line for the conversion from a SAW to an electrical wave must be considered. It is also necessary to consider the position dependence of the charge accumulation enhanced at the edge of the IDT. The center and the edge of the IDT have different capacitances and

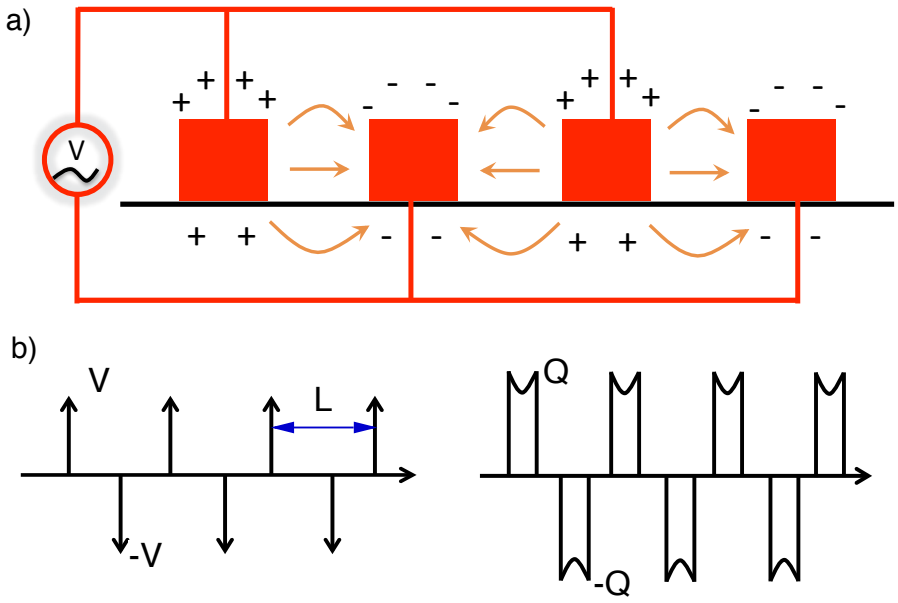

Figure 2.4: IDT when voltage is applied. (a) Description of the charge and electric-field distribution in space. Orange arrow indicates the electrical field. (b) Left (right): Simplified distribution model of electrical potential (charge) on the surface caused by IDT.

charge distributions, and each IDT finger is space-dependent. Taking all of these things into account during the calculation is too cumbersome. Additionally, our current technology for IDT fabrication is imprecise. There is a deviation of the IDT dimensions by an order of 10 nm from the design. This deviation is not negligible for such a precise calculation, because we employ 250-nm-wide IDT fingers.

We have assumed that a SAW propagates through a 1D path. In a 2D system, the diffraction effect is important. Because the IDT is a 2D object, a wave generated at $y = 0$ (see notation in Figure.2.3) and those at $y \neq 0$ take different paths. Waves from different parts of the IDT are added at a certain distance from the IDT, similar to the light focused by a lens [55].

2.2.2 SAW in GaAs

Heretofore, we have discussed the general properties of SAW devices. Next, we discuss specific features of a SAW in GaAs. GaAs belongs to the III–V semiconductor class and forms a zincblende crystal. Owing to the absence of spatial inversion symmetry of the crystal, there is an internal charge polarization and a surface charge that depends on the strain. The surface mechanical modes are derived using the piezoelectric equation and the equation of motion under a stress-free boundary condition at the surface [56] ($T_{i3}(z = 0) = 0$; see equations in Table.2.1). Roughly, surface waves can be classified by their two wave modes. One is a normal surface acoustic wave (NSAW), which has no attenuation along the propagation direction parallel to the surface. The other is a leaky SAW (LSAW) or pseudo-SAW. This wave mode has a finite component of a bulk shear horizontal wave.

This mode leads to attenuation along the propagating direction.

Calculation of the phase velocity and the piezoelectric coupling constant provides some specific features of the SAW in GaAs. The piezoelectric coupling constant, $K^2 = \frac{2\delta v_0}{v_0}$, indicates the piezoelectricity. Here, v_0 is the phase velocity of the SAW without piezoelectricity, and δv_0 is the phase velocity correction for the piezoelectricity. The piezoelectric coupling constant is equivalent to the ratio between the piezoelectric constant and the stiffness coefficient in the bulk mode. Although the relationship is not kept in the surface mode, the piezoelectric coupling constant is used to evaluate the strength of the piezoelectricity. In GaAs, the NSAW has a smaller maximum piezoelectric coupling constant than does the LSAW (see Figure.2.5(b)). Thus, LSAW modes are used in piezoelectric devices made of GaAs. The most commonly used crystal angle in GaAs for piezoelectric devices is the [110] direction on the (001) surface. The wave mode is symmetric with the rotation by $\pi/2$ around the axis perpendicular to the surface. It also has an inversion symmetry on the (110) and (100) plane. This direction not only has a large piezoelectric coupling constant, but it also surprisingly suffers from no attenuation, because coupling to the bulk modes is absent for this specific angle (see Figure.2.5(c)). It is thus possible to consider the LSAW along the [110] direction as a pure Rayleigh wave.

Another advantage of using this direction for SAW propagation is that the (110) plane is a cleavage plane. IDT fabrication along the [110] direction is, therefore, easy. This direction is also free from unwanted wave flow. The cusp structure in the group velocity on a (001) plane of GaAs, as shown in Figure Figure.2.6, indicates that there are more than one allowed modes along a direction inclined from the [100] direction. This structure originates from flows of different wave-vector waves to the identical direction because of the bending of the slowness surface. This is the reciprocal of the phase velocity. However, the [110] direction is free from this effect.

The piezoelectric constant of GaAs is not large (0.07%). For example, Li niobate and Li tantalate have much larger piezoelectric constants. Quartz also has a larger piezoelectric constant [57]. These are commercially used materials. However, GaAs can instead form a very clean 2D electron system having a mobility of 10^6 cm^2/V. This clean system is ideal for our electron-transport experiment mentioned in the next section.

2.2.3 Formation of a moving quantum dot

A SAW generated by an IDT is a kind of electrical potential wave for electrons. For a weak SAW, this wave provides slight modulation of the electrostatic potential to the 2DES. For example, electrons acquire their momentum from the phonons constructing along the SAW. However, when the SAW amplitude becomes large enough, the effect of a SAW is no longer described by such perturbations. Moreover, when a SAW is combined with a depleted 1D channel, only SAW-driven electrons contribute to the current. Electrons are trapped in the SAW potential minimum and dragged by SAW if its electrical potential is higher than the kinetic energy of electrons. In such a situation, quantization of the current is typically observed. Because the potential structure of a SAW is similar to moving quantum dots (see Figure.2.7), strong charge repulsion between electrons plays an important role. Electrons having excessive energies are thus expelled from the potential minimum. The quantization of the number of electrons in each potential minimum, therefore, occurs at the boundary between the electron reservoir and the depleted 1D channel. If all the SAW

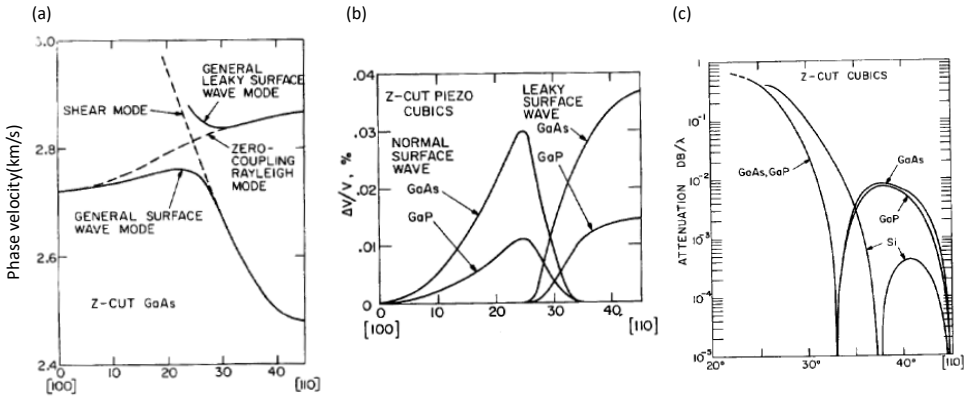

Figure 2.5: Characteristics of SAW cited from [58]. (a) Phase velocity, (b) piezoelectric coupling constant, and (c) attenuation of leaky saw are plotted as a function of the wave-vector direction.

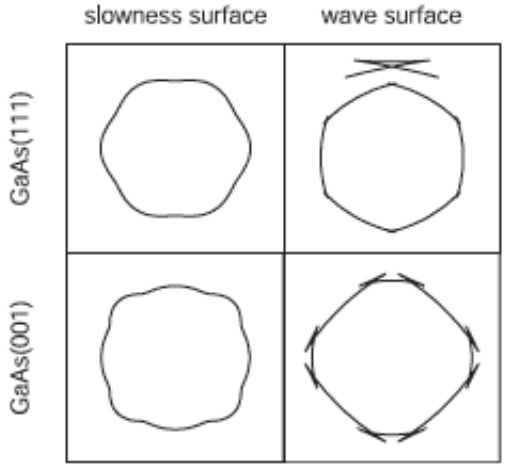

Figure 2.6: Slowness surface of phase velocity (left) and group velocity (right). Vertical direction is [112] at GaAs (111) cut and [100] at (001) cut. The figure is cited from [59]

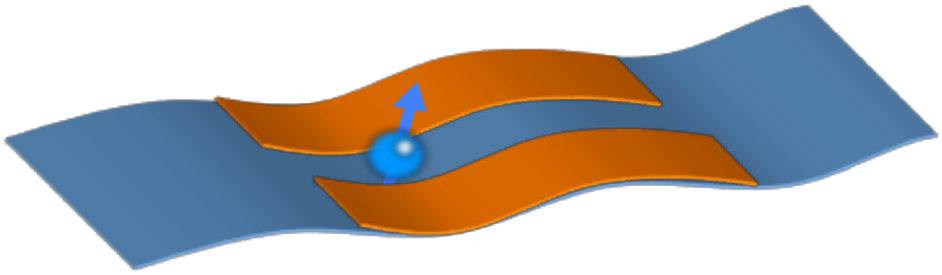

Figure 2.7: Image of electron flow by SAW

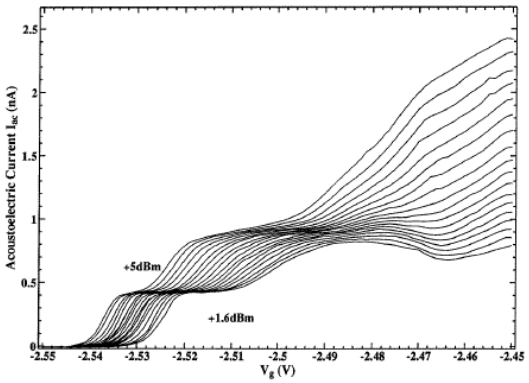

Figure 2.8: Current quantization by the surface acoustic wave. Figure is taken from [54]

potential minima are identical (i.e., the SAW is periodic), then they convey the same number of electrons. Therefore, the total number of electrons transported per time (current) is given as

$$I = nef, \tag{2.6}$$

where n is the number of electrons in each potential minimum, e is the elementary charge, and f is the frequency of the SAW.

Experimentally, a 1D electron system is defined by the gate electrodes that allow the arbitrary control of the channel width. By increasing the confinement potential by increasing the applied negative gate voltages, the number of trapped electrons decreases one-by-one (see Figure.2.8). Additionally, the current decreases by a unit of ef. Using n, it becomes possible to determine the number of electrons used in the experiment.

2.3 Techniques and summery of preceding studies on SAW-driven electron

Historically, the electron transport driven by the SAW has mainly been studied in the field of metrology. The current shows discrete steps in units of ef. This discovery was considered to be a promising opportunity to define the current standard. Therefore, numerous attempts have been made theoretically and experimentally to improve the accuracy of the measured current at its plateau. Recently, however, studies on the current standard seem to have been taken over by the scheme of gate-controlled electron-pumping processes [60]. Technologies developed for the current standard are still useful in my study, however. In this section, some technical aspects of the related studies are presented. My work is related to the motion of electrons driven by the electrical potential of SAWs. Studies described in this section provide insight about the electron environment.

2.3.1 Process of current quantization

In my work, single electrons are first loaded from the reservoir to moving SAW potential minima. This initialization process is a difficult one to access experimentally. Intuitive understanding is easy: the excess electrons are ejected to the reservoir by the strong charging energy. However, it is difficult to determine which quantum state is realized for an electron trapped in a SAW potential minimum. Some people have considered this process completely quantum mechanical. However, they reached this conclusion by including only two initial electrons [61], owing to the difficulty of calculation. Others have tried to explain this process semi-classically [62]. Their research has only shown the validity of the formation of the current plateau. A.M. Robinson and C.H.W. Barnes treated the same problem completely classically [63]. They considered many electrons in a quantum dot as the initial state and calculated their time evolution. Owing to the exchange of energy between electrons, some electrons had higher energies than did the barrier potential, and they dropped from the quantum dot. Because of this process, the final number of electrons was stabilized in their calculation. The configuration of initial electron positions and the resulting SAW-quantized current are shown in Figure.2.9(a) and (b). Additionally, the researchers evaluated the electron temperature for the remaining electron in the quantum dot, as shown in Figure Figure.2.9(c). If the initial temperature is 0 K, electrons are heated up, because the area in which electrons can move increases as the number of electrons in the quantum dot decreases. On the other hand, if the initial temperature is high, electrons in the quantum dot are cooled. This is because the energy is extracted by the expelled electrons. The electron temperature after this process becomes stable, regardless of the environment temperature.

Current noise around the quantized current plateau was experimentally measured by A.M. Robinson et al. [64, 65]. They observed larger noises than were theoretically expected from the shot noise. They pointed out that this was caused by the switching of the impurity states. This argument is reasonable, because many impurities exist in GaAs HEMT samples, because dopants provide electrons. Even for un-doped devices, the density of impurities is still high, exceeding $10^{13}\mathrm{cm}^{-3}$ [66–68]. Evaluating the negative influence of the impurities remains a long-term issue. It is also an inevitable issue for general semiconductor devices. In any case, it is necessary to take this

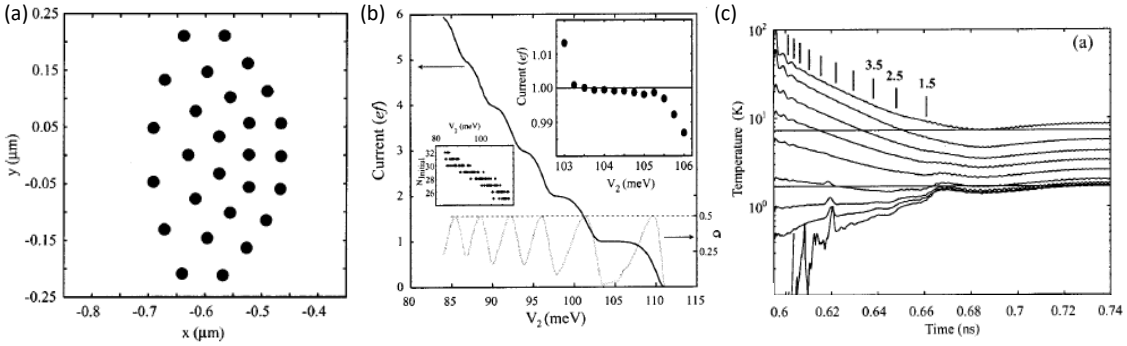

Figure 2.9: Numerical simulation of SAW-driven electron transport. (a) Example of initial position of electrons. (b) Current as a function of barrier potential averaged over 10,000 simulations at each barrier height. (c) Electron temperature at each timing of electron transport. If initial temperature is small (large) final temperature increases (decreases). Data are cited from [63].

influence into account, because it can corrupt the experimental vlidity. Note, however, that there is a possibility of drastic improvement of device properties when using un-doped wafers. Recently, the quantization of current was demonstrated using an un-doped GaAs device [69].

2.3.2 Heating and SAW reflection

A SAW emitted from the IDT also significantly modifies the environment. The first influence includes the increase of temperature [70, 71]. The microwave power required for the IDT is greater than 10 dBm to find a robust quantized plateau of the current. This often exceeds the cooling power of a cryostat, particularly for a dilution fridge. Therefore, an increase of the electron temperature is inevitable. One solution to suppress the heating is to use pulse bursts. They shorten the time duration of the SAW application, suppressing the heating while sacrificing the current. A typical experimental result for the heating is shown in Figure.2.10(a). The electron temperature begins to increase around -15 dBm without a pulse burst and 10 dBm with the pulse burst. In the previous section, suppression of the electron temperature was described. However, heating by the SAW mainly affected the phonon temperature. It can also dephase the electrons. Therefore, the application of pulse bursts is technically important.

Usually only a SAW traveling directly from the IDT to and through a channel is considered. However, a SAW initially traveling through the main structure of the sample possibly reflects back from the edge or the metallic gates [72, 73]. This reflected-SAW is weak compared with the original wave. However, it can remain in the main structure for a relatively long time. Figure.2.10(b) shows the decay of the remaining SAW as a function of time measured by changing the pulse burst period. It observes the current flowing through the QPC structure when a SAW is applied. The SAW works as a turnstile periodic opening of a conduction channel by periodically decreasing the potential barrier rather than driving the force to cross the potential maxima. If the reflected SAW emitted at the previous pulse burst is added to the directly injected SAW, the current is enhanced. In the

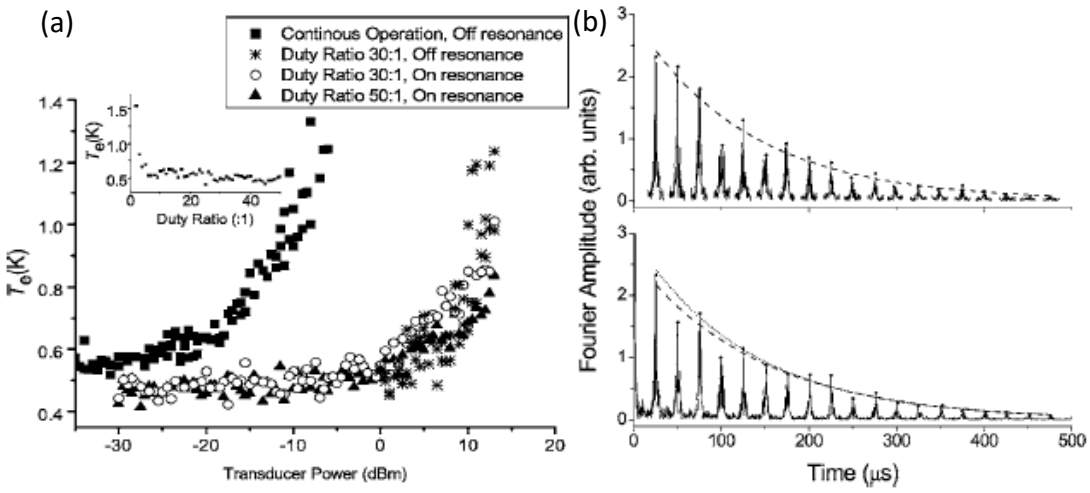

Figure 2.10: (a) Electron temperature measured with the quantum dot when a SAW is applied. Electron temperature exponentially increases as the power of the SAW increases. The increase of temperature is suppressed by inducing the pulse burst operation. Data are cited from [70] (b) SAW-induced current as a result of interference with reflected wave measured using the Fourier transform of the current patter as a function of the frequency of the SAW. A peak appears in the Fourier component at the period of the pulse burst (25 μ) in the lower figure, where the n ' s peaking from the left originate from the interference of SAWs between n-times different pulse bursts. The upper figure shows the accumulation of data for the first peaks when the pulse period is changed. Both data show similar decaying patterns. Data are cited from [73].

experiment, pulse width is set to 0.5 μ, which is short enough to neglect the interference of the SAW emitted at a single pulse burst. Exponential decay of the current was observed in an experiment with a decay time of over 100 μs. The influence of the reflected SAW thus exists and is sometimes used as an additional control parameter [74]. However, in most experiments, it deteriorates the controllability of the electrons.

2.3.3 Detection of SAW amplitude

The amplitude of the SAW is an important parameter in experiments for SAW-driven electron transport. To measure the amplitude, it is necessary to compare it with a reference whose energy scale is known. Such an energy reference is defined using electrons trapped in a static quantum dot. The energy spacing between different energy states in a single quantum dot is measured using the Coulomb diamond [70, 75, 76]. Figure.2.11 shows an example measurement of the SAW amplitude using a quantum dot formed by an unintended impurity potential. In the insets of Figure.2.11(a) a cross section of the Coulomb diamond along the source-drain voltage is plotted with a fixed-gate voltage. Differential conductance though the quantum dot is determined by the relationship between its electrochemical potential ($\mu(n)$; n: number of electrons in the quantum dot) and the electrochemical potential of the source (μ_s) and drain (μ_d) reservoirs. If the electrochemical

potential of the n-th electron in the quantum dot is placed in the bias window defined by the source and drain bias ($\mu_s > \mu(n) > \mu_d$), the differential conductance increases. Otherwise, the current is suppressed (i.e., Coulomb blockade). To achieve the maximum source-drain bias to lift the Coulomb blockade, the following relation must be satisfied: $\mu_s = \mu(n+1) = \mu(n) + \Delta E_C = \mu_d + \Delta E_C$, where ΔE_C is the additional energy. When the source-drain bias exceeds the addition energy, ΔE_C, the blockade is lifted, because either $\mu(n)$ or $\mu(n+1)$ must be in the bias window. The left inset of Figure.2.11(a) shows the measurement of the addition energy, $\Delta E_C \approx 0.3$ meV. In Figure.2.11(b), the source-drain bias is set to zero, but a SAW is applied. The derivative of the current by the radio-frequency (RF) power applied to the IDT is plotted as a function of the gate voltage and power. The current changes around the black curve, whereas it remains constant around the gray region. The role of the SAW in this experiment is to oscillate the electrochemical potential of the electron in the quantum dot by the amount of the electrical potential of the SAW ($\mu(n,t) = \mu(n) + A_{SAW} \sin(2\pi f_{SAW} t$; A_{SAW} is the electrical potential amplitude of the SAW; f_{SAW} is the frequency of the SAW). When the electrochemical potential of the electron crosses the energy window or the Fermi energy of the reservoirs, the current flows. The maximum amplitude of the SAW for the current suppression satisfies the following relation: $\mu(n+1) - A_{SAW} = \mu_s = \mu_d = \mu(n) + A_{SAW}$. From the relation, $\mu(n+1) - \mu(n) = \Delta E_C$, the intersection of two black curves indicated by the white double arrow satisfies $\Delta E_C = 2A_{SAW}$. Therefore, the applied RF power of about -12 dBm corresponds with the SAW amplitude of 0.15 mV in this experiment. Using this evaluation method, modulation of the chemical potential of the source and drain reservoirs can be neglected. This is because the electrical potential of the SAW is screened in the region of high electron density. However, the assumption of no modulation of the chemical potential of the reservoirs is not fully justified.

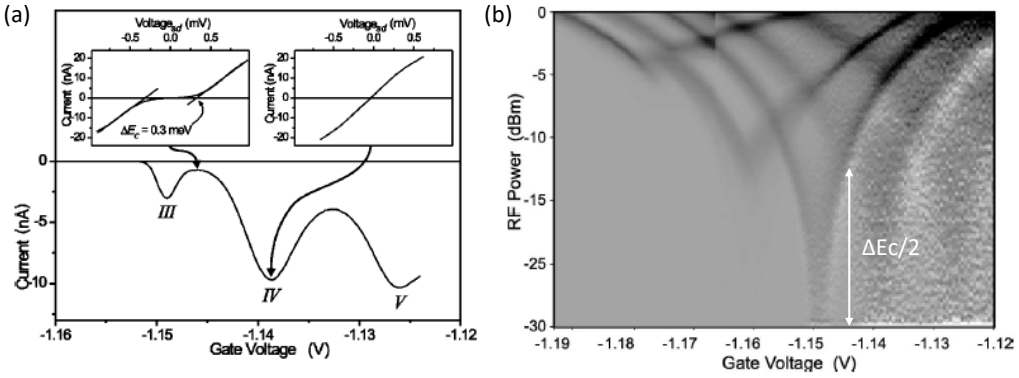

Figure 2.11: (a) Pinch-off curve of a quantum point contact where an unintended impurity quantum dot is formed. Inset: bias voltage is swept at each gate voltage. If the chemical potential of the quantum dot is within the energy window of the source-drain bias, the differential conductance increases. In the left inset, a small differential conductance region appears over the bias of 0.3 mV for the gate voltage of -1.145 V. (b) Derivative of the current by the RF power as a function of the gate voltage and power applied to the IDT. Source-drain bias is almost zero in this measurement. At the intersection of two curves at the gate voltage of -1.145 V, the two chemical potentials for the n-th and (n+1)-th electron in the quantum dot (n is unknown) are aligned with the chemical potential of reservoirs when the SAW-induced potential maximum and minimum arrive. This means that the amplitude of the chemical potential oscillation at half of the 0.3 mV, which is measured in (a). Therefore, the RF power at the intersection corresponds to the 0.15-mV SAW amplitude in this experimental setup. Data are cited from [75].

Chapter 3

Coherent beam splitter for electrons driven by surface acoustic waves

A beam splitter is essential for realizing quantum electron optics at the single electron level. In an optical system, optical beam splitters are used for varieties of experimental setups. Thus, if we follow the optics experiments, a realization of the counterpart to the optical beam splitter for electrons is necessary. It is desirable for a beam splitter to have the ability to split electrons into two different stochastic directions. This splitting must also be a quantum-mechanical splitting. The wave function of each electron must be split at the beam splitter. To realize this, a tunnel-coupled wire device structure, as shown in Figure.3.1, was proposed [77, 78]. This beam splitter has already been demonstrated for DC bias-driven electrons [6, 7]. However, it has not been demonstrated for a single electron trapped in a moving SAW potential wave. Therefore, realization of a quantum-mechanical or coherent beam splitter is necessary to pursue quantum electron optics and realize the flying qubit of an electron trapped in the SAW potential. In this chapter, I present the experimental realization of coherent beam splitting with numerical calculations. In Section 3.1, the time evolution of the electron state is considered in a simple two-level model. Section 3.2 is devoted to the numerical calculation of the realistic potential profile in a real space. Combining the potential calculation using the finite element method (FEM) to solve the Laplace equation and time-dependent Schrödinger equation for simulation of time evolution, I obtain the current expected to be observed for coherent time evolution as a function of the gate voltage used to control electrical potential of conduction channel. A complicated time-evolution process and a higher-lying excited state are also included in the calculation. Finally, I present the experimental demonstration of the coherent beam splitter. I also discuss the experimental setup and characteristics of the SAW-driven current for reference.

3.1 Two-level model

I first explain the tunnel-coupled wires as a coherent beam splitter for a single electron using a simple idealized model. Here, the operation of the beam splitter is seen as a realistic device. The device structure comprises two 1D channels that are tunnel-coupled in the center region (see Figure.3.1). We explain the time evolution of the electron state in this structure using quantum mechanics.

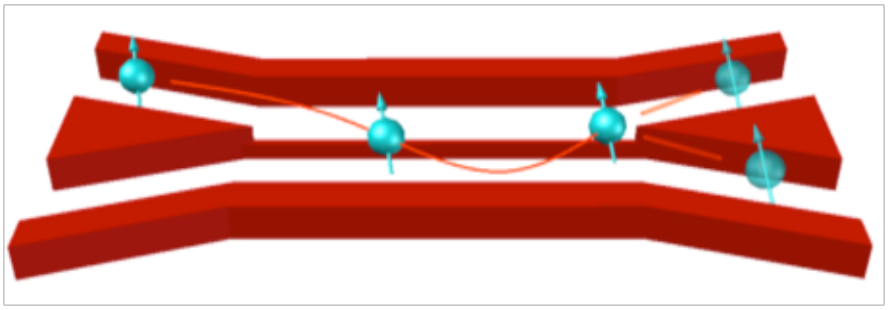

Figure 3.1: Electron-tunneling process in a tunnel-coupled wire.

Although the explanation here is still based on the simplified model, which only considers two levels defined by the electron position in the upper or lower channel, the model provides an intuitive understanding of what happens in this structure. We consider two cases. The first requires an electron as a free wave corresponding to the situation of a preceding study by Yamamoto et al. [7]. The other requires an electron to be confined in the SAW potential and travel with it. Both situations have similar outcomes, but the physical descriptions are different.

3.1.1 Free electron case

A free electron propagates through a 1D channel as a plane wave. The electron state is characterized by $e^{\pm ik_f x}$ with the wave number determined by $\frac{\hbar^2 k_f^2}{2m} = E_f - \phi$. Here, E_f is the Fermi energy, and ϕ is the on-site electrical potential. When two parallel wires are tunnel coupled, the eigenstate is modified in the tunnel-coupled region. The eigenstate splits into two plane waves of different wave numbers, causing the interference seen in the following.

Within the two-level model, a tunnel-coupled wire is described by the tunneling energy, τ, and the difference of detuning energies, ϵ. The former denotes the strength of the tunnel coupling in the tunneling region, and the latter denotes the electrical potential difference between the two wires. The confinement potential term of the Hamiltonian is

$$H_\tau = \frac{\epsilon}{2} |\uparrow\rangle \langle\uparrow| - \tau |\uparrow\rangle \langle\downarrow| - \tau |\downarrow\rangle \langle\uparrow| - \frac{\epsilon}{2} |\downarrow\rangle \langle\downarrow|, \tag{3.1}$$

where $|\uparrow\rangle$ and $|\downarrow\rangle$ indicate the presence of the electron in either of the two (upper or lower) channels. The eigenenergy and the eigenstate of H_τ are $E_\pm = \pm\frac{\sqrt{\epsilon^2+4\tau^2}}{2}$ and $|\pm\rangle = \frac{\epsilon \mp \sqrt{\epsilon^2+4\tau^2}}{2A} |\uparrow\rangle + \frac{\tau}{A} |\downarrow\rangle$, respectively. Here, A is the normalizing factor, $A = \sqrt{\tau^2 + \{\frac{\epsilon-\sqrt{\epsilon^2+4\tau^2}}{2}\}^2}$. Note that E_-, the lower energy state, is the bonding state of the wave functions in the upper and lower channels. $\tau > 0$ if the phase of $|\uparrow\rangle$ and $|\downarrow\rangle$ are the same.

By including the kinetic term and the average of the on-site electrical potential, the Schrödinger equation becomes

$$\{-\frac{\hbar^2}{2m}\frac{\partial^2}{\partial x^2} + \phi + H_\tau\}\psi(x) = E_f\psi(x), \quad \psi(x) = \psi_\uparrow(x) |\uparrow\rangle + \psi_\downarrow(x) |\downarrow\rangle . \tag{3.2}$$

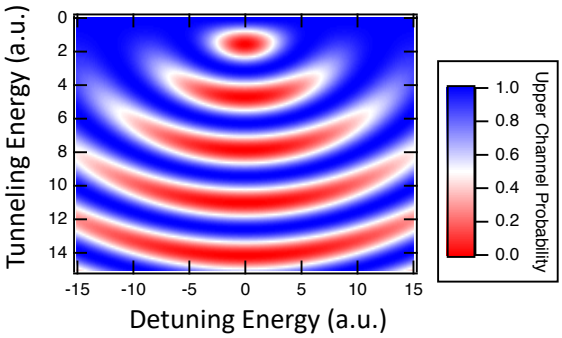

Figure 3.2: Probability of the position of electron in the upper channel after being transported through the tunnel-coupled wire when the initial state is in the upper channel.

After diagonalization by the eigenstate of H_t, the equation becomes

$$\{-\frac{\hbar^2}{2m}\frac{\partial^2}{\partial x^2} + \phi \pm \frac{\sqrt{\epsilon^2+4\tau^2}}{2}\}\psi_\pm(x) = E_f\psi_\pm(x). \tag{3.3}$$

The solution of this equation for a right-moving wave is $\psi_\pm(x) = e^{ik_\pm x}\,|\pm\rangle$, where $k_\pm = \frac{\sqrt{2m(E_f-\phi\mp\frac{\sqrt{\epsilon^2+4\tau^2}}{2})}}{\hbar}$. If the initial electron state is $|\uparrow\rangle$ and has an energy E_f, the electron state at the exit of the tunnel-coupled wire is

$$|fin\rangle = \langle+|\uparrow\rangle\, e^{ik_+L}\,|+\rangle + \langle-|\uparrow\rangle\, e^{ik_-L}\,|-\rangle\,. \tag{3.4}$$

Here, L is the length of the tunnel-coupled region. If E_f is much larger than the potential terms, ϵ and ϕ, $k_\pm \approx \frac{\sqrt{2m}}{\hbar}\{\sqrt{E_f-\phi} \pm \frac{\sqrt{\epsilon^2+4\tau^2}}{4\sqrt{E_f-\phi}}\}$. $k_+ - k_- \approx \frac{\sqrt{2m(\epsilon^2+4\tau^2)}}{2\hbar\sqrt{E_f-\phi}} = \frac{m\sqrt{\epsilon^2+4\tau^2}}{\hbar^2 k_f} = \frac{\sqrt{\epsilon^2+4\tau^2}}{\hbar v_g}$ is the difference of wave number between the two modes. v_g is the group velocity of the traveling electron. By substituting this approximation into (3.4), the probability of the final electron state ($|\uparrow\rangle$ or $|\downarrow\rangle$) after transmitting through the tunnel-coupled wire is obtained as plotted in Figure.3.2. Oscillation as a function of the tunneling energy appears to have nearly zero detuning energy. Note that in (3.4), the reflection of the electron at the connection between the tunnel-coupled region and the zero-tunneling-energy region is ignored.

3.1.2 Confined electron case

Next, we consider the case in which the electron is transported by the moving potential induced by the SAW. The time-dependent Schrödinger equation is

$$\{-\frac{\hbar^2}{2m}\frac{\partial^2}{\partial x^2} + \phi(x-vt)\}\psi(x,t) = i\hbar\frac{\partial}{\partial t}\psi(x,t). \tag{3.5}$$

Here, $\phi(x-vt)$ is the time-dependent potential, and the velocity, v, of the SAW potential wave is assumed to be constant. The explicit form of $\phi(x-vt)$ is not considered here, but it should be large

enough to confine and convey the electron. We define x' as $x' = x - vt$. Then, by substituting x' into (3.5), the Schrödinger equation becomes

$$\{-\frac{\hbar^2}{2m}\frac{\partial^2}{\partial x'^2} + \phi(x')\}\psi(x',t) = i\hbar\{\frac{\partial}{\partial t} - v\frac{\partial}{\partial x'}\}\psi(x',t). \tag{3.6}$$

Note that the partial derivative by t in (3.6) is applied for the fixed x', although x is fixed for the partial derivative in (3.5). By simple calculation and considering the gauge transformation, $\psi(x',t) = e^{i\frac{x'mv}{\hbar}}\psi'(x',t)$, the time-dependent Schrödinger equation becomes time independent.

$$\{-\frac{\hbar^2}{2m}\frac{\partial^2}{\partial x'^2} - \frac{mv^2}{2} + \phi(x')\}\psi'(x',t) = i\hbar\frac{\partial}{\partial t}\psi'(x',t). \tag{3.7}$$

In this equation, we find the steady state by finding the eigenenergy and the eigenstate. If E_n and $\Psi_n(x')$ satisfy $\{-\frac{\hbar^2}{2m}\frac{\partial^2}{\partial x'^2} + \phi(x')\}\Psi_n(x') = E_n\Psi_n(x')$ (n is index of eigen state), the solution of (3.5) becomes

$$\psi_n(x,t) = e^{i(\frac{mvx}{\hbar} - \frac{mv^2t}{2\hbar}) - i\frac{E_nt}{\hbar}}\Psi_n(x - vt). \tag{3.8}$$

From this equation, we can see that the first-phase term is predetermined by the velocity of the SAW potential. This term does not change the phase difference between the electron states driven by the SAW potential, but it changes the global phase. Thus, the electron state is only controlled by the eigenenergy term. The calculation of an electron state after the transport thus becomes a time-independent problem.

If the driven electron enters a tunnel-coupling region, the Hamiltonian is modified to include the two propagation channels and the tunnel-coupling between them as (3.1). If only the ground state at each channel were taken into account, the calculation of tunneling would be reduced to the eigenvalue problem of the Hamiltonian. The equation that must be solved (the one following (3.7)) is now $\{-\frac{\hbar^2}{2m}\frac{\partial^2}{\partial x'^2} + \phi(x') + H_\tau\}\Psi_0(x')\,|\pm\rangle = (E_0 + E_\pm)\Psi_0(x')\,|\pm\rangle$. Here, the wave function is decomposed into the spatial distribution term and the pseudo-spin term that describes the occupation of either channel. Using an eigenenergy of H_τ, the phase acquired through time evolution is calculated. The state after the time evolution is initially $|\uparrow\rangle$, ignoring the global phase.

$$|fin\rangle = \langle +|\uparrow\rangle\, e^{-i\frac{E_+T}{\hbar}}\,|+\rangle + \langle -|\uparrow\rangle\, e^{-i\frac{E_-L}{\hbar}}\,|-\rangle\,. \tag{3.9}$$

$T = L/v$ is the dwell time of the electron traveling from the entrance to the exit of the tunnel-coupled wire. $\frac{(E_+ - E_-)T}{\hbar} = \frac{\sqrt{\epsilon^2+4t^2}L}{\hbar v}$ is the phase difference between the two eigenstates. The distinction of the phase difference between the free electron and the SAW-driven transport originates only from the difference of the velocity of electron transport. The oscillation pattern for the free electron shown in Figure.3.2 is therefore common for SAW-driven electron except for the energy range.

3.1.3 Adiabatic and non-adiabatic transport

In the above two sections, the Hamiltonian describes only the tunnel-coupled region of tunnel-coupled wires. In a real experimental setup, however, the connection from the zero and non-zero tunneling energy regions is important. Therefore, the time dependence of the Hamiltonian is

important for describing a more realistic time evolution of the electron state in the tunnel-coupled wire. In this section, we investigate how the SAW-driven electronic state evolves over time by using a time-dependent two-level Hamiltonian. For this purpose, the time evolution through the entire tunnel-coupled wire is first seen from different aspects.

Figure.3.3(a) schematically shows a typical time and space dependency energy diagram of an electron traveling through the tunnel-coupled wire. On the left side of the figure, the electron has not yet reached the tunnel-coupled region, and its eigenstates are $|\uparrow\rangle$ and $|\downarrow\rangle$ in the two-level model. Then, when the electron is injected into the tunnel-coupled region, the eigenstate becomes $|-\rangle$ and $|+\rangle$. After traveling through tunnel-coupled region, the eigenstate becomes $|\uparrow\rangle$ and $|\downarrow\rangle$ again. The time evolution of the state is described by two processes. The first is the state evolution at the two connections between the zero and non-zero tunneling-energy region. The ratio of the electron injection into the two eigenstates of the latter region depends on the time evolution process at these connections. The second is the phase acquisition process at the tunnel-coupled region. Owing to the energy difference between $|-\rangle$ and $|+\rangle$, these two states acquire different phases. The final state of the electron is decided by this phase difference. This energy diagram resembles that of a Mach–Zehnder interferometer, although the electron state is not separated in space but in energy. The transmission of the electron traveling from the upper channel to the upper channel, $T_{\uparrow\uparrow}$, is described as follows:

$$T_{\uparrow\uparrow} = T_{1\uparrow-}T_{0-\uparrow} + T_{1\uparrow-}T_{0-\uparrow} + 2\sqrt{T_{1\uparrow+}T_{0-\uparrow}T_{1\uparrow-}T_{0+\uparrow}}\sin\phi. \tag{3.10}$$

Here, T_{ijk} denotes the transmission from state k to state j at connection i. $T_{0-\uparrow}+T_{0+\uparrow} = T_{1\uparrow-}+T_{1\uparrow+} = 1$ is thus satisfied. ϕ is the phase difference acquired because of the energy difference between $|-\rangle$ and $|+\rangle$. However, this includes the phase of the transmission and reflection coefficient. Full coherent tunneling is observed only when $T_{0-\uparrow} = T_{0+\uparrow} = T_{1\uparrow-} = T_{1\uparrow+} = 0.5$. If the transmission differs from 0.5, the ratio of the oscillation component in $T_{\uparrow\uparrow}$ is suppressed.

The electron-state beam splitting at the connections depends not only on the detuning and tunneling energies in the tunnel-coupled region, but it also depends on the time evolution process at the two connections. For simplicity, we consider a simple model wherein the tunneling energy increases linearly with time at connection 0 and evaluate $T_{0+\uparrow}$. The Hamiltonian of the system is

$$H_\tau(t) = \frac{\epsilon}{2}|\uparrow\rangle\langle\uparrow| - \tau(t)|\uparrow\rangle\langle\downarrow| - \tau(t)|\downarrow\rangle\langle\uparrow| - \frac{\epsilon}{2}|\downarrow\rangle\langle\downarrow|, \tag{3.11}$$

where the tunneling energy, τ, is shown in Figure.3.3(b). Three parameters (i.e., maximum tunneling energy $\tau_{\max}$, time length in the connection Δt, and detuning energy ϵ (a fixed constant during time evolution)) determine the transmissions of $T_{\uparrow\uparrow}$. Note that considering the pseudo-spin term in the entire Hamiltonian is enough, because only this term determines the transmittances. Figure.3.3(c) shows $T_{0-\uparrow}$ as a function of Δt and ϵ at a fixed $\tau_{\max}$. The larger Δt corresponds to the slower tunneling-energy variation, where the transmission is more likely to differ from 0.5. Note that a new parameter set with $\epsilon' = \alpha\epsilon$, $\tau'_{\max} = \alpha\tau_{\max}$, and $\Delta t' = \frac{\Delta t}{\alpha}$ produces the same figure.

$T_{1\uparrow-}$ and $T_{0-\uparrow}$ are identical if the same parameters are used, although tunneling energy decreases linearly from $\tau_{\max}$ to zero in Connection 1 (exit side). The reason is as follows. First, we observe

the equations of these transmissions:

$$T_{0-\uparrow} = \langle\uparrow|\,\widetilde{\mathrm{T}}e^{i\frac{\int_0^{\Delta t} H_\tau(t)dt}{\hbar}}\,|-\rangle\,\langle-|\,\mathrm{T}e^{-i\frac{\int_0^{\Delta t} H_\tau(t)dt}{\hbar}}\,|\uparrow\rangle \tag{3.12}$$

$$T_{1\uparrow-} = \langle-|\,\widetilde{\mathrm{T}}e^{i\frac{\int_0^{\Delta t} H_\tau(\Delta t-t)dt}{\hbar}}\,|\uparrow\rangle\,\langle\uparrow|\,\mathrm{T}e^{-i\frac{\int_0^{\Delta t} H_\tau(\Delta t-t)dt}{\hbar}}\,|-\rangle = \langle\uparrow|\,\widetilde{\mathrm{T}}e^{-i\frac{\int_0^{\Delta t} H_\tau(t)dt}{\hbar}}\,|-\rangle\,\langle-|\,\mathrm{T}e^{i\frac{\int_0^{\Delta t} H_\tau(t)dt}{\hbar}}\,|\uparrow\rangle\,. \tag{3.13}$$

Thus, T is a time-ordering operator, and $\widetilde{\mathrm{T}}$ is an inverse time-ordering operator. $\widetilde{\mathrm{T}}e^{i\frac{\int_0^{\Delta t} H_\tau(\Delta t-t)dt}{\hbar}} = \mathrm{T}e^{i\frac{\int_0^{\Delta t} H_\tau(t)dt}{\hbar}}$ is used in (3.13). The eigenstate, Ψ_0 (see the expression above (3.9)), can be considered a real function, because it is in a 1D confined state. Reflecting this, H_τ is a real operator. Therefore,

$$(\langle-|\,\mathrm{T}e^{i\frac{\int_0^{\Delta t} H_\tau(t)dt}{\hbar}}\,|\uparrow\rangle)^* = \langle-|\,\mathrm{T}e^{-i\frac{\int_0^{\Delta t} H_\tau(t)dt}{\hbar}}\,|\uparrow\rangle\,, \tag{3.14}$$

where * indicates a complex conjugate. By using $T^*_{1\uparrow-} = T_{1\uparrow-}$, $T_{0-\uparrow} = T_{1\uparrow-}$ for the inverse variation of the tunneling-energy with time is obtained.

In Figure.3.3, the transmission is 0.5 at any Δt if detuning is zero. However, in reality, detuning cannot be kept constant. Detuning is possibly non-zero at least in some part of the connections. For non-zero detuning, the transport velocity of an electron critically affects the transmission. The connections have a certain length while not being clearly defined, owing to the potential slope at that location (see the next section). In the case of the Fermi velocity, the time duration in which the electron passes through the connection should be less than 1 ps. However, in the case of an electron trapped by a SAW, the time duration should be several-10 ps. Therefore, transmission can be more distinct from 0.5 at a non-zero detuning. From this perspective, it is possible that the coherent beam splitter for the SAW-driven electron will not allow us to fully tune its transmission. The dependency of transmission on Δt is, simply put, caused by the adiabaticity of transport.

The description of this section is instructive. However, it is insufficient for evaluating the electron transport in a real device. Therefore, in the next section, more detailed simulation is considered.

3.2 Time evolution of a SAW-driven electron in a realistic electrical potential

The above two-level model does not include any concrete situation characterized by a real potential structure, resulting a more complicated time evolution process and the existence of a higher excited state in each channel. In this section, I present numerical calculations of the time evolution of the electron state for a realistic electrical potential that accounts for all of the above factors. One of the most important steps for this numerical calculation is the estimation of a realistic potential in the device. For this purpose, I use the FEM calculation and solve the Laplace equation by assuming a fixed electrical potential at the gate electrode and the 2DES. The FEM calculation is first explained in this section. Then, the method of simulating the time evolution of the SAW-driven electron in the electrical potential is explained. Finally, the result of numerical simulation is shown with some gate-voltage configurations. The results presented in this section are useful to understanding the experimental results shown in Section 3.3.

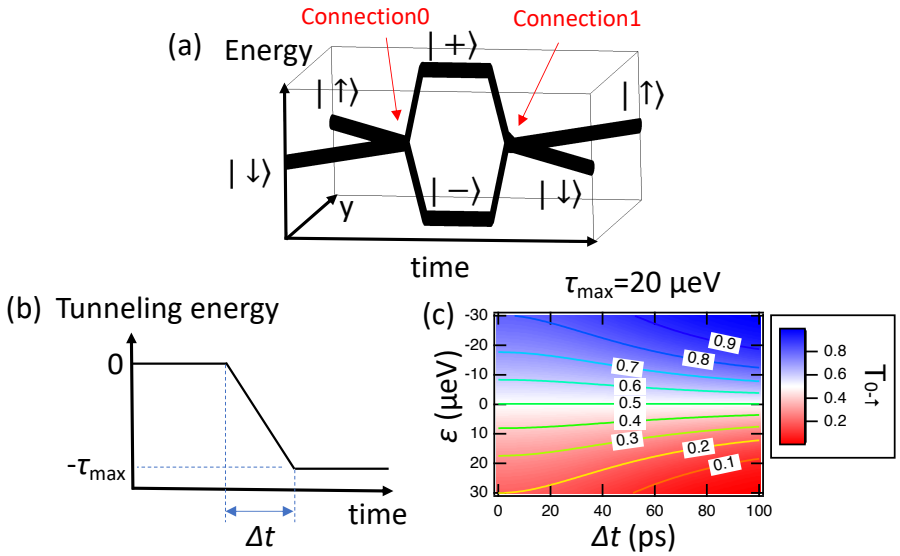

Figure 3.3: (a) Schematic time- (x-axis) and space- (y-axis) dependent energy diagram of a two-level model, in which the presence of an electron in either of the upper $|\uparrow\rangle$ or the lower $|\downarrow\rangle$ moving quantum dot is used as the two bases. The eigenenergy of an electron evolves with time from left to right. (b) Time-dependent tunneling energy used for calculation. (c) $T_{0-\uparrow}$ is calculated.

3.2.1 Potential calculation

Obtaining the electrical potential constructed by gate electrodes is an important task. If we have an accurate electrical potential, at least the single-electron-transport phenomena can be predicted. It is also useful for device designs. Although precise electrical potential is desired, it is still difficult to obtain. This difficulty is not generally caused by quantum-mechanical reasons. Our device is developed with many contrivances to achieve high mobility. 2DES is formed by an electrical field created by unoccupied dopants. There are also surface states or impurity states that trap additional electrons in the surface of semiconductors. How electrons and dopants are distributed is an important consideration that depends on the fabrication process and the existence of gate electrodes. The cooling process in the fridges is also important. Usually, the occupations of these states can be altered at room temperature. However, it is suppressed at lower temperatures.

Although such difficulty exists, most uncertain things do not play an important role in the qualitative discussion. This is because the background potential is nearly unchanged, even after we sweep the gate voltages. We also know that the potential defined by the gate voltage is dominant. Therefore, only the calculation of the electrical potential induced by the gate electrode and 2DES is worth doing. Moreover, the potential induced by the gate electrodes plays a leading role for controlling the transport of electrons. For this purpose, FEM is useful as a well-established technique for solving equations having boundary conditions. It is often used in the field of structural mechanics. Nowadays, it used in many other fields, such as for the calculation of electrical potential. Maxwell's equation is the equation for an electrical field. In our experiment, when the background charge is neglected, the Laplace equation can be used to simplify the problem.

Here, I explain FEM using a simple reference case shown in Figure.3.4(a). The electrical potentials at the left and right sides of the structure are fixed to ϕ_0 and $\phi_3 = 0$. The structure is virtually divided into three sub-structures having different lengths. These are called "elements". FEM terminology comes from the use of finite arbitrary-size element that is used for the calculation. In this problem, we calculate the internal electrical potential. The equation that must be solved is the Laplace equation, $\Delta^2\phi = 0$. First, it is assumed that the potential in each element can be described by using the potential at the vertex (edge in the 1D case) of the element. For simplicity, the internal potential in the center element is described by

$$\phi(x) = \frac{(x - x_1)\phi_2 + (x_2 - x)\phi_1}{L_2}. \tag{3.15}$$

This equation corresponds to taking the average of ϕ_1 and ϕ_2 with the weight of distances from the edges. $\phi(x)$ is illustrated in Figure.3.4(b). The necessary conditions for FEM are that the potential and its derivative are continuous between neighboring elements. This requirement comes from the integral of the Laplace equation. If charge accumulation exists, the derivative should jump between neighboring elements. Thus, the equations become

$$\frac{\phi_2 - \phi_1}{L_2} = \frac{\phi_1 - \phi_0}{L_1}, \tag{3.16}$$

$$\frac{-\phi_2}{L_3} = \frac{\phi_2 - \phi_1}{L_2}. \tag{3.17}$$

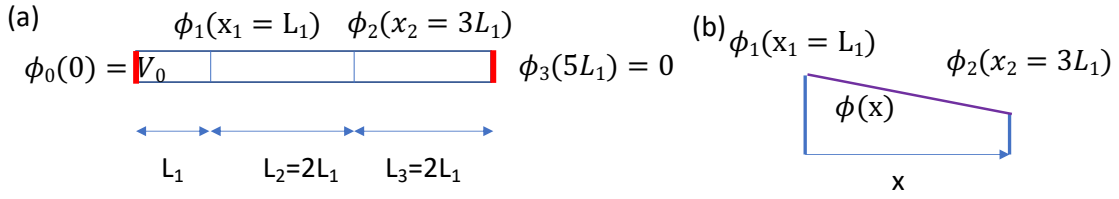

Figure 3.4: Example of FEM calculation.

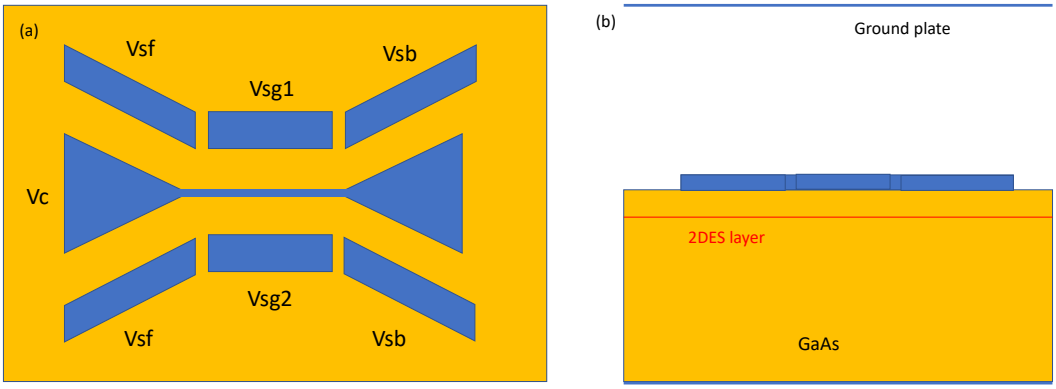

Figure 3.5: False scale image of FEM design. (a) Top view. (b) Side view.

This is done by using the continuity of the derivative to the connection between left and center elements and between center and right elements. It is thus possible to determine all ϕ_i (i=1,2). The internal potential can also be calculated by using (3.15). The boundary condition of the fixed derivative of ϕ can also be used instead of ϕ. For more complicated problems having larger dimensions, it is necessary to expand this concept based on the same idea. The potential of a realistic device is calculated for 3D space.

The design of gate electrodes for the potential calculation is shown in Figure Figure.3.5. The entire calculation space size is about 6,000 nm × 9,000 nm × 2 mm. I assume that the metallic ground plate at the top and bottom of the calculation space 1-mm away from the 2DES, although it does not play an important role. The zero-electrical-field boundary condition is adopted at the side facets of the calculation space. Metal electrodes are put onto the surface of GaAs. Electrical potentials at the electrodes are constant and define the boundary conditions. The voltages applied to the gate electrodes determine the potential profile of the device. The dielectric constant of GaAs is 13, and that of vacuum above GaAs is 1.

2DES is also included in the calculation. It is 125 nm below the surface of the GaAs. To account for the influence of the 2DES, we first calculate its area when -1 V is applied for all gate electrodes. This voltage is close to that applied in the experiment. The procedure is illustrated in Figure.3.6. Initially the 2DES is treated as a zero-potential boundary. However, the area of the

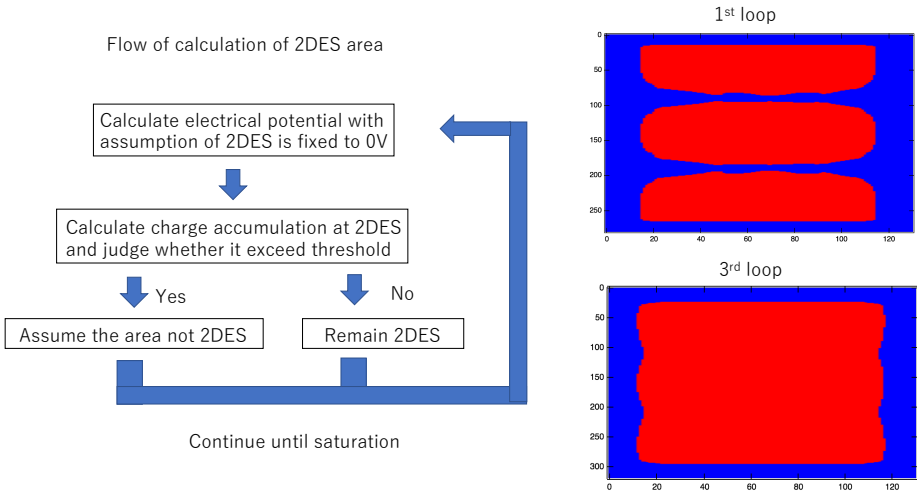

Figure 3.6: Flow of the calculation process of the 2DES area. Right two figures indicate the element wherein the 2DES remains (depleted) with blue (red). Note that horizontal and vertical coordinates represent the order of elements and not the real space size, because each element size is not the same.

2DES is reduced by calculating the positive-charge accumulation (reduction of electrons) in the 2DES from the electrical field of the nearby element. I then compare it with the sheet density, 1.46×10^{11} cm^{-2}, of the wafer used in experiment. If the accumulated charge density exceeds the sheet density, the area is assumed to be depleted and is treated as a normal element of GaAs. After repeating this potential calculation several times, I find the area of the remaining 2DES. In the right side of Figure.3.6, interim results of the calculation are plotted. In our experimental setup, the channels are always depleted. Indeed, around those voltage (-1 V for all gate electrodes), 2DES is also found to be depleted in the calculation. 2DES only exists far from the channels. However, 2DES is important to the construction of a transport channel for the electrons. If there is no 2DES, the electrical potential between the gate electrodes is simply given by their average, and the channels are not constructed. If the voltage applied to the electrodes changes, the 2DES area also changes in a real situation. However, we assume that the 2DES area is fixed in the latter calculation to suppress the calculation time. I used the 2DES area calculated using the -1-V gate voltage. After the 2DEG area is determined, the electrical potential maps defined by each gate electrodes are calculated. The potential structure changes linearly with the gate voltage via this method. Therefore, the calculation time is reduced.

Figure.3.7 shows an example of the result of the FEM potential calculation for $V_c = -1$ V, V_{sf}=-1.2 V, V_{sb}=-1.3 V, V_{sg1}=-1.38 V, and V_{sg2}=-1.42 V (see Figure.3.5 for the gate electrode indices). I am unsure whether the absolute potential value is appropriate, because there should be a background potential source. However, at least the potential structure becomes that of a tunnel-coupled wire. Note that the voltage used for potential calculation is not the same as those of the experiment (see

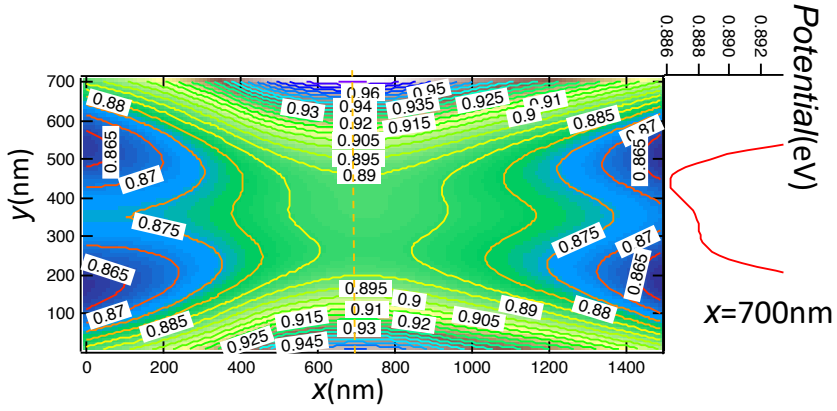

Figure 3.7: Example of potential structure calculated with V_c=-1 V, V_{sf}=-1.2 V, V_{sb}=-1.3 V, V_{sg1}=-1.38 V, and V_{sg2}=-1.42 V.

next section), because the center potential barrier is not well-formed at the smaller negative gate voltage used in my experiment. V_c=-0.7 V in the experiment, whereas V_c=-1 V in the numerical calculation. This may seem to be a big difference. However, it might be caused by my calculation not including the potential modification caused by the presence of the gate electrode via the change the dopant-charge distribution. Although this small discrepancy exists, the calculation is useful for qualitative discussions on the electron transport in a tunnel-coupled wire.

I have not added the potential induced by the SAW, although it is important to the experiment. It is, in principle, possible to calculate the SAW potential using the FEM. However, it is not easy to implement the program. I simply assume that the SAW potential is a sinusoidal potential that propagates at the velocity of 2.7 km/s, and I, therefore, neglect the interaction between the SAW potential and the other structures. This assumption is justified by the fact that the interaction between the SAW and the thin-gate electrodes is weak [79]. Moreover, the electrical potential at the center of the channel is nearly independent of the existence of the gates [80]. The SAW potential amplitude is assumed to be 20 mV. This value comes from experimental observations that used an unintended impurity in the experimental device, adopting the technique mentioned in the last section of the previous chapter.

Finally, I comment on the numerical calculation itself. Hexahedron-shaped elements of appropriate sizes are used for reproducing the device structure. In the calculation, the PARDISO solver package is used for solving the linear equation made from the large sparse matrix. The entire program is written in FORTRAN, including the structural design.

3.2.2 Calculation of time-dependent Schrödinger equation

I use the calculation method proposed by N. Watanabe et al. [**?**] to simulate the time evolution of single electrons. This subsection is thus devoted to explaining their method. The method allows us

to calculate in a simply discretized space and time with optimized calculation orders. This makes calculation time linear to the number of divisions in space. Thus, it is successful for completing entire calculations, including those of relatively higher eigenmodes, which are often discarded during calculation, in a finite time using a supercomputer. For example, I explain the calculation method for a 1D system for simplicity, because 2D cases are too similar to the simple expansion of the 1D case.

In a 1D case, the Hamiltonian is simply written as

$$H(x,t) = -\frac{\hbar^2}{2m}\frac{\partial^2}{\partial^2 x} + \phi(x,t). \tag{3.18}$$

The potential term is diagonalized by using the space base, whereas the kinetic term is not. The kinetic term includes the derivative by space, which is treated as a hopping term to the neighboring discrete space. These two terms are not commutable. It is thus difficult to find a good basis for treating both potential and kinetic terms simultaneously. These terms are, therefore, calculated separately. As a simple method, time evolution is calculated by

$$\psi(x,t+\Delta t) = e^{-\frac{iH(x,t+\frac{\Delta t}{2})\Delta t}{\hbar}}\psi(x,t). \tag{3.19}$$

Δt is the time difference between the time steps of the calculation when using the finite difference method. Kinetic and potential terms are separated by using Suzuki's exponential product theory:

$$\psi(x,t+\Delta t) \approx e^{\frac{i\hbar\Delta t}{4m}\frac{\partial^2}{\partial^2 x}} e^{\frac{-i\phi(x,t+\frac{\Delta t}{2}\Delta t)}{\hbar}} e^{\frac{i\hbar\Delta t}{4m}\frac{\partial^2}{\partial^2 x}}\psi(x,t). \tag{3.20}$$

I must calculate each exponential term step-by-step. First, I explain how the kinetic term is calculated. This term is treated by the relation, $\frac{\partial^2}{\partial^2 x}\psi(x) = \sum_i \frac{\psi(x_{i+1})-2\psi(x_i)+\psi(x_{i-1})}{\Delta x^2}$, in discrete space. Here, $x_i = i\Delta x + x_0$ has an integer, i, and Δx is the space difference between neighboring spaces. When it is written in matrix form, the matrix is tridiagonal and Toeplitz, giving it the same matrix elements along the diagonal direction. The eigenvalues and vectors are well known for these kinds of matrices. Therefore, it is possible to perform exact diagonalization, although it is time consuming. Instead, we use another approximation method to include everything up to the first order of the exponential. As a starting point for calculating the kinetic term, I suppose that the other term is already calculated. For example, ψ' is known as follows. The modified equation from (3.20) is

$$e^{-\frac{i\hbar\Delta t}{8m}\frac{\partial^2}{\partial^2 x}}\psi(x,t+\Delta t) = e^{\frac{i\hbar\Delta t}{8m}\frac{\partial^2}{\partial^2 x}}\psi'(x,t), \tag{3.21}$$

$$\psi'(x,t) = e^{\frac{-i\phi(x,t+\frac{\Delta t}{2}\Delta t)}{\hbar}} e^{\frac{i\hbar\Delta t}{4m}\frac{\partial^2}{\partial^2 x}}\psi(x,t). \tag{3.22}$$

Then, (3.21) is approximated as

$$(1 - \frac{i\hbar\Delta t}{8m}\frac{\partial^2}{\partial^2 x})\psi(x,t+\Delta t) = (1 + \frac{i\hbar\Delta t}{8m}\frac{\partial^2}{\partial^2 x})\psi'(x,t). \tag{3.23}$$

Here, $\frac{1+\frac{i\hbar\Delta t}{8m}\frac{\partial^2}{\partial^2 x}}{1-\frac{i\hbar\Delta t}{8m}\frac{\partial^2}{\partial^2 x}}$ is a unitary matrix. Thus, conservation of the probability is satisfied. This equation is described in matrix form as

$$\begin{pmatrix} A & -1 & 0 & 0 & & \\ -1 & A & -1 & 0 & \dots & \\ 0 & -1 & A & -1 & & \\ & \vdots & & & A & -1 \\ & & & & -1 & A \end{pmatrix}\begin{pmatrix} \psi(x_1, t+\Delta t) \\ \psi(x_2, t+\Delta t) \\ \vdots \\ \\ \psi(x_n, t+\Delta t) \end{pmatrix} = \begin{pmatrix} B & 1 & 0 & 0 & & \\ 1 & B & 1 & 0 & \dots & \\ 0 & 1 & B & 1 & & \\ & \vdots & & & B & 1 \\ & & & & 1 & B \end{pmatrix}\begin{pmatrix} \psi'(x_1, t) \\ \psi'(x_2, t) \\ \vdots \\ \\ \psi'(x_n, t) \end{pmatrix}. \tag{3.24}$$

In this equation,

$$A \equiv -i\frac{8m\Delta x^2}{\hbar\Delta t} + 2, \qquad B \equiv -i\frac{8m\Delta x^2}{\hbar\Delta t} - 2. \tag{3.25}$$

Equation (3.24) is then reduced into lower–upper (LU) decomposition form as

$$\begin{pmatrix} u_1^{-1} & 0 & 0 & & \\ -1 & u_2^{-1} & 0 & \dots & \\ 0 & -1 & u_3^{-1} & & \\ & \vdots & & & 0 \\ & & & -1 & u_n^{-1} \end{pmatrix}\begin{pmatrix} 1 & -u_1 & 0 & & \\ 0 & 1 & -u_2 & \dots & \\ 0 & 0 & 1 & & \\ & \vdots & & & -u_{n-1} \\ & & & & 1 \end{pmatrix}\begin{pmatrix} \psi(x_1, t+\Delta t) \\ \psi(x_2, t+\Delta t) \\ \vdots \\ \\ \psi(x_n, t+\Delta t) \end{pmatrix} = \begin{pmatrix} b(x_1, t) \\ b(x_2, t) \\ \vdots \\ \\ b(x_n, t) \end{pmatrix}, \tag{3.26}$$

where

$$b(x_i) \equiv \psi'(x_{i-1}, t) + B\psi'(x_i, t) + \psi'(x_{i+1}, t) \tag{3.27}$$

$$u_i \equiv \frac{1}{A - u_{i-1}}, \quad u_0 \equiv 0, \quad \psi'(x_0, t) \equiv 0, \quad \psi'(x_{n+1}, t) \equiv 0. \tag{3.28}$$

Calculation of (3.26) can be conducted by using the auxiliary vector, $\boldsymbol{c}$.

$$\begin{pmatrix} c(x_1, t) \\ c(x_2, t) \\ \vdots \\ \\ c(x_n, t) \end{pmatrix} = \begin{pmatrix} 1 & -u_1 & 0 & & \\ 0 & 1 & -u_2 & \dots & \\ 0 & 0 & 1 & & \\ & \vdots & & & -u_{n-1} \\ & & & & 1 \end{pmatrix}\begin{pmatrix} \psi(x_1, t+\Delta t) \\ \psi(x_2, t+\Delta t) \\ \vdots \\ \\ \psi(x_n, t+\Delta t) \end{pmatrix}. \tag{3.29}$$

Doing so, $\boldsymbol{c}$ is directly calculated from $\boldsymbol{b}$ using (3.26). The simultaneous equation is easily solved in the order from top to bottom. Then, the elements of $\boldsymbol{c}$ are determined as

$$c(x_1, t) = u_1 b(x_1, t), \qquad c(x_i, t) = u_i(b(x_i, t) + c(x_{i-1}, t)). \tag{3.30}$$

Finally,

$$\psi(x_n, t+\Delta t) = c(x_n, t), \qquad \psi(x_i, t+\Delta t) = c(x_i, t) + u_i\psi(x_{i+1}, t+\Delta t) \tag{3.31}$$

is obtained by calculating (3.29) in the order from bottom to top.

Calculation of the potential term is quite simple, because the description of the wave function in the space base diagonalizes the term.

$$e^{\frac{-i\phi(x,t+\frac{\Delta t}{2}\Delta t)}{\hbar}} = \begin{pmatrix} e^{-i\frac{\psi(x_1,t+\frac{\Delta t}{2})}{\hbar}} & 0 & & \\ 0 & e^{-i\frac{\psi(x_2,t+\frac{\Delta t}{2})}{\hbar}} & \cdots & \\ & \vdots & & \\ & & & e^{-i\frac{\psi(x_n,t+\frac{\Delta t}{2})}{\hbar}} \end{pmatrix}. \tag{3.32}$$

Repeating the calculation of the kinetic and potential terms at each step, the time evolution of a single electron is achieved. Expansion to a 2D system is also possible. Although the derivative by x and y is commutable (x and y are diagonal coordinates of space), it is easy to calculate both terms separately by using the above-mentioned calculation technique. Therefore, calculation of the kinetic term for the two directions is possible by properly inserting the operation, which arranges the order of the space basis in the vector, ψ, as shown in Figure.3.8, depending on the direction the kinetic term is to be calculated.

The above calculation program is implemented using FORTRAN. This is because FORTRAN and C languages are faster for numerical calculations, compared with other programming languages. A free standard-solver package (i.e., LAPACK) is distributed for the given languages. In the case of my program, solving the eigenstate problem relies on this capability. It is thus necessary to find out the initial electron-wave function. For more difficult problems, I rely on another solver program. In the calculation of the potential using FEM, it is necessary to calculate a linear equation with a sparse matrix for solving the relationships with neighboring elements. I used Intel ' s MKL PARDISO for this purpose. These calculation packages are already installed in the supercomputer at the University of Tokyo. I used the supercomputer for this research, and the following results of Figure.3.7 were obtained by it. The supercomputer allows parallel calculations, and the calculation for Figure Figure.3.10 finishes within 24 h.

3.2.3 Intuitive picture of gate-control tunneling

Next, the program of simulating the time evolution of the SAW-driven electron in its electrical potential calculated by FEM is ready. Here, it is necessary to investigate how to tune the gate voltage to observe the tunnel oscillation. As was already seen in Section 3.1.2, tunnel oscillation is determined by the time duration in the tunnel-coupled region, the tunneling energy (τ), and the detuning energy (ϵ). For the SAW-driven electron, the time duration depends only on the device size and is therefore uncontrollable. Thus, the other two energy factors can be controlled via the electrical potential generated by applying voltage on the gate electrodes. See Figure Figure.3.5.

In the design of the gate pattern shown in Figure.3.5, the most important gate is the center one, V_c, and the two side gates, V_{sg1} and V_{sg2}. For fixing the side-gate voltages, V_c directly controls the center potential barrier and the tunneling energy, maintaining the detuning energy at a constant level. On the other hand, for the fixed-center-gate voltage, V_{sg1} and V_{sg2} can be used to modify the potential structure, as shown in Figure.3.9. This figure shows the potential cross section along the y direction (see Figure.3.7). A new set of gate parameters is thus defined as $V_{gd} = V_{sg1} - V_{sg2}$

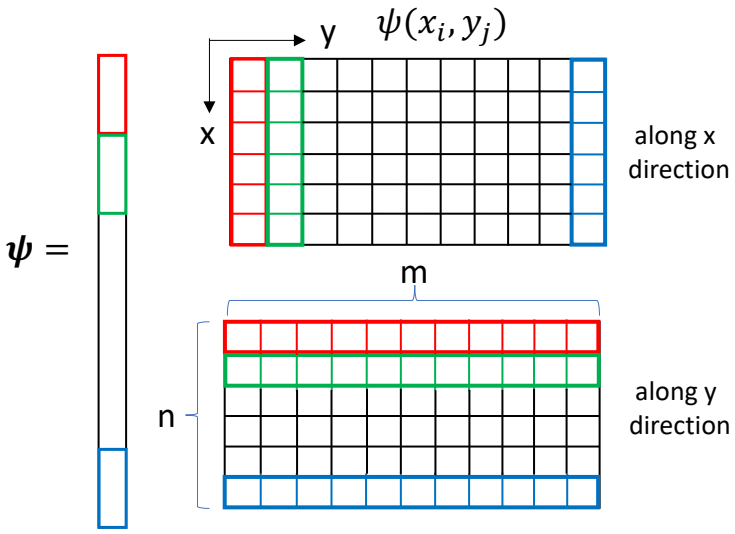

Figure 3.8: Constructing ψ in proper order for calculating the time evolution of an electron. Calculating the kinetic term in x and y directions requires an arrangement of the order of elements in ψ.

and $V_{\text{gs}} = \frac{V_{\text{sg1}}+V_{\text{sg2}}}{2}$. By controlling these gate parameters, the potential structure is assumed to be modified. V_{gd} controls the detuning energy, and V_{gs} controls the tunneling energy. The latter is done, because the center potential barrier becomes relatively small when increasing the potential in both the upper and lower channels. Next, the probability of the output electron staying in the same channel as the injection channel is calculated as a function of V_{gd} and V_{gs}. The probability can experimentally be measured as the output current.

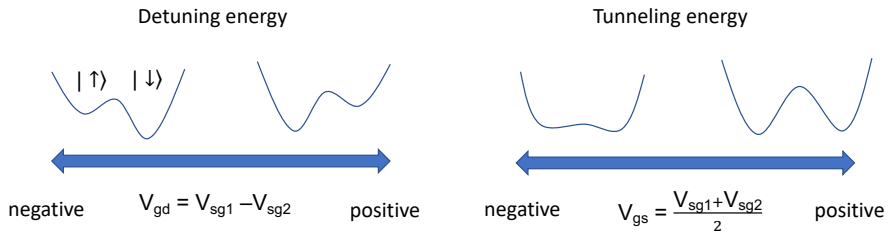

Figure 3.9: How the two side gates V_{sg1} and V_{sg2} control the electrical potential.

3.2.4 Result of calculation

The numerical calculation result in Figure.3.10 shows the probability that the electron propagating through the tunnel-coupled wire ejects from the lower channel when the electron is injected from that channel. The potential structures of the transport channels are calculated using FEM under the assumptions described in the previous section. The electron is transported by the SAW potential, which is assumed to comprise a 20-mV amplitude sinusoidal wave. The initial state of the electron is assumed to be the ground state trapped in the SAW potential minimum. The device design is basically the same as the one used in my experiment. However, the length of the tunnel-coupling region is shortened to 500 nm to reduce calculation time. The gate voltages are set close to the values used in the experiment (see next section), except for the center-gate voltage (V_c). In Figure.3.10(a), we calculate for the case in which the gate voltages are $V_{\rm c} = -1$ V,$V_{\rm sf} = -1.1$ V and $V_{\rm sb} = -1.2$ V. Figure.3.10(b) shows the results at $V_{\rm c} = -1$ V, $V_{\rm sf} = -1.1$V, and $V_{\rm sb} = -1$ V. In Figure.3.10(a), the electron is fully trapped by the SAW potential. However, the electron is dropped off at the exit of the tunneling region in Figure.3.10(b). Details are discussed later. These two figures present the results that should be observed as a current in the experiment. To see the origin of these current patterns, the electron state during the time evolution is investigated.

The time evolution at each marked gate-voltage point in Figure.3.10 is calculated in Figure.3.11(a)–(c). The red (green) line indicates the ratio of the probability distribution of the electron in the upper (lower) region, $P_\uparrow$ ($P_\downarrow$), as a function of the time spent from the initial state. Here, the electron is assumed to be injected from the lower channel. Initially at time zero, the electron is in the lower channel with a 100% probability. At *time*=100 ps, the electron enters the tunnel-coupled region. The electron can hop to the other channel, causing the probability distribution to change in this region. Then, at the exit of the tunnel-coupling region, the tunneling energy goes to zero, and the final electron state is determined. At (a) and (c), the electron tunnels only once to the other channel. At the dips in the probability distribution along the topmost dashed line (red region in Figure.3.10), the tunnel oscillation number is only one. On the other hand, along the second topmost dashed line, the electron tunnels three times, as shown in Figure.3.11(b). The increase of the number of tunnelings with the decrease of $V_{\rm gs}$ is consistent with the picture shown in Figure.3.9.

Figure.3.11(d)–(f) show the accumulation of 24 datasets of the spatial probability distribution at fixed time intervals of 15.4 ps. Over the 24 datasets, the SAW travels by 1 μm. The electron trajectories at each marked gate voltage are presented as results. The electron is initially prepared at the left lower side and conveyed by the SAW to the right. From these figures, it is possible to identify the electron state that couples to the ground state of the injected electron. In Figure.3.11(d), the trajectory of the electron in the upper channel is a single line. This indicates that the upper channel state that couples to the ground state in the lower channel is the ground state. The resonance state is the ground state in the upper channel along the leftmost dot-dashed line in Figure.3.10(a). On the other hand, in Figure.3.11(e) and (f), the upper-channel trajectory splits into two lines. This indicates that the electron state that resonates with the ground state of the lower channel is the first excited state along the y direction in upper channel. This situation is common along the second leftmost dot-dashed line. In summary from these observations, the oscillation pattern in Figure.3.10 appears because of the increasing tunneling energy along $V_{\rm gs}$ and the energy alignment between the injected ground state and the higher-lying state in upper channel along $V_{\rm gd}$. The oscillation structure

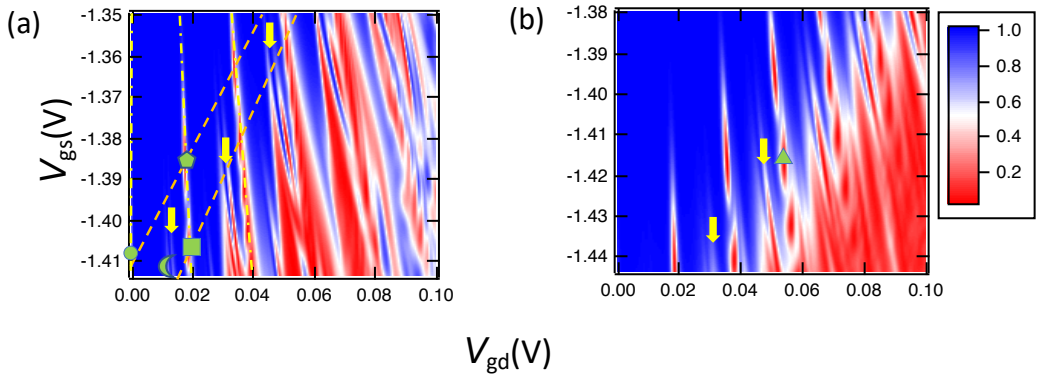

Figure 3.10: Numerically calculated probability of electron staying in the lower channel through the tunnel-coupled wire when the initial state is the ground state of the lower channel. The results are shown as a function of $V_{gd} = V_{sg1} - V_{sg2}$ and $V_{gs} = \frac{V_{gs1}+V_{gs2}}{2}$. (a) Typical result when electrons are fully trapped by the SAW potential during the time evolution. $V_c = -1$ V,$V_{sf} = -1.1$ V and $V_{sb} = -1.2$ V. (b) Typical result when a party of electrons drop off the SAW potential at the exit of the tunnel-coupled region. $V_c = -1$V,$V_{sf} = -1.1$ V and $V_{sb} = -1$ V

along V_{gs} completely originates from the tunneling oscillation discussed for the two-level model. Therefore, observation of the current oscillation along V_{gs} can be used as evidence of tunneling oscillation, and it is observed in the experiment, which will be explained later.

Note that the potential confinement along x direction (by the SAW) and y direction (by the gate electrodes) is almost independent. Therefore excitation along the x direction should also be considered. However, in these marked-gate voltages used in Figure.3.11, the electron state is the ground state along the x direction. The reason is that the injected ground-state electron and the higher excited state along the x direction in upper channel have smaller tunneling energies between them, because they are orthogonal wave functions. Excited states along the x direction appear at the more negative V_{gs} in Figure.3.10, as indicated with the yellow arrow where tunneling energy is higher. A snapshot of the spatial probability distribution in the tunnel-coupled region at the crescent-mark gate voltage in Figure.3.10(a) is plotted in Figure.3.12. The spatial probability distribution in the upper channel has one node along the x direction, indicating that the electron state is in resonance with the ground state in the lower channel and is the first excited state along the x direction in the upper channel.

The difference of gate voltages in Figure.3.10(a) and (b) is small, but the transport is greatly influenced. The electron is dropped from the moving potential by the SAW in (b). Figure.3.13 shows the time evolution of the electron with the gate voltages at the triangle mark in Figure.3.10(b). Until it reaches the center tunnel-coupling region, the electron is trapped by the SAW, and the observed trajectory is similar to that in Figure.3.11. However, at the exit of the tunnel-coupling region, the electron drops, because the electrical potential decreases more than does the confinement potential (see the contour plot of electrical potential in Figure.3.13(b)). The electron travels forward at a

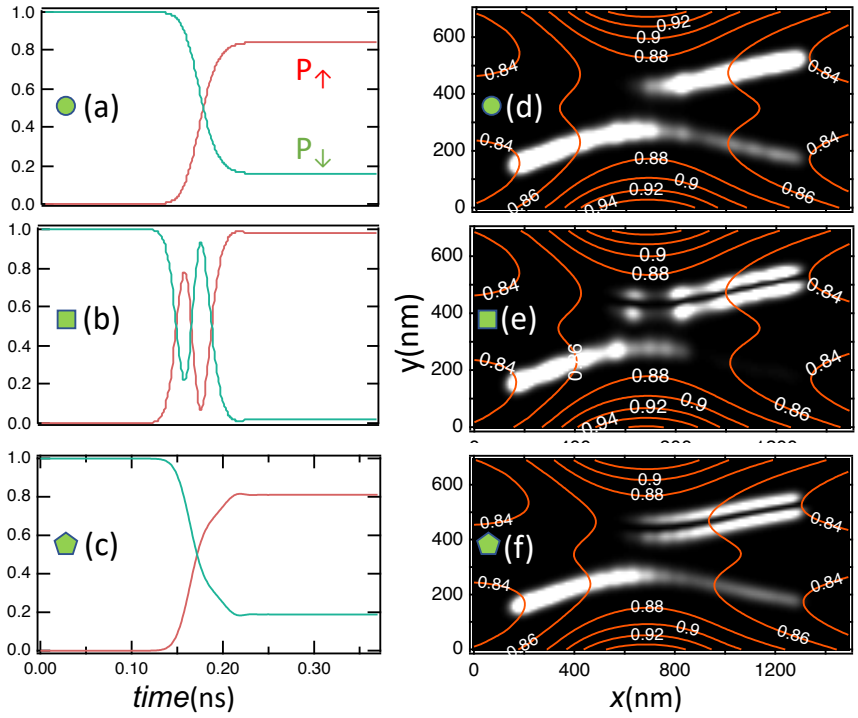

Figure 3.11: Calculated temporal and spatial distributions of an electron in the tunnel-coupled wire for each marked point in Figure.3.10a. (a)–(c) Probability of finding an electron in the lower channel, $P_{\downarrow}$ in green and upper channel, and $P_{\uparrow}$ in red, respectively at each time instance. (d)–(f) Cumulative spatial probability distribution of those obtained at time intervals of 15.4 ps with contour plots of the potential profile.

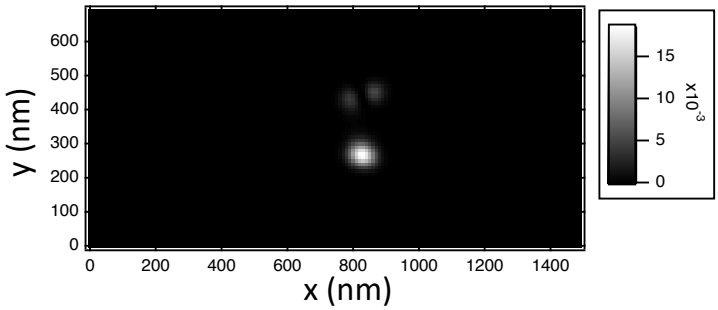

Figure 3.12: Example of the spatial probability distribution. The ground state in the lower channel is coupled with the first excited state along the x direction in the upper channel.

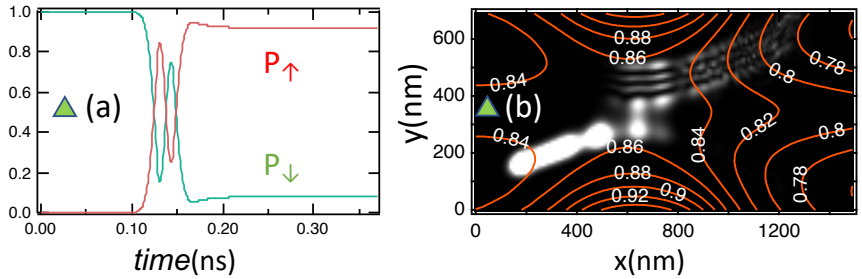

Figure 3.13: Temporal and spatial distribution of electron at the potential configuration where the electron is dropped from the SAW potential.

much faster speed than in the SAW after it drops, because the intensity of the probability becomes weak. A remarkable observation in this case is the more distinct current oscillation pattern, which is related to the adiabaticity/non-adiabaticity of the state evolution. If the electron is always confined by the SAW potential, its velocity is slow. Thus, the time evolution can be adiabatic, suppressing the current oscillation. However, if the electron drops, the state evolution can be considered non-adiabatic, and the current pattern becomes clearer. This situation coincides with the naive model considered in Subsection 3.1.3.

Figure.3.14 shows the result for the same parameters as those shown in Figure.3.10(a) but over a wider gate-voltage range. The initial state is the ground state in the left figure, but the first excited state for the transverse (y) direction is in the right figure. In the left figure, signal only appears at zero or positive V_{gd}. This is because no state in the upper channel can couple with the ground state in the lower channel for the negative V_{gd}. In the right figure, on the other hand, the signal appears, even for a slightly negative V_{gd}. This occurs when the initial state includes an excited state. It is, of course, difficult to make a precisely symmetric structure or to find out the actual zero detuning voltage. However, the knowledge of what will happen as a general tendency when the excited state is included in the initial state is helpful for understanding the experimental result.

In summary, we understand from the numerical simulation what should be observed in the real experiment. The current pattern obtained from simulation is different from the result obtained by a simple two-level model. It is thus necessary to consider higher excited states. The current pattern shown in Figure.3.2 does not appear as it is, because the efficiency of the gate voltage is different between the tunneling and detuning energies. Thus, it appears to be squeezed in the horizontal direction. If the pattern in Figure.3.10 is observed, it becomes possible to see that the demonstration of coherent tunnel oscillation is accomplished. In the next section, experimental observation of the tunnel oscillation is described.

3.3 Experimental result

The results obtained above are all theoretical. In this section, I explain the observation of the tunnel oscillation in a real experiment. In the first subsection, detail of the experimental setup and device

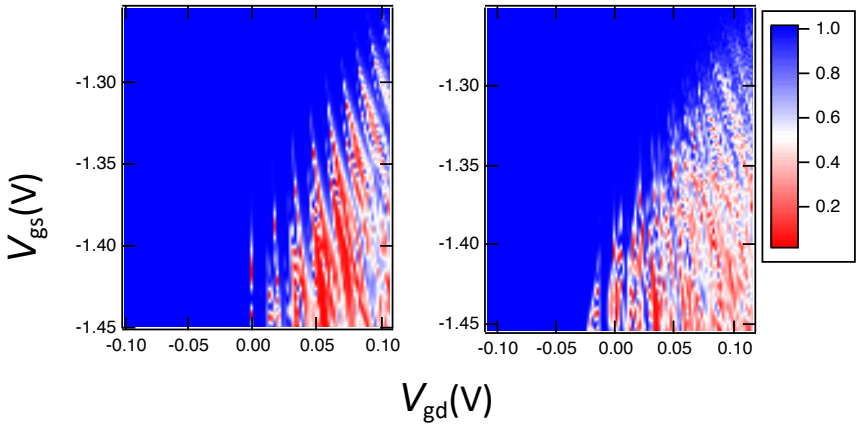

Figure 3.14: Larger gate voltage-area scan when the other gate voltages are the same as those in Figure.3.10(a). The initial state is the ground state (first excited state along y) in the left (right) of the figure.

is explained. In the second subsection, experimental results of the electron transport are described. An important concept for the SAW-driven current was already explained in the last section of the previous chapter. However, another unfamiliar feature is also observed. Such an observation implies that there is also unexpected ambiguity for understanding the SAW experiment. Then, the main tunnel oscillation result is explained.

3.3.1 Experimental device and setup

The device used is shown in Figure.3.15. On the right side, the main device structure is displayed. This picture was taken with a scanning electron microscope (SEM). Metal electrodes at the surface appear bright. The 2DES is formed below the surface, and the electrodes made of Au/Ti allows us to form 1D channels in the 2DES by applying voltage to them. The high electrical potential underneath them restrict the electron motion in the space between the gate electrodes. Two 1D channels (upper and lower) are formed by tuning the gate voltages. Both channels are connected to the 2D reservoirs and the Ohmic contacts represented by a white cross mark in the square frame. The Ohmic contact is a conductive structure wherein the 2DES is connected to the outer electric circuit. The upper and lower channels are connected at two tunnel-coupling regions. The whole device structure is designed to form a Mach–Zehnder interferometer. Additionally, the IDT is placed at the left to generate the SAW. The IDT is apart from the main structure by over 1 mm to suppress disturbances caused by direct electrical magnetic radiation emitted from the IDT. The IDT is made of the Au/Ti metal, just as the gate electrodes. The period of one finger is 1 μm for generating the SAW with a 1-μm wavelength. The number of IDT fingers for each side of the comb is 100. One side of the IDT comb is grounded.

The device is put into a Heliox VL, manufactured by Oxford Instruments. It is an He-3 cryostat. The device is cooled down to 260 mK nominally. In a realistic situation, microwaves that generate

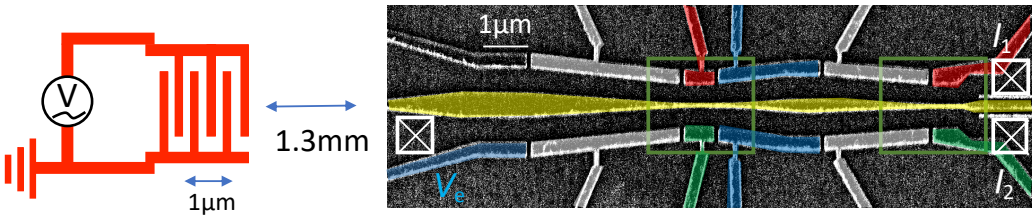

Figure 3.15: Whole-device structure. IDT is placed at the right 1.3-mm away from the main structure to the left. The main structure is made of two tunnel-coupling regions encircled by green frames. The entire structure is designed to form a Mach–Zehnder interferometer.

the SAW produces heat, and the operating temperature is 300 mK at its lowest. Note that the temperature is measured using a thermometer mounted on the Heliox. It is put far from the sample, because heating occurs locally at the IDT. Therefore, it is possible that the real device temperature is higher. In a later section, I show that the temperature is less effective on the experimental result.

The measurement circuit, device, and equipment configuration is shown in Figure.3.16. Only the main device and a low-pass filter is placed in the cryostat. The other equipment is operated at room temperature. The gate electrode and the left-side Ohmic contact are connected to a DC voltage source. The right-side Ohmic contacts are connected to the current/voltage (I/V)-converting current amplifier and voltage meter. As a voltage meter, a digitizer is used for future noise measurement. In this case, it was only used for DC measurement. One side of the IDT comb is connected to an RF generator. The other comb is grounded. A divider is placed midway to the Ohmic contact to improve accuracy and resolution of the voltage applied. Low-pass filters are inserted in line to the gate electrodes to protect the sample from sudden electrical shocks and to filter the high-frequency noise. The cut-off frequency is 150 kHz.

3.3.2 Quantization of current by SAW

The SAW becomes more effective after the channel is depleted. This is because the 2DES screens the electrical potential induced by the SAW. Following the pinch-off, the transport of the electron is driven by the SAW. However, quantization of the charge in each SAW potential minimum and that of the current are not realized only by simply applying the SAW. It requires careful tuning of the gate voltage, power, and frequency of the microwave. This is because the potential structure around the boundary between the 2DES and the 1D channel is critical for quantization of the current. Electrons that are carried must be strongly confined by the SAW potential, but excess electrons must escape to the reservoir at the same time.

Figure.3.17 shows quantization of the current observed by applying a SAW as a function of the gate voltage applied to the blue gate, V_e, as seen in Figure.3.15. In this situation, electron transport occurs in the lower channel defined by the center and lower-blue gates. A color change indicates a change to the microwave power of the RF generator from 6 to 11 dBm (green to red). When the

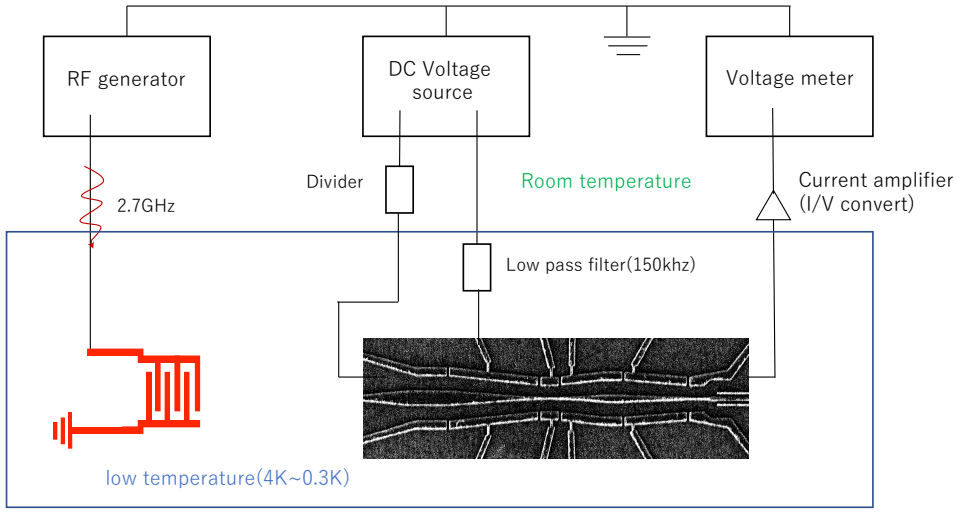

Figure 3.16: Connection between the sample and measurement equipment. Measured device is put in the cryostat to cool down to 0.3 K.

higher power of a SAW is input, a current plateau appears. This indicates that an integer number of electrons trapped in each SAW potential minimum is transported. The current value is displayed as a unit of ef/40 $\approx$ 10.8 pA. The number 40 is the duty cycle of the pulse-burst operation needed to suppress heating via the high-power SAW. Usually, the heating effect is not negligible above -10 dBm power in the continuous wave application. In the coherent beam-splitting experiment, the electron number transported in at SAW potential minimum is adjusted to one. Before describing the experiment of coherent beam splitting, more detail experiment on the quantization of current is explained next.

Figure.3.18(a) shows the differential current by the gate voltage, $\frac{dI}{dV_c}$, as a function of the power and gate voltage. The white area denotes the region in which the current changes abruptly. The black area appearing between the white lines indicates the current plateaus. The vertical white line indicates the formation of the current plateau. However, a slanting white line also appears, whose origin is not yet understood. This slanted structure often appears, although there is no explicit structure that might deform the current pattern in the device. This line might be related to the potential roughness of the channel, such as an impurity potential. However, other origins might exist, because the SAW-current formation process is not well studied. A good calculation of the formation of quantized current must include the time evolution of many electrons. To my knowledge, theories always have treated this phenomenon with a strong assumption, such as a very small number of electrons being trapped in their initial states [61], a classical treatment [63], or a semi-classical treatment [62, 81]

Figure.3.18(b) shows the differential current similar to Figure.3.18(a), but with the gate voltage and frequency of the microwave. The pulse width of the SAW is 50 μs. Note that the plateau

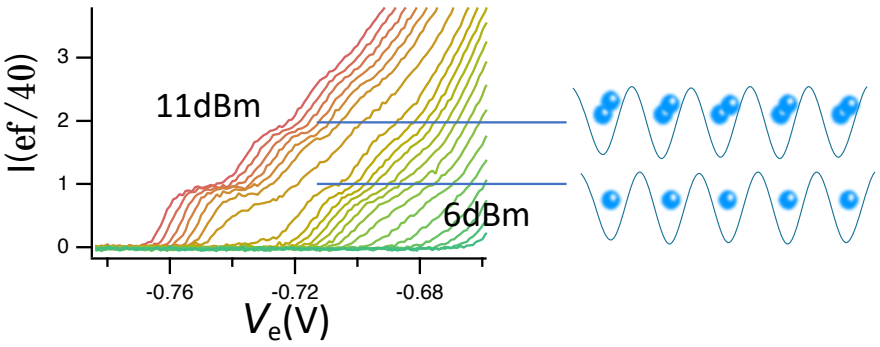

Figure 3.17: SAW-driven current in a unit of ef-times duty cycle. Power of SAW is changed from 6 (green) to 11 dBm (red).

structures appearing at the frequency differing from that of the large SAW-driven current is observed at a more positive V_e. The current is not shown, but the current is large at the white region in the figure. The large SAW-driven current appears around 2,668 and 2,670 MHz. However, the current plateau appears around 2,669–2,669.5 MHz. This observation is not yet understood, but, technically, it will be important to find a better condition to generate the quantized current.

Figure.3.19(a) shows the SAW-driven current as a function of the frequency of the SAW with the pulse width for the duty cycle as a parameter. The pulse width is controlled from 0.1 to 2 μs, keeping the duty cycle to 40 by simultaneously modifying the pulse period from 4 to 80 μs. When the pulse width is smaller than 0.5 μs, the current appears only around 2,729 MHz. Note that the sample used for the measurement in Figure.3.19 is different from the sample used for Figure.3.18. However, by increasing the pulse width to exceed 0.5 μs, another structure appears. Usually structural modifications emerge from the interference of the SAW. In a preceding study, M.R. Astley et al. argued that this as caused by the interference of the reflected SAW [72]. In my data, the frequency difference of the peaks is roughly 2 MHz. This corresponds to a 0.5-μs difference. Therefore, it is the interference of SAWs emitted in the same pulse burst. The length scale of 0.5 μs is about 1.3 mm converted by the velocity of the SAW. However, there is no probable structure that can reflect the SAW. The origin is therefore not yet understood. However, it is still important to recognize that the transportation of electrons suffers from unintended effects if a long-pulse SAW is used. Unfortunately, the unintended effect is difficult to remove by using a short pulse width, because the IDT has a rise time of 0.1 μs because of the 100 IDT fingers. The quality of data is worse at the ratio between the rise time and the pulse width. The many fingers are needed to apply a SAW of large amplitude.

Figure.3.19(b) and (c) show the derivative of the current by the gate voltage as a function of the pulse width and the gate voltage. Figure.3.19(b) (Figure.3.19(c)) show 2,728.6 MHz (2,729 MHz), where interference enhances (suppresses) the current. When the pulse width is increased, a jump in the plateau position is observed in Figure.3.19(c). The jump appears near the 1-μs pulse width. It is of the same order as the interference time scale mentioned above. These two data reinforce the idea

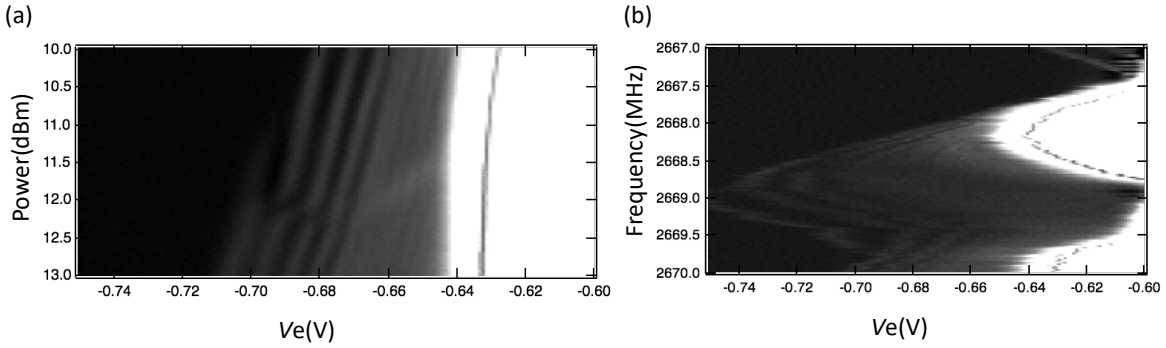

Figure 3.18: Characteristics of $\frac{dI}{dV_e}$ as a function of V_e, power, and frequency of the RF applied to the IDT .

that some unintended reflected SAW exists in the sample. The current plateau structure, however, does not change for pulse widths longer than 2 μs, where the interference effect is saturated. Even if a reflection SAW exist, the electron transport by the SAW and the current plateau remains stable.

3.3.3 Current oscillation in a tunnel-coupled wire

Figure.3.20 shows a magnified SEM image around the left tunnel-coupled wire in Figure.3.15. The terminology of the gate indices are the same as those shown in Figure.3.5. Single electrons are injected from the left into the lower channel and transported to the right direction by the SAW. Important gates for describing the tunnel oscillation are V_c, V_{sg1}, and V_{sg2}. These gates control the tunneling and detuning energies. V_{sf} is used to form a 1D channel connected to the tunnel-coupled region. V_{sb} is used to form a channel to the output contact.

In the experiment, V_{sg1} and V_{sg2} are used as variables. Here, two sweep directions are defined following the argument presented in the previous section. $V_{gd} = V_{gs1} - V_{gs2}$ and $V_{gs} = \frac{V_{gs1}+V_{gs2}}{2}$. V_{gd} are used to tune the detuning energy between the channels, and V_{gs} is used to tune the tunneling energy. The other gate voltages are fixed. One might think that V_c is useful for direct control of the tunneling energy and to keep the detuning. However, changes of V_c alter the entire potential structure of the sample. Therefore, V_c is fixed in most of the measurements. The right tunnel-coupled region has a slightly different geometry than does the left one. There is no explicit difference in the role of gate electrodes, but the gate correspond to V_{sb} does not exist in the right tunnel-coupled wire. In the following, although there are two tunnel coupling regions in the device, only one is adjusted to have an appropriate tunnel coupling. The other gate voltages are tuned such that the upper and lower channels are isolated in the rest of the device.

Figure.3.21 left (right) shows the output current of the upper (lower) channel for the SAW-driven electrons traveling through the right tunnel-coupled region. The current is shown as a function of V_{gd} with V_{gs} as a parameter from -1.3 to -1.5 V. For the more negative V_{gd}, the electrical potential in the upper channel is higher. Therefore, most electrons eject to the lower channel, and I_2 becomes

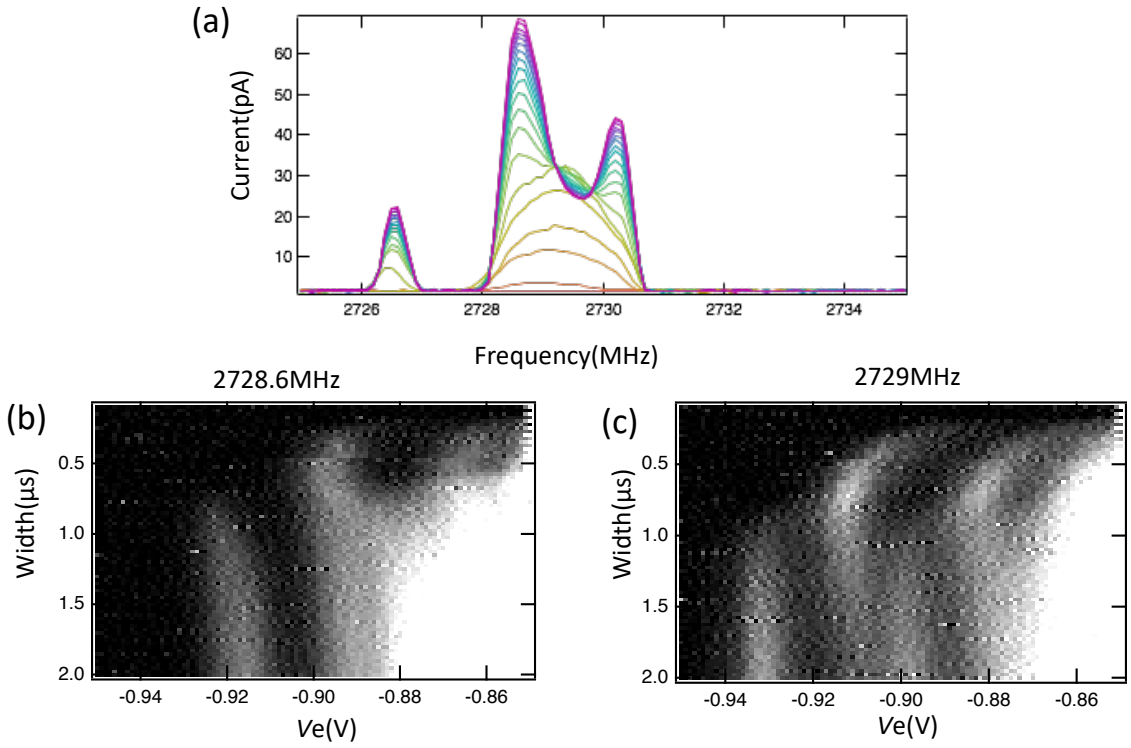

Figure 3.19: (a) Current induced by the SAW as a parameter of pulse width of the duty cycle from 0.1 μs (red) to 2 μs (purple). An interference signal appears having a longer pulse width than about 0.7 μs. (b)–(c) show the $\frac{dI}{dV_e}$ at frequencies of 2,728.6 and 2,729 MHz.

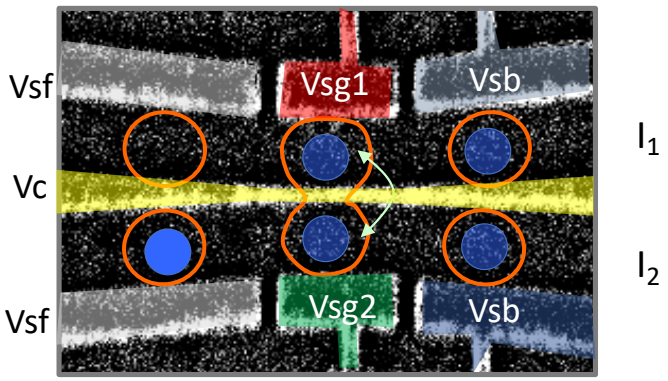

Figure 3.20: Expanded SEM image of the left tunnel-coupled region of Figure Figure.3.15

larger. By making V_{gd} more positive, I_1 (I_2) gradually increases (decreases). Finally, most electrons eject to the upper channel. The current is expressed with units of $\frac{ef}{40}$. Ideally, the total current I_{tot}= I_1+I_2 should be equal to $\frac{ef}{40}$. However, experimentally, it is about $\frac{0.8ef}{40}$. This is because quantization of the current is not perfect for a long 1D channel. A portion of electrons are scattered back to the entrance reservoir from the moving SAW potential minima. Although this current value is smaller than expected, the plateau structure remains. This indicates that the number of electrons trapped in each SAW potential minimum is less than one.

The rough current structure is similar to that observed in a preceding study [82] in which the direction of a classical SAW-driven current was controlled. However, a difference from the classical transport was also observed in these plots. A small ripple-like structure appeared around the slope of the current. To extract this signal structure, the analytically smoothed current was subtracted from the raw data, $\Delta I_2 = I_2 - \bar{I}_2$. $\bar{I}_2$ was an analytically smooth I_2 along the V_{gd} direction. Figure.3.22 shows the intensity plot of ΔI_2 after subtraction from the data shown in the right of Figure.3.21. The red region corresponds to the dips in Figure.3.21. Periodic appearances of peaks and dips are observed along the two directions. One is along the V_{gs}, and the other is along an inclined direction in the V_{gd} - V_{gs} plane. Although the oscillation amplitude and some fine structures are different, the current observed structure agrees well with the numerical calculation shown in Figure.3.10. Therefore, we can conclude that the ripple structure originates from the coherent tunneling of SAW-driven electrons.

To further confirm the scenario, the number of electrons at each SAW potential minimum is injected into the tunnel-coupled wire, controlled by tuning the entrance side gate in Figure.3.15. Figure.3.23(a) shows how the oscillation pattern changes as the total current increases. In this measurement, the left-side tunnel-coupling region is used, and electrons are injected from the upper channel. The color scale shows a normalized oscillation component defined as $\Delta I_1/I_{tot}$. Provided this oscillation component does not depend on the number of electrons in the potential minimum,

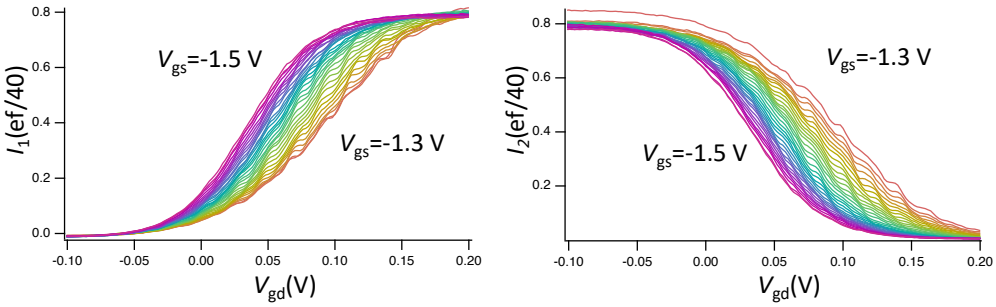

Figure 3.21: Left (right): raw data of the current traveling through the right tunnel-coupled region ejected to the upper (lower) output contact. The other nearby gate voltages are set to $V_c = -0.7$ V and $V_{sf} = -1.3$ V.

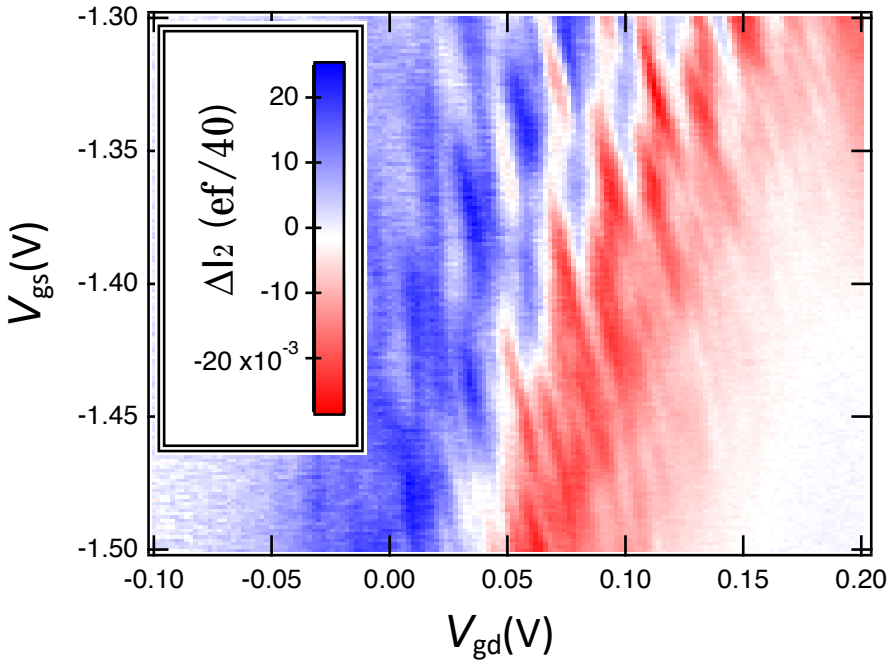

Figure 3.22: Oscillation component of the SAW-driven current obtained by subtracting the smoothed background current from the raw data of Figure.3.21 right.

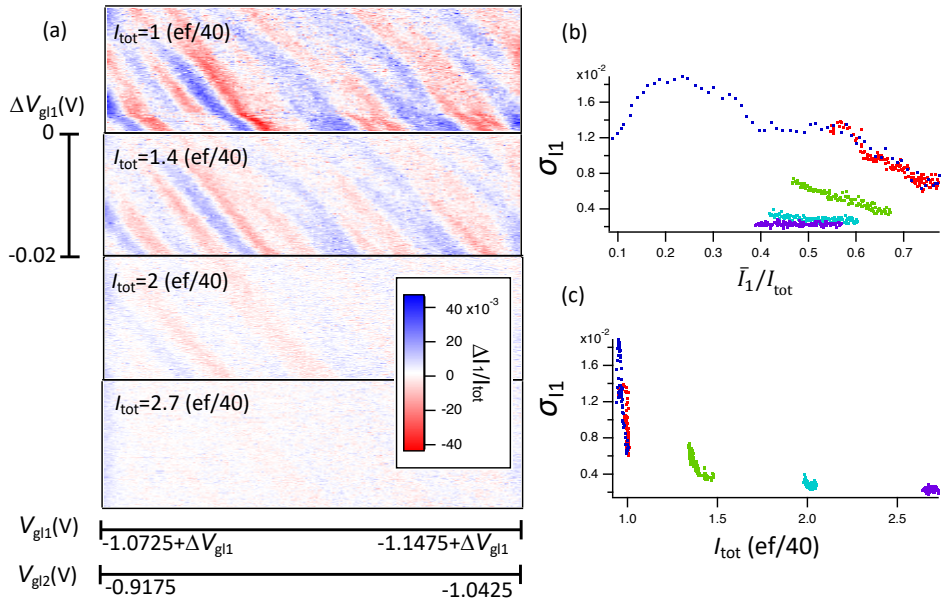

Figure 3.23: (a) Oscillation patterns for different numbers of injected electrons in each SAW potential minimum. The oscillation component divided by the total current is displayed. (b) and (c) Standard deviation of the oscillation component as a function of the normalized current, $\overline{I_1}/I_{tot}$, and total the current, I_{tot}, respectively. The datasets obtained for different I_{tot} are shown with different colors.

the oscillation pattern should be identical. However, the oscillation signal disappears with the increasing total current. This implies that the time evolution of electrons is completely different when more than one electron is trapped in the SAW potential.

In this experiment, the gate voltages are tuned such that the smoothed current ($\overline{I_i}$, i=1,2) is constant along the horizontal direction of Figure.3.23(a). Figure.3.23(b) and (c) show the standard deviation of the oscillation component (σ_{I1}), evaluated by calculating the root mean-square of $\Delta I_1/I_{tot}$ along the horizontal direction of Figure.3.23(a). The standard deviation is shown as a function of the normalized current, $\overline{I_1}/I_{tot}$ and I_{tot}, in Figure.3.23(b) and (c), respectively. The colors of the data points in these figures indicate I_{tot}. Red, green, cyan, and purple points belong to groups having I_{tot} of 1,1.4,2, and 2.7 ef/40, respectively, as shown in Figure.3.23(c). They are derived from the dataset shown in Figure.3.23(a). The blue points are derived from another dataset. In Figure.3.23(c), the deviation is large only when electrons are transported as singles. For example, for I_{tot} = 1.4 ef, 40% of the SAW potential minima trap two electrons, and 60% trap single electrons. σ_{I1} decreases as I_{tot} increases. In Figure.3.23(b), σ_{I1} shows a clear dependence on $\overline{I_1}/I_{tot}$. For the smaller $\overline{I_1}/I_{tot}$, the lower energy states in the upper channel plays a key role for tunneling oscillation. The peak of σ_{I1} at small $\overline{I_1}/I_{tot}$ appears because of the energy distribution of injected electrons.

As mentioned earlier, the amplitude of the oscillation component is smaller than that obtained from the numerical calculation. The amplitude of the normalized oscillation in the numerical calculation is close to one (see Figure.3.10). Thus, in the ideal case, the oscillation component of

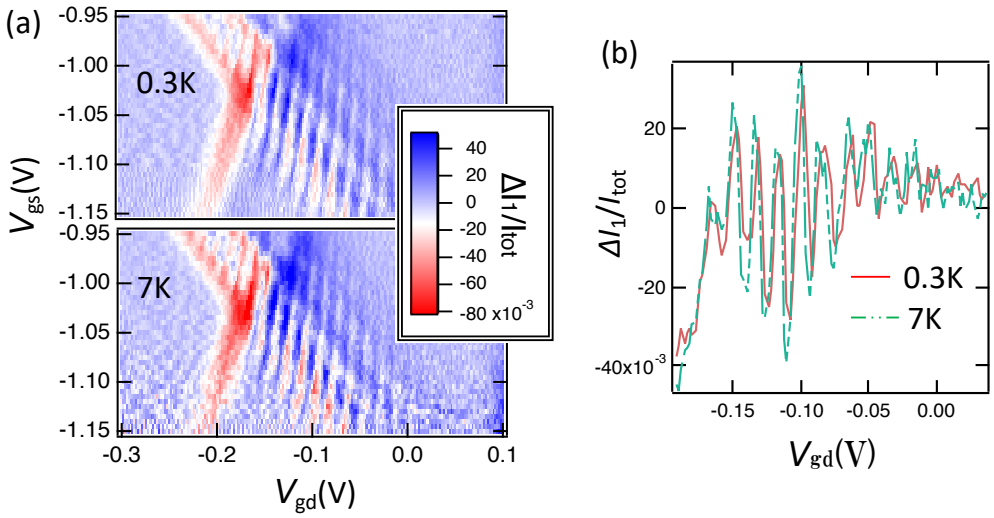

Figure 3.24: Temperature dependence of the tunnel oscillation. (a) $\Delta I_1/I_{\rm tot}$ measured at 0.3 and 7 K. The left tunnel-coupled region is used, and electrons are injected from the upper channel. (b) The cross section along $V_{\rm gs} = -1.08$ V. $V_{\rm c}$=-0.7 V, $V_{\rm sf}$=-1.2 V, and $V_{\rm sb}$=-1.3 V.

the current should be $0.4\frac{ef}{40}$ (half of the total current) in this experiment. However, it is about $0.02\frac{ef}{40}$ in Figure.3.21. The small amplitude is usually attributable to the low fidelity of the initialization, manipulation, or readout. Dephasing provides a common origin of low fidelity. The only dephasing source that possibly influences the system is the phonon. The other dephasing source (e.g., coupling to the reservoirs and gate electrodes) is negligible [83, 84]. The phonon-dephasing rate depends on temperature. However, experimental results presented in Figure.3.24, where the current oscillation components measured at 0.3 and 7 K are compared, shows that the current oscillation does not depend on temperature. Figure.3.24(a) shows a cross section at $V_{\rm gs} = -1.08$ V from Figure.3.24(b). An electron is injected from the upper channel in this experiment. The total current is slightly smaller at 7 K by 0.3 K. No visible difference in temperature is observed, which allows us to conclude that there is no influence from dephasing. The time duration of electron transporting through the tunnel-coupled wire is on the order of 100 ps. This value is close to the theoretical border where phonon dephasing becomes dominant for a static quantum dot [85]. Our experimental finding shows robustness of the SAW-driven electrons against dephasing, even at high temperatures. Then, we must ask, “ what is the origin of low oscillation visibility (ratio of the oscillating current to the total current)? ” The most likely answer is that the initial state is mixed with higher excited states. Excited states have different oscillation periods from those of the ground state. This reduces visibility and is an important problem to be solved for the future development of SAW-driven quantum electron optics.

In the numerical calculation section, I mentioned the possibility that the electron drops from the potential minimum and travels forward and that the oscillation pattern becomes clearer (see Figure.3.10). Figure.3.25 shows the current oscillation data having $V_{\rm sb}$ as a parameter. The left tunnel-coupled region is used for measurement, and single electrons are injected from the upper

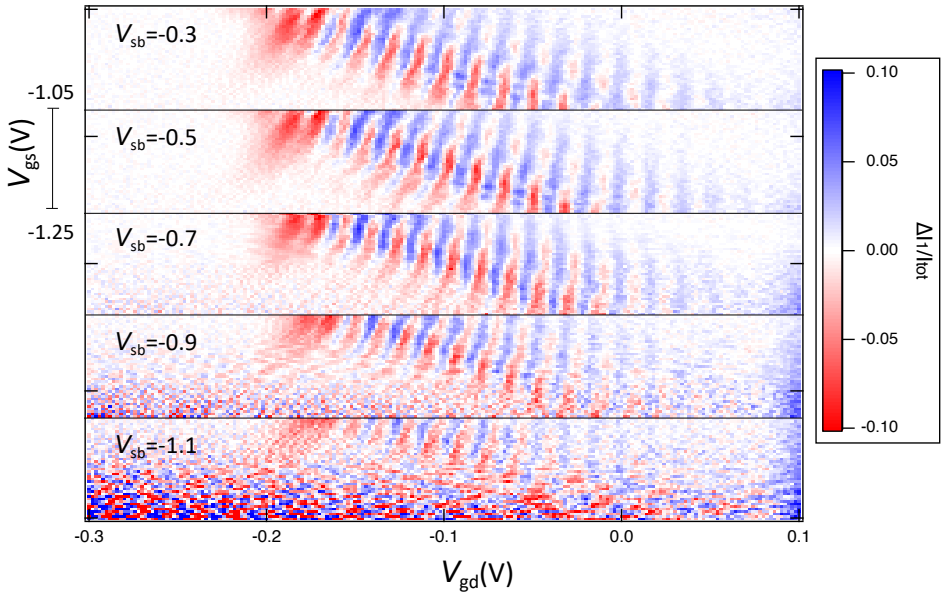

Figure 3.25: Current oscillation signal observed for the left tunnel-coupled region. V_{sb} is modified to control the potential at the exit of the coupled region.

channel. The color plot shows the normalized oscillation component. When the patterns of different V_{sb} are compared, we find that the visibility of the oscillation component depends on V_{sb}. For more positive V_{sb}, we see a clear signal of the coherent oscillation, but it becomes invisible for more negative V_{sb}. This observation is consistent with the numerical calculation shown in Figure.3.10, where a clearer oscillation pattern is observed when electrons drop from the SAW confinement.

In the experiment, the total current, I_{tot}, is not adjusted and decreases from ef/40 to 0.2 ef/40 at $V_{sb} = -0.3$ V and $V_{sb} = -1.1$ V, respectively. At V_{gs}.=-1.15 V. Note that I_{tot} also depends on V_{gs}. I_{tot} is 0.4 ef/40 at $V_{gs} = -1.05$ V and is zero at $V_{gs} = -1.25$ V for $V_{sb} = -1.1$ V. The reduction of the total current lowers the signal-to-noise ratio.

In conclusion, I have demonstrated a coherent beam splitter for SAW-driven electrons, which is desired for quantum electron optics. I performed both numerical and experimental demonstrations and observed the current oscillation pattern originating from the coherent tunneling oscillation. The amplitude of oscillation as not high enough to use for quantum electron optics in a single-electron unit, because the initial state at the entrance of the tunnel coupling region is probably not in the ground state. Nevertheless, this is the first demonstration of coherent beam splitting and is an important step toward realizing a solid-state flying qubit.

Chapter 4

Electron levels in a moving quantum dot

In the tunnel oscillation experiment of an electron trapped by the SAW potential, the oscillation visibility was not numerically as high as expected. This was probably caused by the randomness of the initial state of the injected electron, whose portion was in a higher energy state. This can happen from scattering because of the potential roughness in a depleted channel or the loading of electrons onto excited states at its entrance. Random-energy states cause smaller current oscillation amplitudes, because the time evolution process depends on the orbital state of the electron. In this chapter, I describe an experiment that aims to find the ratio of each energy state by measuring the tunnel current from the moving quantum dot to the electron reservoir. The tunneling probability depends on the energy of the injected electron. Thus, the information about the internal energy state can be extracted from the current pattern as a function of the gate voltage. In Section 4.1, the theoretical description of the experiment is provided. The theory semi-classically analyzes the probability of an electron escaping from a moving quantum dot. Then, the results of the experiment are presented in Section 4.2. The internal state of a moving quantum dot and its dependency on gate voltage are discussed. The results support the idea that a small portion of the initial state is in a ground state, but that controlling it is difficult.

4.1 Theoretical description

Transmittance of an electron from a quantum dot to a reservoir through a barrier potential depends on the energy level of the electron. Because the energy of the trapped electron is higher, it can more easily tunnel through the barrier potential. This property is used to detect internal electron levels in the moving quantum dot. For such an experiment, the same device used for the experiment in the previous chapter is used (see Figure.**??**). One channel is used for the transport of the SAW-driven electrons, and the other is used as a reservoir to detect the energy level of the electron. Figure.4.1 presents a schematic of this process. The left hollow in the potential indicates a moving quantum dot formed in either the upper or lower channel. The right side of Figure.4.1 indicates the reservoir. Through the center barrier activated by the gate voltage, V_c, the electron can escape to the reservoir, which is formed without applying any gate voltage for constructing a 1D channel. The proportion of electrons escaping to the reservoir is then measured as a current and a function of the gate voltage.

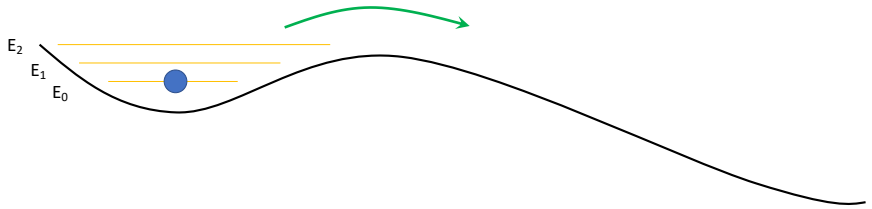

Figure 4.1: Electron-dropping experiment.

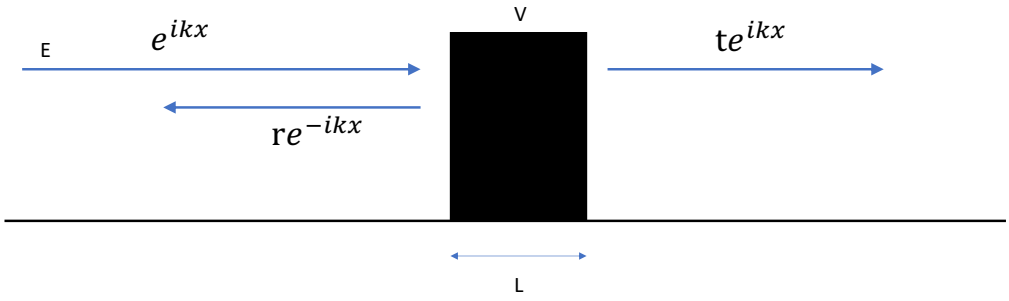

Figure 4.2: Tunnel effect through a rectangular potential.

Transmittance from the quantum dot to the reservoir for a given electrical potential should be argued theoretically. To my knowledge, however, there has been no strict method presented to date. M.R. Astley et al. [86] used the transmittance of a plane-wave electron instead of one confined to a quantum dot. Their electron was supposed to have collided with the potential barrier several times during propagation in the tunneling region via their method. The transmittance at each collision was evaluated by using the transmittance of the plane wave, and the entire transmittance was estimated by accounting for the number of collisions. They used this method to discuss electrons escaping from the dot when more than one electron was injected. Interactions between electrons are important in such a case. Our objective is, in contrast, to find the internal state of a single electron. Only the orbital state determines electron tunneling. In the following subsections, I discuss how the tunneling current should be described based on the idea of Astley et al. Our model allows us to find a fitting function to analyze our experimental data.

4.1.1 Transmittance through a tunnel barrier

First, the transmittance of an untrapped electron wave through the potential barrier is described. The assumed structure is a typical potential barrier formed to construct a quantum-point contact. However, instead of the potential, we start with a simple model of transmittance through a rectangular

potential, which is easily calculated using simple mathematics. The transmission coefficient, t, and the reflection coefficient, r, are given below, reflecting when the energy, E, of the injection electron is smaller than the barrier potential, V, as shown in Figure.4.2.

$$t = \frac{4ik\gamma e^{-ikL}}{(\gamma + ik)^2 e^{-\gamma d} - (\gamma - ik)^2 e^{\gamma L}} \tag{4.1}$$

$$r = \frac{(k^2 + \gamma^2)(e^{\gamma L} - e^{-\gamma L})}{(\gamma + ik)^2 e^{-\gamma d} - (\gamma - ik)^2 e^{\gamma L}} \tag{4.2}$$

$$\frac{\hbar^2 k^2}{2m} = E, \qquad \frac{\hbar^2 \gamma^2}{2m} = V - E. \tag{4.3}$$

Transmittance is then calculated as

$$T = |t|^2 = \frac{1}{1 + \frac{V^2}{4E(V-E)} \sinh(\sqrt{\frac{2m(V-E)}{\hbar^2}} L)}. \tag{4.4}$$

However, if the barrier potential becomes more complicated, the problem become more difficult. In the case where the electron energy is higher than any potential barrier, $\phi(x)$, the 1D Schrödinger equation can be solved by using a position-dependent wave number. By assuming $\psi(x) = A(x)e^{i\int k(x)dx}$ and $k(x) = \frac{\sqrt{2m(E-\phi(x))}}{\hbar}$, the equation becomes

$$(-\frac{\hbar^2}{2m}\frac{\partial^2}{\partial x^2} + \phi(x) - E)\psi(x) = (-\frac{\hbar^2}{2m}(\frac{\partial^2 A}{\partial x^2} + 2i\frac{\partial A}{\partial x}k + iA\frac{\partial k}{\partial x}))e^{i\int k dx} = 0. \tag{4.5}$$

If $\frac{\partial^2 A}{\partial x^2} \approx 0$, the answer becomes $A(x) = \frac{C}{\sqrt{k(x)}}$, where C is a constant. This treatment is the Wentzel–Kramers–Brillouin (WKB) approximation. The condition, $\frac{\partial^2 A}{\partial x^2} \approx 0$, is valid if $|E - \phi(x)| \gg 0$, and $\phi(x)$ is smooth. When $\phi(x)$ traverses E, a patching function is used for $|E - \phi(x)| \approx 0$, which is connected to the approximated function for $E > \phi$ and $E < \phi$. The typical assumption around $|E - \phi(x)| \approx 0$ is that the linear potential in space and the patching function become an Airy function. The matching condition between high and low potential regions is describe as follows:

$$\frac{1}{\sqrt{k}}\cos(-\frac{\pi}{4} + \int_x^a k dx) \leftrightarrow \frac{1}{2\sqrt{\kappa}} e^{-\int_a^x \kappa dx} \tag{4.6}$$

$$\frac{1}{\sqrt{k}}\cos(-\frac{\pi}{4} + \int_a^x k dx) \leftrightarrow \frac{1}{2\sqrt{\kappa}} e^{-\int_x^a \kappa dx}. \tag{4.7}$$

Here, $\kappa(x) = \frac{\sqrt{2m(\phi(x)-E)}}{\hbar}$ and a is in a position where $\phi(a) = E$. By using this matching condition, it becomes possible to calculate the transmission probability of the plane wave. Note that the matching condition is only strict when $\phi(x)$ is proportional to x around a. H. Fröman and P.O. Fröman derived the strict description of the transmittance for a general potential [87, 88].

Next, we calculate the transmittance through the potential barrier shown in Figure.4.3. First, we assume that the electron state in Regions I and Ⅲ in the figure is approximated as follows [89]:

$$\psi_I = \frac{A}{\sqrt{k}} e^{i\int k dx} + \frac{B}{\sqrt{k}} e^{-i\int k dx} \tag{4.8}$$

$$\psi_{III} = .\frac{C}{\sqrt{k}} e^{i\int k dx} + \frac{D}{\sqrt{k}} e^{-i\int k dx}. \tag{4.9}$$

Here, A, B, C, and D are constant. According to the Frömans, the relationship between the constants can be described as

$$\begin{pmatrix} C \\ D \end{pmatrix} = e^{\theta} \begin{pmatrix} (1+e^{-2\theta})^{\frac{1}{2}} & -i \\ i & (1+e^{-2\theta})^{\frac{1}{2}} \end{pmatrix} \begin{pmatrix} A \\ B \end{pmatrix}. \tag{4.10}$$

In the above equation, $\theta \equiv \int_a^b \kappa(x)dx$, and $E = \phi(x)$ at a and b. This supports a smooth potential problem. Generally, the transmittance is described as

$$T = \frac{Pe^{-2\theta}}{1 + Pe^{-2\theta}}, \tag{4.11}$$

where P is a parameter that is related to the potential structure. In the case of a smooth potential, $P = 1$. The electrical potential formed by gate voltages can be assumed to be a smooth potential. Thus, $P = 1$ in our problem. Note that above equation is also valid for $E > \phi(x)$ by expanding the real values, a and b, to satisfy $\kappa(a) = \kappa(b) = 0$ to the imaginary value. In the case of $E > \phi(x)$, $\theta < 0$, and transmittance is still smaller than 1. A finite reflection thus occurs, because the wave function cannot deform in a short-length scale.

The potential structure defined by a gate is often approximated as a quadratic potential. The potential structure of a quantum-point contact is approximated as

$$\phi(x, y) = V_0 - \frac{1}{2} m\omega_x^2 x^2 + \frac{1}{2} m\omega_y^2 y^2. \tag{4.12}$$

It is a good practice to consider the transmittance, because the potential barrier tuned by V_c has a similar potential barrier than that of a quantum-point contact. The transmittance is described as follows for different energy levels along the y direction:

$$T = \frac{1}{1 + e^{-\pi\epsilon_n}}, \tag{4.13}$$

with

$$\epsilon_n = \frac{2(E - \hbar\omega_y(n + \frac{1}{2}) - V_0)}{\hbar\omega_x}. \tag{4.14}$$

This equation sometimes appears for fitting an electron current through a potential barrier [86]. The general fitting function is described as

$$T = \frac{1}{1 + e^{\frac{-E-E_0}{\Delta}}}, \tag{4.15}$$

with Δ and E_0 as fitting parameters.

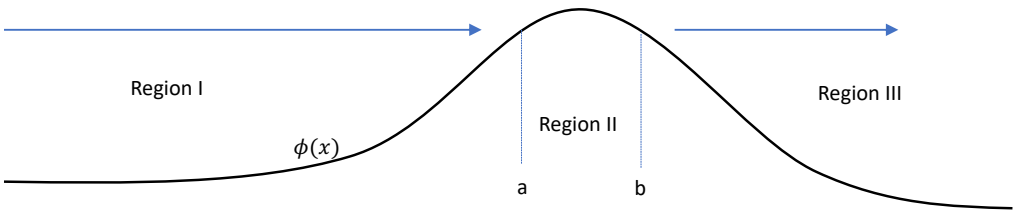

Figure 4.3: Electron transport through a barrier potential.

4.1.2 An electron in a moving quantum dot

The transmittance derived above is for free electrons. However, the transmittance that should be derived is one for confined electrons. Even so, to the best of my knowledge, there has been no theoretical derivation of transmittances for an explicit potential structure. The transmittance from the quantum dot to the reservoir, as a function of gate voltage, is necessary to analyze the experiment. Therefore, transmittance of the free electron is utilized for obtaining the probability of an electron escaping from the dot instead. Here, I discuss the validity of this treatment. I show that the localized state can be described as a superposition of free wave modes.

Consider the situation in which an electron is trapped in a 1D potential minimum, as shown in Figure.4.4. The wave function in Regions I and Ⅲ can be described as

$$\psi_I = \frac{A}{\sqrt{\kappa}} e^{-\int_x^a \kappa(x'dx')}, \tag{4.16}$$

because, at the limit of $x \to -\infty$, the wave function must be 0. Additionally,

$$\psi_{III} = \frac{C}{\sqrt{\kappa}} e^{-\int_b^x \kappa(x'dx')}. \tag{4.17}$$

A and C are constants. The wave function in Region Ⅱ is calculated using the matching condition in (4.6) and (4.7). With the matching condition between Regions I and Ⅱ, ψ_{II} must satisfy

$$\psi_{II} = \frac{2A}{\sqrt{k}} \cos\left(\int_a^x k(x')dx' - \frac{\pi}{4}\right) = \frac{2A}{\sqrt{k}} \left(e^{i\{\int_a^x k(x)dx - \frac{\pi}{4}\}} + e^{-i\{\int_a^x k(x)dx - \frac{\pi}{4}\}}\right). \tag{4.18}$$

This shows that the wave function is a superposition of the left and right moving free waves. The reflection of the left moving wave to the right moving wave shifts the phase by $-\frac{\pi}{2}$. Given the matching condition between Regions Ⅱ and Ⅲ, ψ_{II},

$$\psi_{II} = \frac{2C}{\sqrt{k}} \cos\left(\int_x^b k(x')dx' - \frac{\pi}{4}\right) = \frac{2C}{\sqrt{k}} \cos\left(-\int_a^b k(x')dx' + \int_a^x k(x')dx' + \frac{\pi}{4}\right). \tag{4.19}$$

Similarly, this shows that ψ_{II} is a superposition of left and right moving free waves. The reflection of the right moving wave shifts the phase by $-\frac{\pi}{2}$. Under the condition where (4.18) and (4.19) are

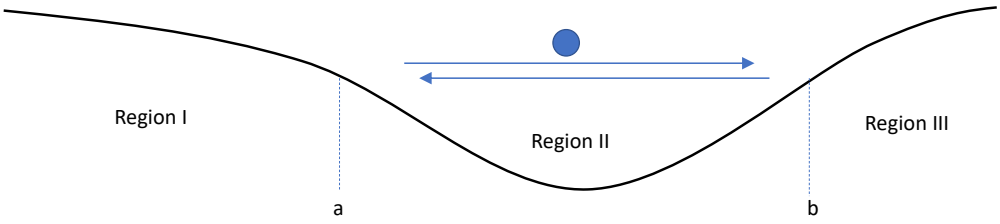

Figure 4.4: Potential structure forming a quantum dot.

identical functions, it thus becomes necessary to satisfy

$$\int_a^b k(x')dx' = (n + \frac{1}{2})\pi, \qquad A = (-1)^n C. \tag{4.20}$$

This equation restricts the energy of the free moving wave to a specific value. Note that the total phase shift during one oscillation of the free wave in the quantum dot is $\int_a^b k(x)dx + \int_b^a -k(x)dx - \pi = 2\pi n$. The first and second terms are the right and left traveling phases, respectively. The third term is the phase shift caused by the reflection.

To show that the condition (4.20) is consistent with the direct solution of the Schrödinger equation, the eigenenergy in a harmonic oscillator is derived. If the potential of the oscillator is $\frac{m\omega^2 x^2}{2}$, then the eigenenergy can be derived as follows by using $k(x) = \frac{\sqrt{2m(E - \frac{m\omega^2 x^2}{2})}}{\hbar}$:

$$\int_a^b k(x')dx' = \frac{\pi E}{\omega} = \pi(n + \frac{1}{2}) \qquad \therefore E = (n + \frac{1}{2})\hbar\omega. \tag{4.21}$$

The semi-classical treatment gives the correct eigenenergy. This result supports the validity of the semi-classical treatment.

It is possible to suppose that a free electron oscillates in a quantum dot as seen above. Therefore, we need to know the number of collisions to the barrier during the transportation of the electron by the SAW. A quantum dot is often described by a quadratic potential structure, $\frac{m\omega^2 x^2}{2}$. The time length for one oscillation, T, in the potential using the group velocity gives

$$T = \frac{2m}{\hbar}\int_a^b \frac{1}{k(x)}dx = \frac{2\pi}{\omega}. \tag{4.22}$$

Note that the above derivation of T is semi-classical, because group velocity cannot be defined when allowed wave vectors are discretized. The quantum-mechanical T can differ from $\frac{2\pi}{\omega}$. For example, in the case of the electron state, the quantum dot is a superposition of the ground and the third excited state. Thus, the time length for one electron oscillation in the quantum dot is $\frac{2\pi}{3\omega}$, because the phase of the ground state and the third excited state agree at this frequency. Therefore, hypothesizing, I use the semi-classically derived frequency as the oscillation frequency of the electron in a quantum dot.

Potential	Energy splitting	Frequency
$\frac{1}{2}m\omega^2x^2$	$(n+\frac{1}{2})\hbar\omega$	$\frac{\omega}{2\pi}$
$\infty(\theta(x-\frac{L}{2})+\theta(-x-\frac{L}{2}))$	$\frac{\hbar^2n^2\pi^2}{2mL^2}$	$\frac{\hbar n\pi}{2mL^2}$.

Table 4.1: Eigenenergies and semi-classical oscillation frequency for fundamental potential.

In the above discussion, the potential structure of a quantum dot is assumed to be harmonic. Note that the quadratic potential is not the only important term. An extreme case involves an infinite quantum-well potential. In this case, the oscillation frequency can be different at each eigenenergy state via the semi-classical derivation. Table.4.1 presents a reference of the eigenenergies and the oscillation frequencies estimated from the group velocity.

4.1.3 Fitting

The tunneling current from a quantum dot should be fitted with a fitting function to extract information from the current pattern. If the internal electron state of the quantum dot is not superposed between ground and excited states, the current is formed via the summation of the current from each energy-level electron. Therefore, the experimentally observed current of the tunneling into the reservoir as a function of gate voltage to tune the energy levels of the moving quantum dot will be schematically similar to that shown in Figure.4.5(a). Each step represents the contribution of each energy state. The height of a step indicates the occupation ratio of the corresponding state. To fit this current pattern, the fitting function will be

$$f(V)=\sum_n\sum_{k=0}^{\frac{\omega_n\tau}{2\pi}}a_nT_n(1-T_n)^k,\qquad T=\frac{1}{1+e^{\frac{V-V_n}{\Delta_n}}}. \tag{4.23}$$

Here, index n ($n=0,1,2,\cdots$) indicates the n-th energy level, and a_n is the ratio of the occupation in the n-th excited level. τ is the time length in which the electron remains in the tunneling region. This fitting function expresses the probability of an electron escaping the quantum dot after reflections at the potential barrier. The summation of k is limited by the maximum number of collision to the barrier during its travels through the tunneling region, $\frac{\omega_n\tau}{2\pi}$. The transmission of a one-time collision is expressed using the fitting function of (4.15). The variable in (4.15) changes from the energy to the gate voltage, assuming that the energy is proportional to the gate voltage. The fitting function described here is a direct consequence of the discussion presented in the previous subsections. Next, the fitting function is further simplified.

First, the summation by k is approximated. The typical orbital-energy spacing is hundreds of micro-electron volts, which is converted to hundreds of GHz. τ is several 100 ps in our setup. Thus, the number of collision to the barrier is in the several 10s. The following approximation reduces the number of terms:

$$f(V)\approx\sum_n\sum_{k=0}^{\infty}a_nT_n(1-T_n)^ke^{-\frac{2\pi k}{\omega_n\tau}}=\sum_n a_n\frac{T_n}{1-(1-T_n)e^{-\frac{2\pi}{\omega_n\tau}}}. \tag{4.24}$$

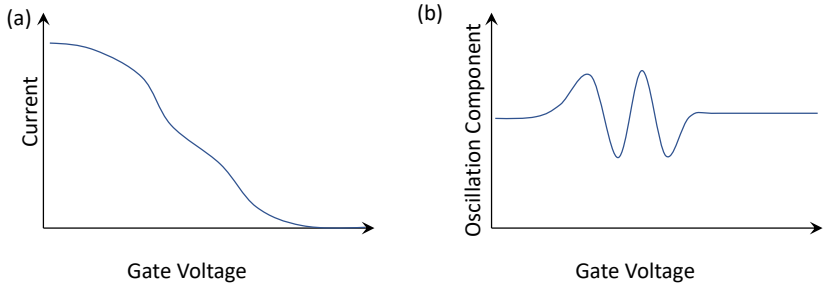

Figure 4.5: (a) Current pattern and (b) Smoothed background subtracted current.

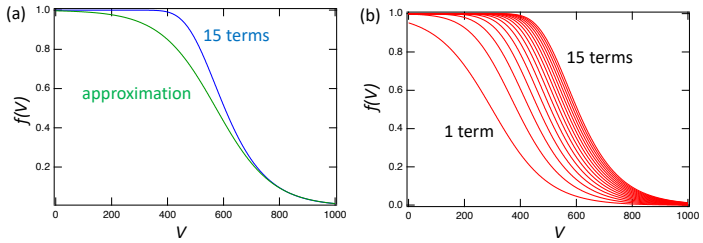

Figure 4.6: (a) Comparison of (4.23) with $\frac{\omega_n \tau}{2\pi} = 14$ and (4.24). $\Delta_0 = 100$, a_0=1 and $a_i = 0$ for i>0. V_0'=300 (see (4.26)). (b) Comparison of (4.23) from $\frac{\omega_n \tau}{2\pi}$=0–14.

Figure.4.6(a) compares two functions, $f(V)$, calculated with (4.23) and (4.24). The small $f(V)$ part is well-approximated with Figure.4.24, although the discrepancy becomes bigger at larger $f(V)$ parts. Figure.4.6(b) shows (4.23), depending on the number of terms (i.e., $\frac{\omega_n \tau}{2\pi}$).

Another issue of this fitting function is that it involves many fitting parameters. It uses four parameters (i.e., Δ_n, ω_n, a_n, and V_n) for each energy level. The number of fitting parameters should be minimized for performing physically meaningful fitting. Hereafter, the potential shape of the barrier is assumed to be the one expressed by (4.12). The potential of the quantum dot is also assumed to be a harmonic potential. The confinement potential of the quantum dot is assumed to be independent of the position in both transverse x and longitudinal y directions. In Equation (4.14), $E = \hbar\omega_x'(n + \frac{1}{2}) + \hbar\omega_y'(n + \frac{1}{2})$ for the harmonic potential quantum dot. Under the additional assumption that $\omega_y = \omega_y'$, the transmittance in (4.13) is described by substituting a parameter in (4.14) with $\epsilon_n = \frac{2(\hbar\omega_x'(n+\frac{1}{2})-V_0)}{\hbar\omega_x}$. The confinement along y is caused by the SAW potential in the experiment. Thus, the assumption is justified if the modulation of the SAW confinement along the x direction is negligible. The fitting parameters in (4.24) are thus restricted under these assumptions.

$$\omega_n = \omega, \quad \Delta_n = \Delta, \quad V_{n+1} - V_n = dV. \tag{4.25}$$

Using this relation, the fitting function can be further simplified.

$$f(V) \approx \sum_n \frac{a_n}{1 + e^{\frac{V-V_0-(n-1)dV}{\Delta}}(1 - e^{-\frac{2\pi}{\omega\tau}})} = \sum_n \frac{a_n}{1 + e^{\frac{V-V_0'-(n-1)dV}{\Delta}}}. \tag{4.26}$$

Here, $e^{-\frac{V_0'}{\Delta}} = e^{-\frac{V_0}{\Delta}}(1 - e^{-\frac{2\pi}{\omega\tau}})$.

For the analysis of experimental data, the smoothed background subtracted current is often used to extract the oscillation component of the previous chapter. In this case, the derived data become as shown in Figure.4.5(b). The fitting function for the smoothed background subtracted current then becomes

$$F(V) = \sum_n \left(\frac{a_n}{1 + e^{\frac{V-V_0'-(n-1)dV}{\Delta}}} - \frac{1}{2w} \int_{V-w}^{V+w} dV' \frac{a_n}{1 + e^{\frac{V'-V_0'-(n-1)dV}{\Delta}}} \right) \tag{4.27}$$

$$= \sum_n \left(\frac{a_n}{1 + e^{\frac{V-V_0'-(n-1)dV}{\Delta}}} + \frac{a_n\Delta}{2w} \ln \frac{1 + e^{-\frac{V-V_0'-(n-1)dV+w}{\Delta}}}{1 + e^{-\frac{V-V_0'-(n-1)dV-w}{\Delta}}} \right). \tag{4.28}$$

w denotes the range of smoothing. Note that result of fitting with (4.26) and (4.28) do not coincide, because the fitting functions evaluate experimental results differently, although the difference of the obtained fitting parameter is not big.

4.2 Experimental result

五年以内に出版予定

4.3 Discussion

In the discussion above, we assumed that the electron state was not coherent. Because the electron states injected into the tunneling region are random, the phase information of each is averaged out. This assumption is reasonable, because we had only small visibility into the coherent tunnel oscillation in the previous chapter. However, the coherence of electrons in the tunneling region can also lead to the formation of a current structure for the dropping electron. Here, I present a numerical calculation of the time evolution of a SAW-driven electron in the tunneling region.

The Hamiltonian model for describing the system is

$$H = \sum_i \epsilon_i a_i^\dagger a_i + \sum_k \omega_k b_k^\dagger b_k + \sum_{i,k} (c_{i,k} a_i^\dagger b_k + h.c.). \tag{4.29}$$

$a_i^\dagger(a_i)$ is the creation (annihilation) operator for a SAW-driven electron at the i-th eigenstate. $b_k^\dagger(b_k)$ is the creation (annihilation) operator of the electron in the reservoir having a wave number of k. ϵ, ω, and c are energies of the electrons in the quantum dot, the reservoir, and the coupling

coefficient, respectively. In the experiment, the electron transported to a tunneling structure suddenly experienced tunnel coupling to the reservoir. Thus, the time evolution could be calculated using a time-independent Hamiltonian as follows:

$$\rho(t) = e^{-i\frac{Ht}{\hbar}}\rho(t=0)e^{i\frac{Ht}{\hbar}}. \tag{4.30}$$

Only the electrons trapped in the SAW-driven moving quantum dot contribute to the current, and those in the reservoir do not affect it. Therefore, it is safe to assume that the number of electrons in the reservoir is zero. Therefore, it becomes possible to assume that the initial state can be described by the separate states of the quantum dot and the reservoir. The density matrix at the initial time (t=0) is described as $\rho(t=0) = \rho_a(t=0) \otimes \rho_b(t=0)$. Here, subscripts a and b indicate the quantum dot and the reservoir, respectively, and $\rho_b(t=0) = |0\rangle\langle 0|$. Here, $|0\rangle$ indicates a vacuum.

Precise calculation can be conducted using the above equation. However, the number of states included in the calculation is infinite, and the coefficient is unknown. Therefore, for simplicity, we consider the Hamiltonian having a decreased number of states:

$$H/\hbar = \sum_{i=1,2}(-1)^i a_i^\dagger a_i + \sum_{k=0}^{100}(0.04 * k - 2)b_k^\dagger b_k + \sum_{i,k}(0.01 a_i^\dagger b + h.c.). \tag{4.31}$$

This assumes that only two states exist in the moving quantum dot. The electron state in the reservoir is no longer continuous, but there is a finite number of states having energies close to that of the quantum-dot electron. The coupling constant between each state is identical. The results of time evolution are displayed in Figure.4.7(a), which shows the probability of the electron staying in the moving quantum dot after traveling through the tunneling region. The initial electron state is assumed to be $\rho_a = \frac{1}{2}(|1\rangle\langle 1| + |2\rangle\langle 1| + |1\rangle\langle 2| + |2\rangle\langle 2|)$ in red, $\rho_a = \frac{1}{2}(|1\rangle\langle 1| + i\,|2\rangle\langle 1| - i\,|1\rangle\langle 2| + |2\rangle\langle 2|)$ in green, and $\rho_a = \frac{1}{2}(|1\rangle\langle 1| + |2\rangle\langle 2|)$ in blue. Here, $|1\rangle$ ($|2\rangle$) denotes that the state in which the electron is in the ground (excited) state. In the first two states, the electron is in a fully coherent state, whereas, in the last state, no phase information is kept. When the electron is coherent, its time evolution trapped in the quantum dot shows oscillation behavior at the frequency of the energy spacing of the quantum dot. The origin of this oscillation is the interference within the moving quantum dot, wherein the electron acquires different phases between the ground and excited states. This leads to the oscillation of the electron within the dot, periodically changing the distance from the reservoir [90].

The question is whether or not this oscillation can be the origin of the current structure observed in this experiment. In the experiment, the controllable valuable is the side-gate voltage, not the time-length/duration of the time evolution. However, by tuning the negative voltage applied to the side gate, the frequency of the coherent motion increases, because confinement of the quantum dot become stronger, and the time duration in the tunneling region becomes effectively longer.

The calculation data in Figure.4.7(a) are not fully appropriate for considering the origin of the oscillation in the electron tunneling. A small correction is added to the Hamiltonian for the result shown in Figure.4.7(b), assuming a higher coupling constant between excited states and the reservoir than between the ground state and the reservoir. This correction is necessary to reproduce a realistic situation wherein the tunnel barrier height is finite. When the number of oscillations increases, the

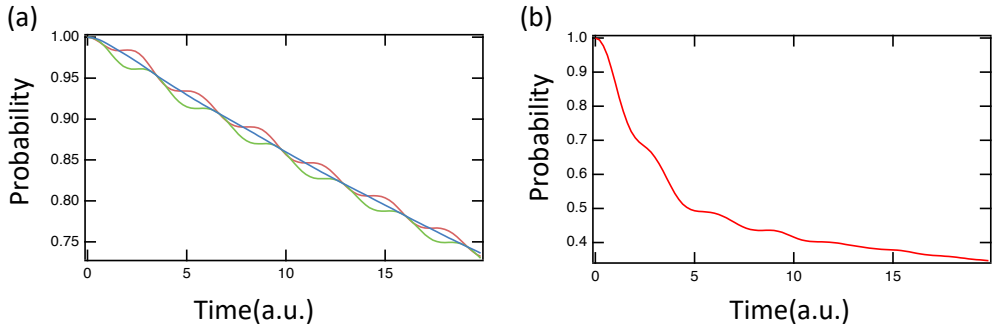

Figure 4.7: Probability of an electron in a quantum dot at the tunneling region. (a) The initial states are $|1\rangle + |2\rangle$ and $|1\rangle + i\,|2\rangle$, with mixed states of $|1\rangle$ and $|2\rangle$. These are indicated by red, green, and blue lines, respectively. (b) The coupling constant for $|1\rangle$ ($|2\rangle$) is 0.01 (0.05). The initial state is $|1\rangle + |2\rangle$.

oscillation component decreases. This is because an excited state component quickly escapes from the quantum dot. When this behavior is compared with the experiment, the dependence on the gate voltage is completely reversed. The oscillation component increases by applying more negative gate voltage in the experiment, but this decreases in the numerical calculation. Therefore, we conclude that the observed behavior is not caused by the coherent motion of electrons, but it is instead caused by the energy-dependent tunneling.

I also calculated the time evolution by solving the quantum master equation under the Born–Markov approximation. It uses the Hamiltonian of

$$H/\hbar = \sum_{i=1,2} (-1)^i a_i^\dagger a_i + \sum_k \omega_k b_k^\dagger b_k + \sum_{i,k} (0.1 a_i^\dagger b + h.c.). \tag{4.32}$$

Details are described in the appendix. The equation of time evolution of the density matrix is given by

$$\frac{d\rho_s}{dt} = -i[\sum_{i=1,2} (-1)^i a_i^\dagger a_i, \rho_s(t)] - 0.01 \times \pi c \left\{ \begin{pmatrix} 1 & 1 \\ 1 & 1 \end{pmatrix} \rho_s(t) + \rho_s(t) \begin{pmatrix} 1 & 1 \\ 1 & 1 \end{pmatrix} \right\}. \tag{4.33}$$

Here, 0.01 comes from the second power of the coupling constant, 0.1, and [,] indicates a commutator. The density matrix is expressed based on $|1\rangle$ and $|2\rangle$. c indicates the density of states in the reservoir at the energy of the electron in the quantum dot. The result of the time evolution from Equation (4.33) is shown in Figure.4.8, illustrating the probability of the electron remaining in the quantum dot. The initial state is $\rho_a = \frac{1}{2}(|1\rangle\langle 1| + |2\rangle\langle 1| + |1\rangle\langle 2| + |2\rangle\langle 2|)$. The oscillating pattern is almost the same as the one shown in Figure.4.7 except for the change of the absolute value of the probability, which is caused by the different number of reservoir states.

The calculation relying on the quantum master equation supports the result of the direct time evolution calculation (4.30) with a limited number of bases (4.31). The calculation shows that the experimental result is not assigned to the coherent motion within the channel. However, it instead

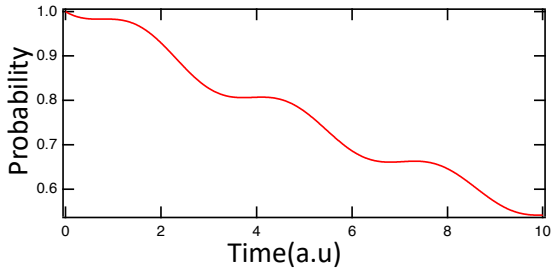

Figure 4.8: Probability of an electron in a quantum dot at the tunneling region when the initial state is $|1\rangle + |2\rangle$. This is calculated using the quantum master equation under the Born–Markov approximation.

originates from the energy-dependent tunneling probabilities. The occupation of a higher energy state is consistent with the experimental results described in the previous chapter.

Chapter 5

High-visibility tunneling oscillation

As discussed in previous chapters, the visibility of the tunneling oscillation of the beam splitter is small, because the initial orbital state is not well-determined. To overcome this difficulty, a new approach for initializing the electron state is necessary. In this chapter, I present the occasionally observed high-visible current oscillation. Although a similar device structure is used, the current pattern (i.e., observed current as a function of gate voltages) through the tunnel-coupled wire is largely different. The origin of this current pattern is still not clear. However, it is known to not originate from the tunneling oscillation of an electron trapped in the SAW potential, similar to the oscillation discussed in Chapter 3. As a possible scenario for explaining the high-visibility oscillation pattern, a hot electron model is presented near the end of this chapter.

5.1 Experimental result

五年以内に出版予定

5.2 Discussion

五年以内に出版予定

Chapter 6

Two-electron pair-splitter for violating Bell's inequality

An electron has two quantum degrees of freedoms. One is defined by its orbital state, and the other is defined by its spin. Experiments in previous chapters aimed at controlling the orbital state while the spin state was not considered, because the spin states are degenerated and do not affect the transport. The orbital state of a SAW-driven electron is used to define the flying qubit of an electron. However, it is generally believed that spin is more promising for quantum information processing. This is because the spin information is more robust against the dephasing induced by coupling to the environment. The main decoherence sources for the spin state of an electron confined in a quantum dot include hyperfine and spin-orbit interactions. However, the decoherence time takes much longer than that of the orbital state, which suffers from the electron–phonon coupling and direct-charge noise. SAW-driven electrons can also carry spin information. An earlier study demonstrated that the loss of spin information was negligible for 4-μm transport of SAW-driven electrons [41]. Spin manipulation during transport has also been demonstrated [42]. The study of spin information of SAW-driven electrons is a research target of this thesis.

One of the benchmarks for quantum information processing is the ability to generate entanglement. In a SAW-driven electron system, several methods to generate and detect entanglement states of orbital and spin states have been proposed [23, 91, 92]. The orbital entanglement state remains out of reach presently, because the precise control of the electron orbital state has not yet been realized, as explained in Chapters 3 and 4. The generation of the spin entanglement state was investigated by using two distant static quantum dots [41] by transferring one of the two electrons in one of the dots to the other via a SAW pulse. However, the spin state was flipped before or after the transfer because of the irradiation of the SAW pulse onto the static quantum dot. In this chapter, I propose a novel scheme for generating and detecting the entanglement between distant spins using SAW-driven electrons. The goal of this proposal is to demonstrate the violation of Bell's inequality. In the upcoming chapter section, this proposal is described. Then, in the subsequent section, one of the important functions for realizing the proposed scheme (i.e., the electron-pair splitter) is demonstrated experimentally. The efficiency of the splitter reaches about 89%, which is enough to demonstrate a violation of Bell's inequality.

6.1 Future device to test the violation of Bell's inequality

五年以内に出版予定

6.2 Experimental result

五年以内に出版予定

Appendix A

Quantum master equation

The derivation of the quantum master equation is described here, following [107]. Starting from the general equation, I derive equation (4.33).

When we describe a system, it is usually coupled with the environment. The Hamiltonian is described as $H = H_s + H_e + H_i$, in which subscripts s, e, and i indicate system, environment, and interaction between them, respectively. Usually, it is assumed that the system and the environment are independent initially. Therefore, the density matrix is described as $\rho(t = 0) = \rho_s \otimes \rho_e^{eq}$. The superscript, eq, indicates equilibrium. The time evolution of the density matrix is described by the following relation:

$$(\partial_t - L)\rho = 0. \tag{A.1}$$

Here, L is the quantum Liouville operator defined as $L \equiv -i[H, \ ]$. For convenience, the same subscript as the Hamiltonian is used to describe the operation, such as $L_s = -i[H_s, \ ]$. Then, the mapping operator is defined as

$$P \equiv \rho_e^{eq}\mathrm{Tr}_e. \tag{A.2}$$

Here, the trace is taken only for the environment. From the definition, $\mathrm{Tr}_e(\rho_e^{eq} H_i) = 0$ is satisfied. Therefore, the following equation is satisfied.

$$PL_b = L_b P = 0, \quad [L_s, P] = 0, \quad PL_i P = 0 \tag{A.3}$$

By using the mapping operator to complement the space of P, $Q = I - P$, and new notation of $\rho_P \equiv P\rho$ and $\rho_Q \equiv Q\rho$, the equation of motion is separated to two terms:

$$\partial_t \rho_P = L_s \rho_P + PL_i \rho_Q \tag{A.4}$$

$$, \partial_t \rho_Q = QL\rho_Q + QL_i \rho_P. \tag{A.5}$$

The rigid answer to the second equation is

$$\rho_Q(t) = \int_0^t dt' e^{t' QLQ} L_i \rho_P(t - t'). \tag{A.6}$$

This is confirmed by

$$\begin{aligned}\partial_t \rho_Q &= e^{tQLQ} L_i \rho_P(0) - \int_0^t dt' e^{t'QLQ} L_i \partial_{t'} \rho_P(t-t') \\ &= e^{tQLQ} L_i \rho_P(0) - e^{t'QLQ} L_i \rho(t-t') \mid_{t'=0}^{t'=t} + \int_0^t dt' QLQ e^{t'QLQ} L_i \partial_{t'} \rho_P(t-t') \\ &= L_i \rho_P + QLQ\rho_Q = QL_i\rho_P + QL\rho_Q.\end{aligned} \tag{A.7}$$

Then, the first equation comes to

$$\rho_P = L_s \rho_P + \int_0^t dt' P L_i e^{t'QLQ} L_i \rho_P(t-t'). \tag{A.8}$$

The density matrix of the system side ($\rho_s = \mathrm{Tr}_e \rho$) then follows the equation described as

$$\partial_t \rho_s(t) = L_s \rho_s(t) + \int_0^t dt' \mathrm{Tr}_e (L_i e^{t'QLQ} L_i \{\rho_s(t-t') \otimes \rho_e^{eq}\}). \tag{A.9}$$

This is known as the generalized master equation. It is rigid but difficult to calculate. One approximation is to assume a weak coupling. This is known as the Born approximation. In (A.9), it corresponds to substituting $L_0 = L_s + L_i$ instead of L into the exponential. Another approximation assumes that the future state is determined by only the present state and not by past state. This is known as the Markov approximation. In (A.9), it corresponds with the replacement of $\rho_s(t-t')$ with $\rho_s(t)$ and also $\int^t$ with $\int^\infty$. This approximation is justified when $e^{t'QLQ}$ decreases faster than the change of ρ_s. With these approximations, equation (A.9) is transformed through

$$\begin{aligned}\mathrm{Tr}_e (L_i e^{t'QL_0Q} L_i \{\rho_s(t) \otimes \rho_e^{eq}\}) &= \mathrm{Tr}_e (L_i e^{t'L_0} L_i \{\rho_s(t) \otimes \rho_e^{eq}\}) \\ &= \mathrm{Tr}_e (L_i e^{-\frac{iH_0t'}{\hbar}} L_i (\rho_s(t) \otimes \rho_e^{eq}) e^{\frac{iH_0t'}{\hbar}}).\end{aligned} \tag{A.10}$$

Here, the Liouville operator is applied to only $\rho_s(t) \otimes \rho_e^{eq}$ not to $e^{\frac{iHt'}{\hbar}}$. Finally, the quantum master equation under the Born–Markov approximation is described as

$$\partial_t \rho_s(t) = L_s \rho_s(t) + \int_0^\infty dt' \mathrm{Tr}_e (L_i e^{-\frac{iH_0t'}{\hbar}} L_i (\rho_s(t) \otimes \rho_e^{eq}) e^{\frac{iH_0t'}{\hbar}}). \tag{A.11}$$

Then, we derive (4.33) from the Hamiltonian (4.32). Source, environment and interaction terms are described as

$$\begin{aligned}H_s/\hbar = \sum_{i=1,2} (-1)^i a_i^\dagger a_i, \quad H_e/\hbar = \sum_k \omega_k b_k^\dagger b_k \\ H_i/\hbar = \sum_{i,k} (0.1 a_i^\dagger b_k + h.c.)\end{aligned} \tag{A.12}$$

The environment in the experimental setup is the vacuum, $\rho_e^{eq} = |0\rangle\langle 0|$. ρ_s has three bases for the Hamiltonian, H_s: $|0\rangle$, $a_1^\dagger |0\rangle$, and $a_2^\dagger |0\rangle$. By applying the useful relation,

$$e^{-\frac{iH_0t'}{\hbar}} a_j^\dagger e^{\frac{iH_0t'}{\hbar}} = e^{-i(-1)^j t} a_j^\dagger \quad \text{and} \quad e^{-\frac{iH_0t'}{\hbar}} b_k^\dagger e^{\frac{iH_0t'}{\hbar}} = e^{-i\omega_k t} b_k^\dagger, \tag{A.13}$$

the trace term in second term of the right-hand side of (A.11) can be described as

$$\begin{aligned}
&\mathrm{Tr}_e([H_i, e^{-\frac{iH_0t'}{\hbar}}[H_i, \rho_s(t)\otimes|0\rangle\langle 0|]e^{\frac{iH_0t'}{\hbar}}]) \\
&\quad = 0.1\{\mathrm{Tr}_e([H_i, e^{-\frac{iH_0t'}{\hbar}}(b^\dagger a\rho_s(t)\otimes|0\rangle\langle 0| - \rho_s(t)\otimes|0\rangle\langle 0|\, a^\dagger b)e^{\frac{iH_0t'}{\hbar}}])\} \\
&\quad = 0.01\sum\{e^{i\{(-1)^n-\omega_k\}t'}a_n^\dagger a_m\rho_s(t) - e^{-i\{(-1)^n-\omega_k\}t'}a_n\rho_s(t)a_m^\dagger \\
&\qquad\quad -e^{i\{(-1)^m-\omega_k\}t'}a_n\rho_s(t)a_m^\dagger + e^{-i\{(-1)^m-\omega_k\}t'}\rho_s(t)a_n^\dagger a_m\}
\end{aligned} \tag{A.14}$$

During the derivation, the cyclic property of the trace operation is utilized. When the integral of (A.11) is evaluated, the exponential term returns a delta function. For simplicity, it is possible to remove the base, $|0\rangle$, from the density matrix, because $|0\rangle$ does not influence $a_1^\dagger|0\rangle$ and $a_2^\dagger|0\rangle$, which is interesting. In this case, the $a\rho a^\dagger$ term is negligible, because the creation and annihilation operators change the state to one that is not accounted for in the density matrix. The matrix-form expression of $a_n^\dagger a_m$ is $\begin{pmatrix}1 & 1\\ 1 & 1\end{pmatrix}$. Finally, it arrives at Equation (4.33).

Aknowledgement

I would like to take this opportunity to thank all of the people who supported me throughout the course of my Ph.D studies.

The present work was performed under the supervision of Professor Seigo Tarucha at the department of Applied physics, University of Tokyo. First, I deeply thank Prof. Tarucha for giving me exciting experimental topics. His insight and attitude toward physics provided me with useful information.

I am really grateful to Dr. Michihisa Yamamoto, now the team leader at the Center for Emergent Matter Science, RIKEN. He is well-versed in this field, and discussions with him were truly helpful to the progression of my work. In addition, he kindly corrected my poor English in this thesis and other documents. I would like to thank him from the bottom of my heart.

I also thank Dr. Shintaro Takada and Dr. Jason Chen. They both kindly taught me the basic but important knowledge and techniques of my experimental research. Their wise advice contributed significantly to this thesis. I would also like to express my appreciation to the other members of the Tarucha Laboratory. Discussions with them stimulated me and helped to develop deep insight to the physics. Moreover, knowledge about related physical field obtained from them has been quite helpful in the design of future targets.

I would like to show gratitude to Prof. Chrisopher Bäuerle and his laboratory members for their fruitful discussion about these results. The experiment described in this thesis used a high-quality wafer offered from Prof. Andreas D. Wieck and Dr. Arne Ludwig. I am grateful to them.

Finally, I would also like to express my gratitude to my family for their moral support and warm encouragements.

Bibliography

[1] Ji-Gang Ren, Ping Xu, Hai-Lin Yong, Liang Zhang, Sheng-Kai Liao, Juan Yin, Wei-Yue Liu, Wen-Qi Cai, Meng Yang, Li Li, Kui-Xing Yang, Xuan Han, Yong-Qiang Yao, Ji Li, Hai-Yan Wu, Song Wan, Lei Liu, Ding-Quan Liu, Yao-Wu Kuang, Zhi-Ping He, Peng Shang, Cheng Guo, Ru-Hua Zheng, Kai Tian, Zhen-Cai Zhu, Nai-Le Liu, Chao-Yang Lu, Rong Shu, Yu-Ao Chen, Cheng-Zhi Peng, Jian-Yu Wang, and Jian-Wei Pan. Ground-to-satellite quantum teleportation. *Nature*, 549(7670):70–73, 2017.

[2] Sheng-Kai Liao, Wen-Qi Cai, Wei-Yue Liu, Liang Zhang, Yang Li, Ji-Gang Ren, Juan Yin, Qi Shen, Yuan Cao, Zheng-Ping Li, and et al. Satellite-to-ground quantum key distribution. *Nature*, 549(7670):43–47, Aug 2017.

[3] Keith R. Motes, Alexei Gilchrist, Jonathan P. Dowling, and Peter P. Rohde. Scalable boson sampling with time-bin encoding using a loop-based architecture. *Phys. Rev. Lett.*, 113:120501, Sep 2014.

[4] Shuntaro Takeda and Akira Furusawa. Universal quantum computing with measurement-induced continuous-variable gate sequence in a loop-based architecture. *Phys. Rev. Lett.*, 119:120504, Sep 2017.

[5] Warit Asavanant, Yu Shiozawa, Shota Yokoyama, Baramee Charoensombutamon, Hiroki Emura, Rafael N. Alexander, Shuntaro Takeda, Jun-ichi Yoshikawa, Nicolas C. Menicucci, Hidehiro Yonezawa, and Akira Furusawa. Generation of time-domain-multiplexed two-dimensional cluster state. *Science*, 366(6463):373–376, 2019.

[6] Yang Ji, Yunchul Chung, D. Sprinzak, M. Heiblum, D. Mahalu, and Hadas Shtrikman. An electronic mach-zehnder interferometer. *Nature*, 422(6930):415–418, 03 2003.

[7] Michihisa Yamamoto, Shintaro Takada, Christopher Bäuerle, Kenta Watanabe, Andreas D. Wieck, and Seigo Tarucha. Electrical control of a solid-state flying qubit. *Nature Nano.*, 7(4):247–251, 04 2012.

[8] S. Takada, C. Bäuerle, M. Yamamoto, K. Watanabe, S. Hermelin, T. Meunier, A. Alex, A. Weichselbaum, J. von Delft, A. Ludwig, A. D. Wieck, and S. Tarucha. Transmission phase in the kondo regime revealed in a two-path interferometer. *Phys. Rev. Lett.*, 113:126601, Sep 2014.

[9] Preden Roulleau, F. Portier, D. C. Glattli, P. Roche, A. Cavanna, G. Faini, U. Gennser, and D. Mailly. Finite bias visibility of the electronic mach-zehnder interferometer. *Phys. Rev. B*, 76:161309, Oct 2007.

[10] I. Neder, M. Heiblum, Y. Levinson, D. Mahalu, and V. Umansky. Unexpected behavior in a two-path electron interferometer. *Phys. Rev. Lett.*, 96:016804, Jan 2006.

[11] Izhar Neder, Florian Marquardt, Moty Heiblum, Diana Mahalu, and Vladimir Umansky. Controlled dephasing of electrons by non-gaussian shot noise. *Nature Physics*, 3(8):534–537, 2007.

[12] I. Neder, M. Heiblum, D. Mahalu, and V. Umansky. Entanglement, dephasing, and phase recovery via cross-correlation measurements of electrons. *Phys. Rev. Lett.*, 98:036803, Jan 2007.

[13] P. Samuelsson, E. V. Sukhorukov, and M. Büttiker. Two-particle aharonov-bohm effect and entanglement in the electronic hanbury brown–twiss setup. *Phys. Rev. Lett.*, 92:026805, Jan 2004.

[14] I. Neder, N. Ofek, Y. Chung, M. Heiblum, D. Mahalu, and V. Umansky. Interference between two indistinguishable electrons from independent sources. *Nature*, 448:333 EP –, 07 2007.

[15] G. Fève, A. Mahé, J. M. Berroir, T. Kontos, B. Plaçais, D. C. Glattli, A. Cavanna, B. Etienne, and Y. Jin. An on-demand coherent single-electron source. *Science*, 316(5828):1169, 05 2007.

[16] A. Marguerite, E. Bocquillon, J.-M. Berroir, B. Plaçais, A. Cavanna, Y. Jin, P. Degiovanni, and G. Fève. Two-particle interferometry in quantum hall edge channels. *physica status solidi (b)*, 254(3):1600618, 2017.

[17] J. Keeling, I. Klich, and L. S. Levitov. Minimal excitation states of electrons in one-dimensional wires. *Phys. Rev. Lett.*, 97:116403, Sep 2006.

[18] J. Dubois, T. Jullien, F. Portier, P. Roche, A. Cavanna, Y. Jin, W. Wegscheider, P. Roulleau, and D. C. Glattli. Minimal-excitation states for electron quantum optics using levitons. *Nature*, 502(7473):659–663, 10 2013.

[19] T. Jullien, P. Roulleau, B. Roche, A. Cavanna, Y. Jin, and D. C. Glattli. Quantum tomography of an electron. *Nature*, 514(7524):603–607, 10 2014.

[20] R. Bisognin, A. Marguerite, B. Roussel, M. Kumar, C. Cabart, C. Chapdelaine, A. Mohammad-Djafari, J. M. Berroir, E. Bocquillon, B. Plaçais, A. Cavanna, U. Gennser, Y. Jin, P. Degiovanni, and G. Fève. Quantum tomography of electrical currents. *Nature Communications*, 10(1):3379, 2019.

[21] A. A. Vyshnevyy, A. V. Lebedev, G. B. Lesovik, and G. Blatter. Two-particle entanglement in capacitively coupled mach-zehnder interferometers. *Phys. Rev. B*, 87:165302, Apr 2013.

[22] Patrick P. Hofer and Christian Flindt. Mach-zehnder interferometry with periodic voltage pulses. *Phys. Rev. B*, 90:235416, Dec 2014.

[23] Radu Ionicioiu, Paolo Zanardi, and Fausto Rossi. Testing bell's inequality with ballistic electrons in semiconductors. *Phys. Rev. A*, 63:050101, Apr 2001.

[24] M. Veldhorst, J. C. C. Hwang, C. H. Yang, A. W. Leenstra, B. de Ronde, J. P. Dehollain, J. T. Muhonen, F. E. Hudson, K. M. Itoh, A. Morello, and A. S. Dzurak. An addressable quantum dot qubit with fault-tolerant control-fidelity. *Nature Nanotechnology*, 9(12):981–985, 2014.

[25] Jun Yoneda, Kenta Takeda, Tomohiro Otsuka, Takashi Nakajima, Matthieu R. Delbecq, Giles Allison, Takumu Honda, Tetsuo Kodera, Shunri Oda, Yusuke Hoshi, Noritaka Usami, Kohei M. Itoh, and Seigo Tarucha. A quantum-dot spin qubit with coherence limited by charge noise and fidelity higher than 99.9%. *Nature Nanotechnology*, 2017.

[26] A. Noiri, T. Nakajima, J. Yoneda, M. R. Delbecq, P. Stano, T. Otsuka, K. Takeda, S. Amaha, G. Allison, K. Kawasaki, Y. Kojima, A. Ludwig, A. D. Wieck, D. Loss, and S. Tarucha. A fast quantum interface between different spin qubit encodings. *Nature Communications*, 9(1):5066, 2018.

[27] W. Huang, C. H. Yang, K. W. Chan, T. Tanttu, B. Hensen, R. C. C. Leon, M. A. Fogarty, J. C. C. Hwang, F. E. Hudson, K. M. Itoh, A. Morello, A. Laucht, and A. S. Dzurak. Fidelity benchmarks for two-qubit gates in silicon. *Nature*, 569(7757):532–536, 2019.

[28] Austin G. Fowler, Matteo Mariantoni, John M. Martinis, and Andrew N. Cleland. Surface codes: Towards practical large-scale quantum computation. *Phys. Rev. A*, 86:032324, Sep 2012.

[29] Luka Trifunovic, Oliver Dial, Mircea Trif, James R. Wootton, Rediet Abebe, Amir Yacoby, and Daniel Loss. Long-distance spin-spin coupling via floating gates. *Phys. Rev. X*, 2:011006, Jan 2012.

[30] Luka Trifunovic, Fabio L. Pedrocchi, and Daniel Loss. Long-distance entanglement of spin qubits via ferromagnet. *Phys. Rev. X*, 3:041023, Dec 2013.

[31] H. O. H. Churchill, A. J. Bestwick, J. W. Harlow, F. Kuemmeth, D. Marcos, C. H. Stwertka, S. K. Watson, and C. M. Marcus. Electron-nuclear interaction in 13c nanotube double quantum dots. *Nat Phys*, 5(5):321–326, 05 2009.

[32] T. Frey, P. J. Leek, M. Beck, A. Blais, T. Ihn, K. Ensslin, and A. Wallraff. Dipole coupling of a double quantum dot to a microwave resonator. *Phys. Rev. Lett.*, 108:046807, Jan 2012.

[33] K. D. Petersson, L. W. McFaul, M. D. Schroer, M. Jung, J. M. Taylor, A. A. Houck, and J. R. Petta. Circuit quantum electrodynamics with a spin qubit. *Nature*, 490(7420):380–383, 2012.

[34] M. R. Delbecq, L. E. Bruhat, J. J. Viennot, S. Datta, A. Cottet, and T. Kontos. Photon-mediated interaction between distant quantum dot circuits. *Nat Commun*, 4:1400, 01 2013.

[35] P. Scarlino, D. J. van Woerkom, U. C. Mendes, J. V. Koski, A. J. Landig, C. K. Andersen, S. Gasparinetti, C. Reichl, W. Wegscheider, K. Ensslin, T. Ihn, A. Blais, and A. Wallraff. Coherent microwave-photon-mediated coupling between a semiconductor and a superconducting qubit. *Nature Communications*, 10(1):3011, 2019.

[36] T. A. Baart, N. Jovanovic, C. Reichl, W. Wegscheider, and L. M. K. Vandersypen. Nanosecond-timescale spin transfer using individual electrons in a quadruple-quantum-dot device. *Applied Physics Letters*, 109(4):043101, 2016.

[37] H. Flentje, P. A. Mortemousque, R. Thalineau, A. Ludwig, A. D. Wieck, C. Bäuerle, and T. Meunier. Coherent long-distance displacement of individual electron spins. *Nature Communications*, 8(1):501, 2017.

[38] R. P. G. McNeil, M. Kataoka, C. J. B. Ford, C. H. W. Barnes, D. Anderson, G. A. C. Jones, I. Farrer, and D. A. Ritchie. On-demand single-electron transfer between distant quantum dots. *Nature*, 477(7365):439–442, 2011.

[39] Sylvain Hermelin, Shintaro Takada, Michihisa Yamamoto, Seigo Tarucha, Andreas D. Wieck, Laurent Saminadayar, Christopher Bäuerle, and Tristan Meunier. Electrons surfing on a sound wave as a platform for quantum optics with flying electrons. *Nature*, 477(7365):435–438, 09 2011.

[40] Shintaro Takada, Hermann Edlbauer, Hugo V. Lepage, Junliang Wang, Pierre-André Mortemousque, Giorgos Georgiou, Crispin H. W. Barnes, Christopher J. B. Ford, Mingyun Yuan, Paulo V. Santos, Xavier Waintal, Arne Ludwig, Andreas D. Wieck, Matias Urdampilleta, Tristan Meunier, and Christopher Bäuerle. Sound-driven single-electron transfer in a circuit of coupled quantum rails. *Nature Communications*, 10(1):4557, 2019.

[41] BertrandB., HermelinS., TakadaS., YamamotoM., TaruchaS., LudwigA., WieckA. D., BäuerleC., and MeunierT. Fast spin information transfer between distant quantum dots using individual electrons. *Nat Nano*, 11(8):672–676, 08 2016.

[42] H. Sanada, Y. Kunihashi, H. Gotoh, K. Onomitsu, M. Kohda, J. Nitta, P. V. Santos, and T. Sogawa. Manipulation of mobile spin coherence using magnetic-field-free electron spin resonance. *Nat Phys*, 9(5):280–283, 05 2013.

[43] Takafumi Fujita, Kazuhiro Morimoto, Haruki Kiyama, Giles Allison, Marcus Larsson, Arne Ludwig, Sascha R. Valentin, Andreas D. Wieck, Akira Oiwa, and Seigo Tarucha. Angular momentum transfer from photon polarization to an electron spin in a gate-defined quantum dot. *Nature Communications*, 10(1):2991, 2019.

[44] R. C. Miller, A. C. Gossard, D. A. Kleinman, and O. Munteanu. Parabolic quantum wells with the GaAs – $al_xga_{1-x}As$ system. *Phys. Rev. B*, 29:3740–3743, Mar 1984.

[45] Yin Wang, Ferdows Zahid, Yu Zhu, Lei Liu, Jian Wang, and Hong Guo. Band offset of gaas/alxga1 − xas heterojunctions from atomistic first principles. *Applied Physics Letters*, 102(13):132109, 2013.

[46] J. H. Davies. *The Physics of Low-dimensionla Semiconductors*. Cambridge University Press, 1998.

[47] R. Ludeke and G. Landgren. Electronic properties and chemistry of Ti/GaAs and Pd/GaAs interfaces. *Phys. Rev. B*, 33:5526–5535, Apr 1986.

[48] Raymond T. (董梓則) Tung. The physics and chemistry of the schottky barrier height. *Applied Physics Reviews*, 1(1):011304, 2014.

[49] M. Pioro-Ladrière, John H. Davies, A. R. Long, A. S. Sachrajda, Louis Gaudreau, P. Zawadzki, J. Lapointe, J. Gupta, Z. Wasilewski, and S. Studenikin. Origin of switching noise in GaAs/$Al_xGa_{1-x}As$ lateral gated devices. *Phys. Rev. B*, 72:115331, Sep 2005.

[50] B. van Wees, H. van Houten, C. Beenakker, J. Williamson, L. Kouwenhoven, D. van der Marel, and C. Foxon. Quantized conductance of point contacts in a two-dimensional electron gas. *Phys. Rev. Lett.*, 60:848–850, Feb 1988.

[51] J. C. H. Chen, Y. Sato, R. Kosaka, M. Hashisaka, K. Muraki, and T. Fujisawa. Enhanced electron-phonon coupling for a semiconductor charge qubit in a surface phonon cavity. *Scientific Reports*, 5:15176 EP –, 10 2015.

[52] Riccardo Manenti, Anton F. Kockum, Andrew Patterson, Tanja Behrle, Joseph Rahamim, Giovanna Tancredi, Franco Nori, and Peter J. Leek. Circuit quantum acoustodynamics with surface acoustic waves. *Nature Communications*, 8(1):975, 2017.

[53] K. J. Satzinger, Y. P. Zhong, H. S. Chang, G. A. Peairs, A. Bienfait, Ming-Han Chou, A. Y. Cleland, C. R. Conner, É. Dumur, J. Grebel, I. Gutierrez, B. H. November, R. G. Povey, S. J. Whiteley, D. D. Awschalom, D. I. Schuster, and A. N. Cleland. Quantum control of surface acoustic-wave phonons. *Nature*, 563(7733):661–665, 2018.

[54] J M Shilton, V I Talyanskii, M Pepper, D A Ritchie, J E F Frost, C J B Ford, C G Smith, and G A C Jones. High-frequency single-electron transport in a quasi-one-dimensional gaas channel induced by surface acoustic waves. *Journal of Physics: Condensed Matter*, 8(38):L531, 1996.

[55] William D. Hunt, Yoonkee Kim, and F. M. Fliegel. A synopsis of surface acoustic wave propagation on 100- cut ⟨110⟩- propagating gallium arsenide. *Journal of Applied Physics*, 69(4):1936–1941, 1991.

[56] R. Miskinis E. Urba. Physics and application of surface acoustic waves on various structures of gallium arsenide. *ULTRAGARSAS*, 45(4):13, 2002.

[57] Supriyo Datta. *Surface Acoustic Wave Devices*. Prentice-Hall, 1986.

[58] K. M. Lakin D.Penunuri. Leaky surface wave propagation on si, gaas, gap, al2o3 and quartz. *Ultrasonics Symposium Proceedings*, 1975.

[59] P.Hess Al.A.Kolomenskii A.A.Maznev, A.M.Lomonosov. Anisotropic effect in surface acoustic wave propagation from a point source in a crystal. 2003.

[60] Gento Yamahata, Katsuhiko Nishiguchi, and Akira Fujiwara. Gigahertz single-trap electron pumps in silicon. *Nature Communications*, 5:5038 EP –, 10 2014.

[61] Godfrey Gumbs, G. R. Aĭzin, and M. Pepper. Coulomb interaction of two electrons in the quantum dot formed by the surface acoustic wave in a narrow channel. *Phys. Rev. B*, 60:R13954–R13957, Nov 1999.

[62] Karsten Flensberg, Qian Niu, and Michael Pustilnik. Nonadiabaticity and single-electron transport driven by surface acoustic waves. *Phys. Rev. B*, 60:R16291–R16294, Dec 1999.

[63] A. Robinson and C. Barnes. Classical dynamics of electrons in quantized-acoustoelectric-current devices. *Phys. Rev. B*, 63:165418, Apr 2001.

[64] A. M. Robinson, V. I. Talyanskii, M. Pepper, J. E. Cunningham, E. H. Linfield, and D. A. Ritchie. Measurements of noise caused by switching of impurity states and of suppression of shot noise in surface-acoustic-wave-based single-electron pumps. *Phys. Rev. B*, 65:045313, Jan 2002.

[65] A. M. Robinson and V. I. Talyanskii. Shot noise in the current of a surface acoustic-wave-driven single-electron pump. *Phys. Rev. Lett.*, 95:247202, Dec 2005.

[66] W. Y. Mak, K. Das Gupta, H. E. Beere, I. Farrer, F. Sfigakis, and D. A. Ritchie. Distinguishing impurity concentrations in gaas and algaas using very shallow undoped heterostructures. *Applied Physics Letters*, 97(24):242107, 2010.

[67] J. C. H. Chen, D. Q. Wang, O. Klochan, A. P. Micolich, K. Das Gupta, F. Sfigakis, D. A. Ritchie, D. Reuter, A. D. Wieck, and A. R. Hamilton. Fabrication and characterization of ambipolar devices on an undoped algaas/gaas heterostructure. *Applied Physics Letters*, 100(5):052101, 2012.

[68] A. F. Croxall, B. Zheng, F. Sfigakis, K. Das Gupta, I. Farrer, C. A. Nicoll, H. E. Beere, and D. A. Ritchie. Demonstration and characterization of an ambipolar high mobility transistor in an undoped gaas/algaas quantum well. *Applied Physics Letters*, 102(8):082105, 2013.

[69] S.K-Hsiao A.Nasir A.Rubino J.P.Griffiths I Farrer D.A.Ritchie C.J.B.Ford Y.Chung, H.Hou. Quantised charge transort dirven by a surface acoustic wave in induced unipolar and bipolar junction. *arxiv*, 2019.

[70] R. J. Schneble, M. Kataoka, C. J. B. Ford, C. H. W. Barnes, D. Anderson, G. A. C. Jones, I. Farrer, D. A. Ritchie, and M. Pepper. Quantum-dot thermometry of electron heating by surface acoustic waves. *Applied Physics Letters*, 89(12):–, 2006.

[71] Pawel Utko, Poul Erik Lindelof, and Kurt Gloos. Heating in single-electron pumps driven by surface acoustic waves. *Applied Physics Letters*, 88(20):202113, 2018/10/28 2006.

[72] M. R. Astley, M. Kataoka, R. J. Schneble, C. J. B. Ford, C. H. W. Barnes, D. Anderson, G. A. C. Jones, H. E. Beere, D. A. Ritchie, and M. Pepper. Examination of surface acoustic wave reflections by observing acoustoelectric current generation under pulse modulation. *Applied Physics Letters*, 89(13), 2006.

[73] M. R. Astley, M. Kataoka, C. J. B. Ford, C. H. W. Barnes, D. Anderson, G. A. C. Jones, I. Farrer, H. E. Beere, D. A. Ritchie, and M. Pepper. Examination of multiply reflected surface acoustic waves by observing acoustoelectric current generation under pulse modulation. *Phys. Rev. B*, 74:193302, Nov 2006.

[74] J. Cunningham, V. I. Talyanskii, J. M. Shilton, M. Pepper, M. Y. Simmons, and D. A. Ritchie. Single-electron acoustic charge transport by two counterpropagating surface acoustic wave beams. *Phys. Rev. B*, 60:4850–4855, Aug 1999.

[75] N. E. Fletcher, J. Ebbecke, T. J. B. M. Janssen, F. J. Ahlers, M. Pepper, H. E. Beere, and D. A. Ritchie. Quantized acoustoelectric current transport through a static quantum dot using a surface acoustic wave. *Phys. Rev. B*, 68:245310, Dec 2003.

[76] F. J. Ahlers, O. F. O. Kieler, B. E. Sağol, K. Pierz, and U. Siegner. Quantized acoustoelectric single electron transport close to equilibrium. *Journal of Applied Physics*, 100(9):–, 2006.

[77] Jesús A. del Alamo and Cristopher C. Eugster. Quantum field- effect directional coupler. *Applied Physics Letters*, 56(1):78–80, 1990.

[78] A. Bertoni, P. Bordone, R. Brunetti, C. Jacoboni, and S. Reggiani. Quantum logic gates based on coherent electron transport in quantum wires. *Phys. Rev. Lett.*, 84:5912–5915, Jun 2000.

[79] Ryo Takasu, Yuya Sato, Tokuro Hata, Takafumi Akiho, Koji Muraki, and Toshimasa Fujisawa. Surface-acoustic-wave resonators with ti, cr, and au metallization on GaAs. *Applied Physics Express*, 12(5):055001, apr 2019.

[80] S. Rahman, M. Kataoka, C. H. W. Barnes, and H. P. Langtangen. Numerical investigation of a piezoelectric surface acoustic wave interaction with a one-dimensional channel. *Phys. Rev. B*, 74:035308, Jul 2006.

[81] Vyacheslavs Kashcheyevs and Bernd Kaestner. Universal decay cascade model for dynamic quantum dot initialization. *Phys. Rev. Lett.*, 104:186805, May 2010.

[82] V. I. Talyanskii, M. R. Graham, and H. E. Beere. Acoustoelectric y-branch switch. *Applied Physics Letters*, 88(8):–, 2006.

[83] S. R. Woodford, A. Bringer, and K. M. Indlekofer. Dephasing of a quantum dot due to the coulomb interaction with a gate electrode. *Phys. Rev. B*, 76:064306, Aug 2007.

[84] Matisse W. Y. Tu and Wei-Min Zhang. Non-markovian decoherence theory for a double-dot charge qubit. *Phys. Rev. B*, 78:235311, Dec 2008.

[85] M. Thorwart, J. Eckel, and E. R. Mucciolo. Non-markovian dynamics of double quantum dot charge qubits due to acoustic phonons. *Phys. Rev. B*, 72:235320, Dec 2005.

[86] M. R. Astley, M. Kataoka, C. J. B. Ford, C. H. W. Barnes, D. Anderson, G. A. C. Jones, I. Farrer, D. A. Ritchie, and M. Pepper. Energy-dependent tunneling from few-electron dynamic quantum dots. *Phys. Rev. Lett.*, 99:156802, Oct 2007.

[87] P.O.Froman H.Froman. *JWKB Approximation: Contributions to the Theory*. North-Holland,Amsterdam, 1965.

[88] Richard G. Forbes. On the need for a tunneling pre-factor in fowler–nordheim tunneling theory. *Journal of Applied Physics*, 103(11):114911, 2008.

[89] William H. Miller. Semiclassical treatment of multiple turning- point problems—phase shifts and eigenvalues. *The Journal of Chemical Physics*, 48(4):1651–1658, 1968.

[90] M. Kataoka, M. R. Astley, A. L. Thorn, D. K. L. Oi, C. H. W. Barnes, C. J. B. Ford, D. Anderson, G. A. C. Jones, I. Farrer, D. A. Ritchie, and M. Pepper. Coherent time evolution of a single-electron wave function. *Phys. Rev. Lett.*, 102:156801, Apr 2009.

[91] C. H. W. Barnes, J. M. Shilton, and A. M. Robinson. Quantum computation using electrons trapped by surface acoustic waves. *Phys. Rev. B*, 62:8410–8419, Sep 2000.

[92] X. Shi, M. Zhang, and L. F. Wei. Quantum computation with moving quantum dots generated by surface acoustic waves. *Phys. Rev. A*, 84:062310, Dec 2011.

[93] Scott Hill and William K. Wootters. Entanglement of a pair of quantum bits. *Phys. Rev. Lett.*, 78:5022–5025, Jun 1997.

[94] Asher Peres. Separability criterion for density matrices. *Phys. Rev. Lett.*, 77:1413–1415, Aug 1996.

[95] John F. Clauser, Michael A. Horne, Abner Shimony, and Richard A. Holt. Proposed experiment to test local hidden-variable theories. *Phys. Rev. Lett.*, 23:880–884, Oct 1969.

[96] R. Hanson, L. P. Kouwenhoven, J. R. Petta, S. Tarucha, and L. M. K. Vandersypen. Spins in few-electron quantum dots. *Rev. Mod. Phys.*, 79:1217–1265, Oct 2007.

[97] Toshimasa Fujisawa, David Guy Austing, Yasuhiro Tokura, Yoshiro Hirayama, and Seigo Tarucha. Allowed and forbidden transitions in artificial hydrogen and helium atoms. *Nature*, 419:278 EP –, 09 2002.

[98] Massoud Borhani, Vitaly N. Golovach, and Daniel Loss. Spin decay in a quantum dot coupled to a quantum point contact. *Phys. Rev. B*, 73:155311, Apr 2006.

[99] Vitaly N. Golovach, Massoud Borhani, and Daniel Loss. Electric-dipole-induced spin resonance in quantum dots. *Phys. Rev. B*, 74:165319, Oct 2006.

[100] K. C. Nowack, F. H. L. Koppens, Yu. V. Nazarov, and L. M. K. Vandersypen. Coherent control of a single electron spin with electric fields. *Science*, 318(5855):1430–1433, 2007.

[101] M. Pioro-Ladrière, T. Obata, Y. Tokura, Y. S. Shin, T. Kubo, K. Yoshida, T. Taniyama, and S. Tarucha. Electrically driven single-electron spin resonance in a slanting zeeman field. *Nature Physics*, 4:776 EP –, 08 2008.

[102] J. Yoneda, T. Otsuka, T. Nakajima, T. Takakura, T. Obata, M. Pioro-Ladrière, H. Lu, C. J. Palmstrøm, A. C. Gossard, and S. Tarucha. Fast electrical control of single electron spins in quantum dots with vanishing influence from nuclear spins. *Phys. Rev. Lett.*, 113:267601, Dec 2014.

[103] A. Noiri, J. Yoneda, T. Nakajima, T. Otsuka, M. R. Delbecq, K. Takeda, S. Amaha, G. Allison, A. Ludwig, A. D. Wieck, and S. Tarucha. Coherent electron-spin-resonance manipulation of three individual spins in a triple quantum dot. *Applied Physics Letters*, 108(15):153101, 2016.

[104] Takumi Ito, Tomohiro Otsuka, Takashi Nakajima, Matthieu R. Delbecq, Shinichi Amaha, Jun Yoneda, Kenta Takeda, Akito Noiri, Giles Allison, Arne Ludwig, Andreas D. Wieck, and Seigo Tarucha. Four single-spin rabi oscillations in a quadruple quantum dot. *Applied Physics Letters*, 113(9):093102, 2018.

[105] Paulo V. Santos, Junsaku Nitta, and Klaus H. Ploog. Stern–gerlach spin filter using surface acoustic waves. *Solid State Communications*, 132(9):631 – 634, 2004.

[106] Niels Ubbelohde, Frank Hohls, Vyacheslavs Kashcheyevs, Timo Wagner, Lukas Fricke, Bernd Kästner, Klaus Pierz, Hans W. Schumacher, and Rolf J. Haug. Partitioning of on-demand electron pairs. *Nat Nano*, 10(1):46–49, 01 2015.

[107] A.Altland and B.Simons. *Condensed Matter Field Theory*. Cambridge University Press, second edition edition, 2010.